MICROFLUIDIC SCHEMES TO STUDY FREE STANDING LIPID BILAYER INTERACTIONS AND PROTEIN BILAYERS

Dissertation

zur Erlangung des Grades
des Doktors der Naturwissenschaften
der Naturwissenschaftlich-Technischen Fakultät II
- Physik und Mechatronik -
der Universität des Saarlandes

von

José Nabor Vargas del Castillo

Saarbrücken

2015

Tag des Kolloquiums: 01.06.2016

Dekan: Univ.-Prof. Dr. rer. nat. Georg Frey

 Mitglieder des Prüfungsausschusses:

Vorsitzender: Univ.-Prof. Dr. rer. nat. Heiko Rieger

Gutachter: Univ.-Prof. Dr. rer. nat. Ralf Seemann

Univ.-Prof. Dr. rer. nat. Ludger Santen

Akademischer Mitarbeiter: Dr. Varun Giri

ABSTRACT

In the present thesis, a microfluidic scheme with simultaneous optical and patch clamping access is developed to study membrane fusion, its intermediated states and hydrophobin protein bilayers. As a first application, the formation of a free standing hemifused state due to the interaction of free standing lipid bilayers is studied. The hemifusion state is shown to be the result of a dewetting process under no-slip boundary conditions. Furthermore, the microfluidic scheme is extended to study membrane fusion by means of SNARE proteins; small unilamellar vesicles containing v-SNARE proteins are allow to contact a free standing lipid bilayer containing t-SNARE proteins, bilayer-vesicle fusion occurs via t-SNARE/v-SNARE complex formation. Single fusion events were characterized using fluorescence and capacitance measurements. As a third application, the microfluidic scheme is used for the production of free standing hydrophobin protein bilayers. Adhesion properties of the protein bilayers were characterized as a function of both the protein orientation and its charged amino acids distribution. For that, three mutation variants and the wild type protein were used. The obtained results revealed that a reduction of the absolute number of charges on the protein surface leads to an increase of the adhesion energy between protein leaflets.

KURZZUSSAMENFASSUNG

In der vorliegenden Arbeit wurde ein mikrofluidisches Verfahren zur gleichzeitig optisch und elektrophysiologisch Untersuchung der membranen Fusion und deren Wechselwirkungen entwickelt. Zuerst, wird die formation einer Hemifusion studiert, die sich bildet wenn zwei frei stehende Lipid Doppellagen kontaktiert werden; dies geschieht durch einen Entnetzungsprozess mit Haftrandbedingung. Zweitens, einfache SNARE vermittelnde Fusions Ereigniße werden erzeugt. Über Ca^{2+} vermittelte Fusion von t-SNARE dotierten Vesikeln mit einer Lipiddoppellage werden zuerst t-SNARE's in die Doppellage eingefügt. Danach werden v-SNARE dotierte Vesikel eingespült und in Kontakt mit der Doppellage gebracht. Die nachfolgende Fusion wird durch die Bildung von t-SNARE/v-SNARE–Komplexen vermittelt. Aufgrund der Fusion beider, der t-SNARE/v-SNARE Interaktion mit Calcium Ionen war diese charaktarisiert durch die Nutzung von Fluoreszenz- und Kapazitäts messungen. Es zeigt sich, dass die SNARE vermittelte Fusion schneller ist als die Ca^{2+}. Drittens, wird das mikrofluidische Verfahren außerdem noch verwendet um freistehende Hydrophobinen-Doppellagen herzustellen. Die Ahesionseigenschaften der Protein Doppellagen wurden charakterisiert als eine Funktion beider, der protein orientierung und seiner Aminosäuren Wechselwirkungsenergie . Dafür wurden drei Mutations Varianten sowie der ursprüngliche Typ des proteins verwendet. Die erhaltenen Resultate lassen darauf schließen das eine reduktion der Anzahl der Wechselwirkungsenergien an der Protein Oberfläsche zu einer Erhöhung der Adhesionserergie zwischen den Protein Lagen führt.

Contents

List of Figures

List of Tables

Introduction

In the prebiotic environment, simple molecules known as fatty acids are believed to self-assemble to create a protocell membrane [1]. This prebiotic membrane was responsible for isolating the protocell from its hostile environment [2], allowing it to evolve and develop a unique biochemistry making life in all its diversity to become possible [3]. The continuous evolution of the protocell's inner biochemistry (gens) resulted in a variety of sophisticated biological membranes like archaea, bacteria, and eukaryotic cell membranes [4, 5]. The eukaryotic cell is highly compartmentalized; it means that its inner-side is made of a vast net of different membranes [6]. Both eukaryotic cell inner and external (cell to cell) communication, impose the requirement of overcoming the membrane barrier to deliver a messenger molecule. To allow the crossing of big molecules through the membrane, the cell wraps messenger molecules in spherical lipid bilayers known as vesicles [7]. These vesicles in turn, interact with the target internal or external membrane in a process called membrane fusion [8]. Membrane fusion is carried out by a series of complex machineries better known as fusogenic proteins [9]. Perhaps the most studied fusogenic proteins are the SNARE family, which were discovered in the 80's by Prof. J. Rothman and co-workers [10]. Since then, SNAREs have been found responsible of triggering fusion for vesicle trafficking inside the cell, and the exocytose of synaptic vesicles in the neuronal system [10]. The mechanisms by which SNAREs fuse two opposing membranes are yet not well understood, but intense researches in this field have elucidated a series of fusion steps prior to reach full membrane fusion [11]. In vitro experiments constitute an important experimental tool to study membrane fusion. Those experiments normally use supported membranes or vesicles; both techniques have several shortcoming in terms of bio-relevance or accessibility for inspecting the interacting membranes.

In the present thesis , a microfluidic platform is developed and used to produce and to study the different stages of membrane fusion between two free standing lipid bilayers. The microfluidic platform is based on the concept of droplet interface bilayer which was proposed by H. Bayley et al [12]. This platform allows for the production of stable free standing lipid bilayers and to bring them into contact in a controlled fashion. It also allows the inspection of the membrane interaction process by optical microscopy and electrophysiological measurements (patch-clamp) simultaneously. Furthermore, the microfluidic platform was extended to the study of membrane fusion by means of SNARE proteins. A free standing lipid bilayer containing t-SNARE proteins is produced in a microfluidic channel (T-bilayer). Small unilamellar vesicles containing v- SNARE proteins are brought in contact with the T-bilayer. As a result of the t-SNARE/v-SNARE interaction the vesicles fused to the T-bilayer. The vesicle fusion process is monitored by fluorescence microscopy and patch clamping.

Another phenomena addressed in the present thesis, is the production of hydrophobin protein bilayers. The aim of the study is to characterize the protein-protein interaction in a free standing bilayer. Hydrophobins are a family of small relatively hydrophobic fungal proteins (ca. 100 amino acids) [13]. They are divided into two classes according to the hydropathy patterns and the solubility of the protein assemblages [14]. Class I hydrophobins are mostly soluble in oil [15], while class II hydrophobins are soluble in polar solvents [16]. The most remarkable aspect of these proteins is their ability to convert hydrophobic surfaces to hydrophilic and vice versa, by self-assembly into an amphipathic protein layer [17]. Due to their high surface active properties, hydrophobins have a wide range of applications: In the food industry, these proteins are used to stabilize emulsions, e.g. beers [18], ice-cream [19]. In biosensor, hydrophobins are used to immobilize proteins or cell to different surfaces [20]. In tissue engineering, they increase implants biocompatibility due to their surface properties [21]. And in drug delivery system hydrophobins are used to stabilize oil droplets [22]. HFBI protein, a class II hydrophobin was selected as the test protein for the present work. The

main characteristic of HFBI proteins is the present of charged amino acids on its surface [23]. Lienemman et, al. have produced a mutant variant of HFBI proteins, by replacing the charged amino acids on the wild type HFBI protein [24]. Both, the wild type HFBI and the mutant variants were used to inspect the influence of the charge distribution on HFBI protein bilayer tension and adhesion energy.

1.   Background and State of the Art

In this chapter we focus on the basic understanding of membrane cell biology and the physical principles of biomembranes, self-assembly, and membrane interaction leading to a fusion or merging of lipid membranes. Relevant principles of microfluidics are also explained being the primary tool for free standing bilayers production. A description of patch clamping is given as the method to measure bilayer properties.

1.1   Biological membranes and functions

Lipid cell membranes represent the outer boundary of all living cells [25, 26]. A cell membrane is a thin, flexible and fragile structure which acts as a barrier to isolate the internal cell world from its external environment, ensuring its physical integrity [27]. All cell membranes must be able to maintain vast differences in chemical gradients between the cell and its surroundings. However, they also must regulate the passage of nutrients and ions into the cell and the passage of waste products out of it [25, 28]. Furthermore, lipid membranes are responsible for the high degree of cell's compartmentalization which separate the cell interior in many different organelles; as the endoplasmic reticulum, mitochondria, nuclei, and the golgi apparat (figure 1). Each of these organelles has its own biochemical environment, totally independent of one another including the cytoplasm. Compartmentalization allows cells to perform many different complex reactions in its cytoplasm [29, 30]. The organelles cooperated and communicate with one another via the so called trafficking vesicles. Vesicles are spherical lipid bilayers that fuse to a given organelle to maintain the integrity and functionality of cells [31, 32]. Cell membranes are also an important factor in cell to cell communication or the flow of information from one cell to another [29, 33]. Attached to the cell membrane there are many sensor like proteins that promote

cell signaling and communication with neighbor cells [34, 35]. In spite of the vast variety of biological cell membranes in nature, they all conserve the same building blocks [25], basically they are organized in a "fluid bilayer" compose mainly of both lipid and protein molecules[25, 29].
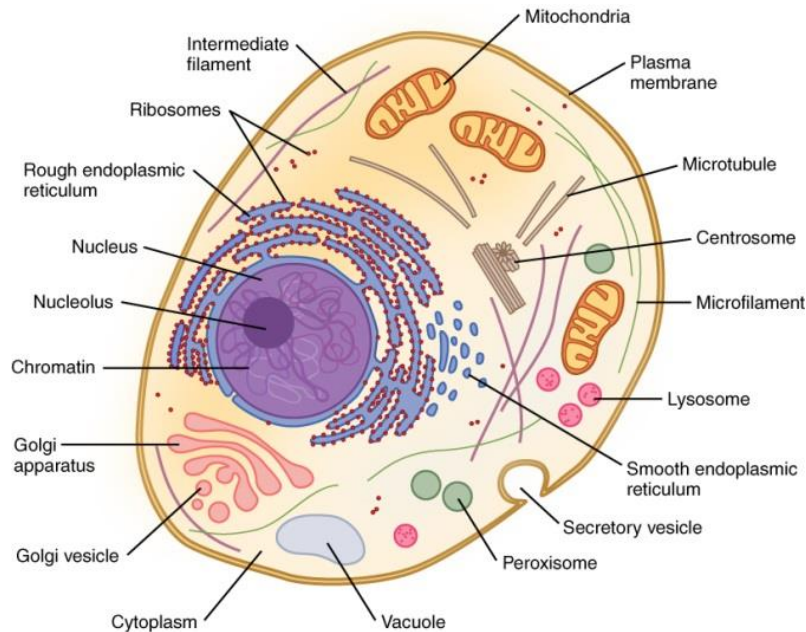
Figure 1 A eukaryotic cell is surrounded by a plasmatic membrane composed mainly of lipid and proteins, cell possess a high degree of inner compartmentalization, at the cytoplasm there are many organelles which are isolated by lipid membranes. Communication between the different organelles proceeds via trafficking vesicles.

1.1.2   Architecture of Biological membranes

The plasma cell membrane of all animal cells can be viewed as a multilayer system [29]. The outermost layer is composed of the glycocalyx a film formed of the glycolipid head groups and the branched polypeptide of the glycoprotein's head groups (figure 2) [36, 37]. The innermost layer at the intracellular side is composed mostly of cytoskeleton micro-filaments [38, 39]. The center layer, is formed by the liquid crystalline lipid-protein structure held together by non-covalent bonds [40, 41]. The molecular composition of the central lipid-protein bilayer varies substantially from one cell type to another [29]. However, cells

maintain the same few classes of lipids from the enormous variety of natural occurring lipids [25]. Mainly, the phospholipids; phosphatidylcholine (PC), phosphatidylserine (PS), phosphatidylethanolamine (PE), sphingomyelin (SPHM). Others lipid like molecules are cholesterol and cerebrosides [42, 43]. The lipid composition of an erythrocyte plasma membrane and some intracellular organelles are summarized (table 1).
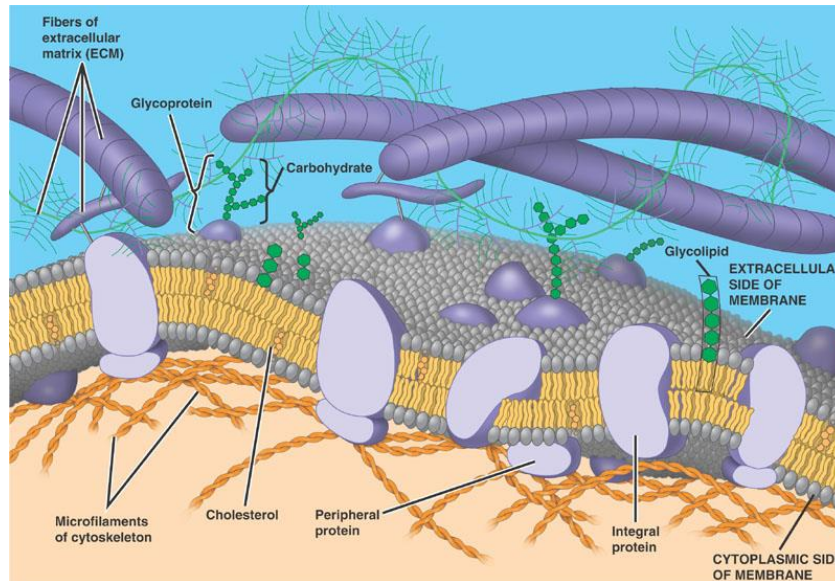
Figure 2 Schematic of the different layers forming a plasma cell membrane, the outermost is known as glycocalix layer, the innermost layer at the cytoplasmic side is made of a network of microfilaments, and the center layer is formed by the liquid crystalline lipid-protein structure.

Lipid	Erythrocyte	Golgi	Lysosome	Nuclei	Neuron
PC	20%	25%	23%	44%	48%
PE	18%	13%	13%	17%	21%
PS	7%	3%		4%	5%
PI	3%	5%	6%	6%	7%
SPHM	18%	7%	23%	3%	4%
Others	11%	43%	16%	15%	1%
Cholesterol	20%	8%	14%	10%	11%

Table 1 Lipid composition of different cell membranes [25]

1.1.2.1 Membrane Proteins

Depending on the cell type or organelle, bio-membranes contain hundreds of different proteins [29]. Each membrane protein has a defined orientation relative to the cytoplasm. Therefore the properties of one leaflet of a membrane are different from those of the other leaflet [44]. Proteins carry out most of the cell specific functions as water and ion transport, signaling, and fusion [45, 46]. Depending on the interaction type to the cell membrane, proteins can be divided in three main groups. *Peripheral proteins,* these are located entirely on the surface of the lipid bilayer on the cytoplasmic or extracellular side [47]. *Lipid-anchored proteins,* are located outside the lipid bilayer covalently linked to a lipid molecule within the bilayer [48]. And *transmembrane proteins,* which penetrate entirely the lipid bilayer having domains that protrude from both the extracellular and cytoplasmic sides of the membrane [49]. SNAREs and Ion channels are typical examples of transmembrane proteins [50].

1.1.2.2 Lipids

Lipid molecules mainly phospholipids, compose the core of the cell membrane bilayers [29]. They act primarily as the structural backbone of the membrane and provide the barrier that prevents random movements of water-soluble materials across the cell membrane [25]. Phospholipids themselves have backbones which serve as an attachment site for different functional groups [51]. They do not form covalent bonds with other lipids. As a result every phospholipid can be seen as a separate molecule within a membrane [52]. As it is shown in table 2, bio-membranes contain a wide diversity of lipids all of which are amphipathic in nature. This means, lipids contain both a hydrophilic and hydrophobic part (figure 3) [29]. Lipids have the general formula; $R_1COOCH_2 \cdot CH(OOCR_2) \cdot CH_2OP(O_2)OX$, R_1 and R_2 represent the hydrocarbon chains and X is the alcohol part of the phosphate ester head group [26].
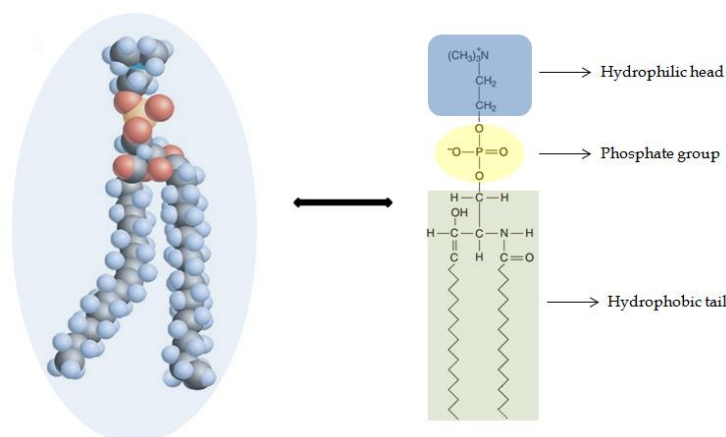
Figure 3 Molecular structure of a phospholipid molecule, it is and amphiphilic molecule divided into two main regions; a hydrophobic part which compose mostly of fatty acids, and a hydrophilic part that can be a phospho-choline, phospho-serine, etc.

Differences in the polar head group and the acyl chains accounts for over 100 different lipid types in a normal cell membrane [26]. Such lipids diversity confers the cell membrane with a variety of optimized physical properties depending on cellular needs [53]. For instance, microorganisms can adjust their lipid membrane composition in respond to environmental temperature changes to preserve membrane fluidity [54]. Another example comes from cells involved in exocytosis, they have a markedly distinct leaflet composition, the inner leaflet facing the exocytic vesicles is compose of a large amount of lipid having strong tendency to form non-lamellar structures in present of divalent cations [55, 56].

1.1.3   Lipids polymorphism and Self-assembly of Lipid Bilayer

Due to their amphiphilic characteristic, lipid molecules self-aggregate in water solutions [26]. The driving mechanism that make possible such a self-assembly is known as the hydrophobic effect [57, 58]. As a result of the hydrophobic effect, the hydrocarbon tails of the lipids induce the molecules to congregate together, while the hydrophilic head groups remain in contact with the water solution. Therefore lipids are assembled into well-defined structures such as micelles and bilayers [59, 60]. A basic method to understand the self-assembly behavior of amphiphilic molecules is taking into account the lipid or surfactant

molecular shape [26, 61]. Thus self-assembly of amphiphilic molecules is dictated by a dimensionless packing parameter:

$$S = \frac{V}{al} \tag{1}$$

where V is the hydrocarbon volume, a is the area of the head group, and l is the length of the hydrocarbon chain [26]. When the packing parameter $S \approx 1$, lipid molecules have a cylindrical shape, e.g. PC lipids (figure 4a), they form lamellar phases (figure 1.3d). For $S > 1$, lipid molecules have a conical shape due to its small polar head, e.g. PE lipids, normally self-assemble in a hexagonal (H_{II}) phase (figure 4c,f). For $S < 1/3$, the lipid molecules possess only one hydrocarbon chain, e.g. monoolein, that confers an inverse conical shape, this molecules self-assemble in micelles or H_I phase (see figure 4b,e) [61].
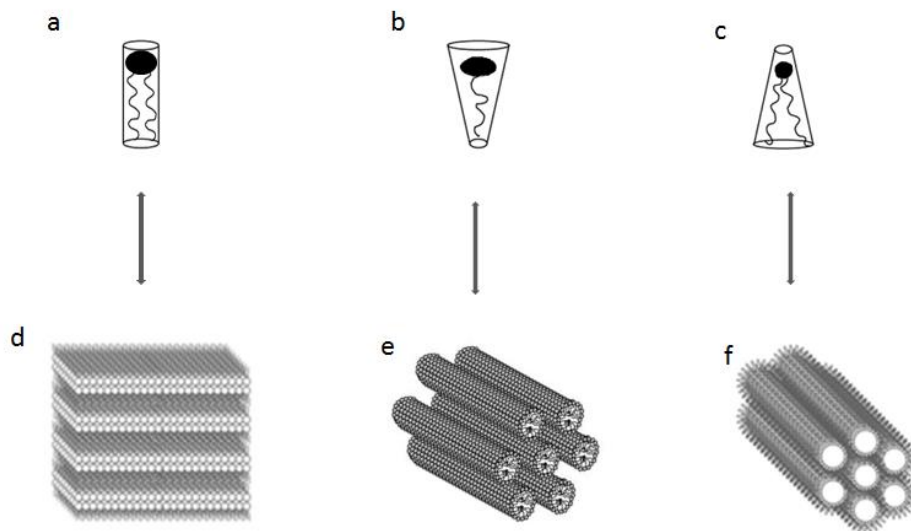
Figure 4 Lipid molecule shape and lipid phase structure in water systems, a) cylindrical shape characteristics of PC lipids. b) inverse conical shape for lipid with one hydrocarbon chain as monoolein. c) conical shape for PE lipids. d) Lamellar phase of lipid-water systems. e) hexagonal (HI) phase. d) hexagonal (HII) phase.

Another way to describe lipid self-assembly, is taking into account the critical micelle concentration factor (CMC) in mole fraction units [26]. For a given CMC

value, lipid monomers self-assemble into a corresponding micelle or bilayer state. Above the CMC, monomers and micelles exist in dynamic equilibrium [26]. Below this concentration amphiphilic molecules behave as dissolved solutes with no detectable association between molecules [61]. The CMC factor can be determined by the following relation:

$$\ln[\text{CMC}] = \frac{\Delta G}{RT} \tag{2}$$

where ΔG is the free energy of transfer of a lipid monomer into a corresponding micelle or bilayer state [59]. The CMC can be affected by many variables like temperature and pressure being of relatively minor importance. It decreases with increasing hydrocarbon chain length of the surfactant or lipid molecule. For ionic surfactants it also depends on the nature and concentration of cations in solution [26, 59]. Added electrolytes decrease the CMC, thus effect increases with decreasing charge density of the cations.

1.1.4 Electrical Properties of Lipid Bilayers

To introduce the most relevant electrical properties of free standing lipid bilayers, let us analyze the scenario depicted in figure 5, a flat lipid bilayer separating two high ionic strength water compartments. The aliphatic central core of the bilayer represents a barrier for the charged molecules to cross the membrane from one compartment to the other [61]. This hydrophobic core can be seen as an insulator of certain thickness d, which corresponds to the length of the lipid hydrocarbon tails [26]. The later implies that a bilayer behaves as an electrical capacitor, where a dielectric material separates two conducting plates. Therefore the voltage drop U, across the lipid bilayer is proportional to the charge Q, as follows:

$$Q = CU \tag{3}$$

where C is the total capacitance. This total capacitance is related to the dielectric constant ε of the hydrocarbon core of the lipid membrane by:

$$C = \frac{\varepsilon_0 \varepsilon A}{d} \tag{4}$$

Where ε_0 is the vacuum permittivity, ε is the lipid dielectric constant, A is the lipid bilayer area, and d is the hydrophobic core thickness [61]. The lipid bilayer and its hydrophobic core are expected to have defects, causing a week leakage ions current I_m flowing through it. This means that a lipid bilayer also possess an intrinsic resistance R_m associated to it.
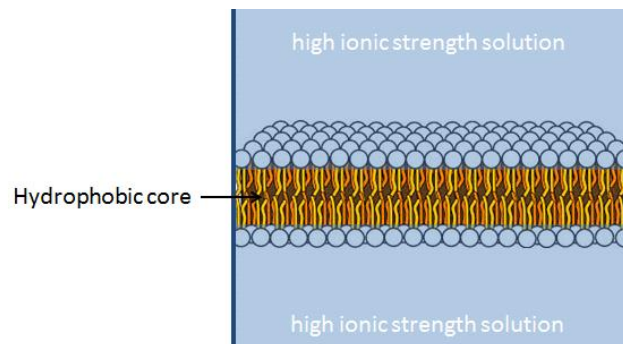
Figure 5 A flat lipid bilayer separating two high ionic strength water compartments, the hydrophobic core of the lipid bilayer prevent the flow of ions from one compartment to the other, therefore a lipid membrane can be modeled as an electrical capacitor.

1.1.4.1 Electroporation of Lipid Bilayers

Reversible pores in lipid bilayers can be induced by applying an external electric field. This technique is referred as electro-permeabilization or electroporation [62, 63]. Each pore is formed by a large number of lipid molecules, but the shape, size and stability of the pore are strongly influenced by the structure of these molecules and their local interactions [62]. According to the

most applied model for electroporation, formation of a pore of radius (r) changes the free energy of the membrane by [64, 65]:

$$\Delta W(r, U) = 2\gamma\pi r - \Gamma\pi r^2 - \frac{(\varepsilon_e - \varepsilon_m)\pi r^2}{2d}U^2 \tag{5}$$

where γ is the surface tension, Γ the interfacial tension of the lipid bilayer, U is the transmembrane voltage, while ε_e and ε_m are the dielectric permittivities of the aqueous medium (in approximation, that of water) in the pore and the bilayer [62]. The transmembrane voltage reduces both the critical radius of the pore and the energy barrier, which are given by:

$$r_c(U) = \frac{\gamma}{\Gamma + \frac{\varepsilon_e - \varepsilon_m}{2d}U^2}, \qquad \Delta W_c(U) = \Delta W(r_c, U) = \frac{\pi\gamma^2}{\Gamma + \frac{\varepsilon_e - \varepsilon_m}{2d}U^2} \tag{6}$$

1.1.5 Interfacial Tension of Bilayers

When two water droplets decorate with lipid monolayers come to close contact, they for a lipid bilayer (figure 6). The interfacial tension Γ of such a lipid bilayer can be determined by measuring the angle θ of the bilayer at the water/oil or water/air interface (figure 6), producing the following expression [61]:
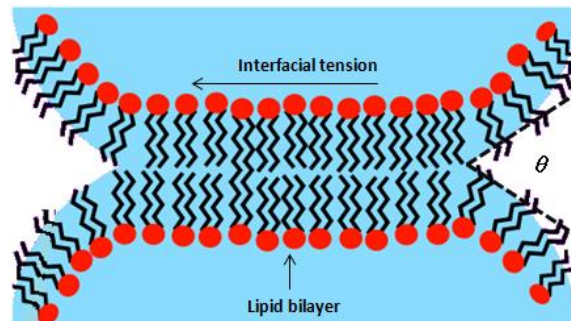
Figure 6 Lipid bilayer produced by contacting two water droplets decorate with a lipid monolayer. The bilayer forms an angle at the water/oil or water/air interface, this angle is used to determine the interfacial or bilayer tension.

$$\Gamma = 2\gamma \cos{}^{\theta}\!/_{2} \tag{7}$$

where γ is the surface tension of the water/oil or water/air interface. The free energy change ΔF of the transition from two separate monolayers to one bilayer can be described as follows:

$$\Delta F = \Gamma - 2\gamma = 2\Delta\gamma \tag{8}$$

$$\Delta F = 2\gamma \left(\left(\cos{}^{\theta}\!/_{2} \right) - 1 \right) \tag{9}$$

1.1.5 Mechanisms of Membrane Fusion phenomena

As it was discussed in the introductory section of the present work, membrane fusion is an essential tool to ensure cell viability and communication [66]. However, cell membrane fusion is not a yet well understood process, in which there is a fine tuned interplay of many different membrane proteins [67], lipid and ions [68], responsible for the approximation and interaction of two separate lipid membranes [66]. Basically, it can be seen as the process by which two independent lipid membranes merge together to form a single one [69]. In the following we will discuss the condition for membrane fusion to occur in pure lipidic bilayer systems. Experimental evidences have demonstrated that two independent bilayers can be brought into contact for a long period of time, without resulting in a fusion even [70]. The later implies that for membrane fusion to occur, certain conditions have to be reached. For instance, the lipid composition of a given bilayer has a crucial role in the tendency of a lipid membrane to form fusion intermediates or pores over contact with another bilayer [69]. Physically speaking the tendency of a pure lipid bilayer to trigger fusion could be attributed to the effective spontaneous curvature or the ability of lipid molecules to adopt a particular orientation, with respect to a flat imaginary plane lying inside the monolayer close to the interface between the polar heads and the hydrocarbon

chains of the lipids [61]. In absence of any forces acting on its surface, a lipid monolayer adopts a curvature *H*, the spontaneous curvature of a lipid bilayer is related to the *H* of both the inner and outer monolayer as follow, $H^B = H^{out} - H^{in}$ [71, 72]. Under external forces, a membrane bends with respect to its spontaneous curvature. The bending energy *F* as a function of the deformation is given by:

$$F = (1 / 2)A \cdot k \cdot (H' - H)^2 \tag{10}$$

 where *A* is the membrane area and *k* is the bending modulus. From equation 10, we could infer that lipids with intrinsic curvature (section 1.3) will increase the bending energy according to a square power relation. Experimental evidence has shown that lipids with intrinsic negative curvature promote membrane fusion [71], while lipids having intrinsic positive curvature prevent fusion to occur [72]. Taking into account the lipid shape and its orientation in bilayers, we will now introduce the most fundamental theory of the lipid membrane fusion pathway. Which was originated with the discovery of point like defects observed on liposome membrane surfaces in freeze fracture electron microscopy experiments. These defects were supposed to be lipid molecules adopting and hexagonal phase [72]. The assumption of lipids adopting hexagonal phase into the membrane, opens the door for the development of the inverted micellar intermediate mechanism, better known as a stalk model or the continuum approach [73]. This model treats lipid membranes as macroscopic continuous films that can be described by the elastic theory of lipid monolayers, and the self-consistent mean field theory of the lipid bilayer interior [74]. The core of the stalk model is the Assumption that *"the state of fused membranes is energetically more favorable than the initial state of two separate membranes, and thus that membranes have a tendency to fuse"* [73]. To summarize the fusion pathway figure 7, depicts the process of two independent lipid bilayers in close proximity. When lipid bilayers come into contact, they interact to form a structure called a fusion stalk, a hourglass shaped structure connecting the two proximal lipid monolayers (leaflets) while the distal

monolayers remains separate (figure 7a-c) [75, 76]. The fusion stalk is believed to expand spontaneously to a more energetically favorable state, which is known as hemifusion and its main characteristic is the interaction of the two distal monolayers which form a new single lipid bilayer (figure 7d) [77]. A hemifusion diaphragm is supposed to be a transient structure that either dissociates, leaving two separated membranes, or gives rise to a fusion pore (figure 7e) [71]. The generation of a fusion pore is the final step in the fusion pathway, at this point there is a liquid content mixing in the case of two liposomes and the starting two independent bilayers became one [78].
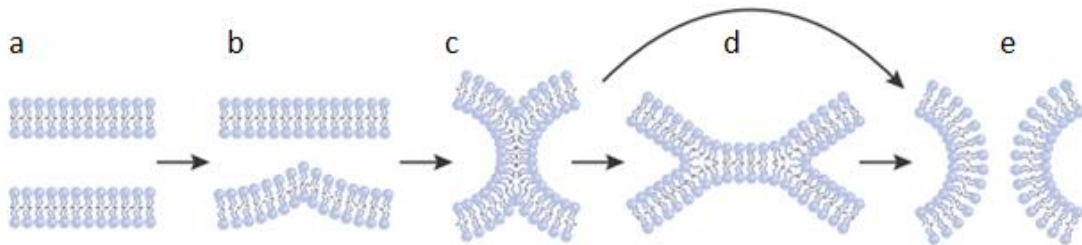
Figure 7 Interaction of two lipid bilayers, a) two independent lipid bilayers. b) lipid bilayers in close proximity. c) upon interaction they create a so called stalk. d) the stalk structure is thought to expand into a hemifusion diaphragm. e) the fusion pores will open within the hemifused membrane. Image taken from [71].

The stalk model has led to two competing scenarios for the evolution of membrane fusion and its intermediate structures [76]. Some scientists believe that the fusion stalk structure expands radially into a hemifusion diaphragm, which is thought to be an energetically more favorable state [75], and the subsequence fusion pore will form along the hemifusion diaphragm perimeter. Alternatively, it has been proposed that the stalk decays directly into the fusion pore, so that the stage of hemifusion is not a mandatory intermediate step in lipid membrane fusion pathway [79]. Experimental evidences in pure lipid membrane systems account for the generation of hemifusion diaphragm in liposome and supported bilayers fusion experiments [71]. While the only evidence for the decay of a fusion stalk

into a pore, comes from computational simulations [79]. Both theoretical and experimental findings have center their attention in reproducing a hemifusion state considering mostly the lipid molecule types or the favorable energetic pathway for the decay into a fusion pore. However little is known about the physical driving mechanism leading to such a state.

1.1.6 Machinery for Membrane Fusion

Until now, we have discussed the implication of lipid molecule type and shape in the fusion process of pure lipid membrane experiment such as liposome or black lipid membranes. In the following, we will cover the different machineries and molecules acting as fusogenic agents in bilayer systems.

Small molecules like cations have been reported from the early seventies to have fusogenic properties, e.g. Ca^{2+}, Mg^{2+}, Mn^{2+}, Zn^{2+}, La^{3+}, Sr^{3+}, and H^+ [68]. Liposome to liposome fusion essays, have revealed that Ca^{2+} and Mg^{2+} present high fusogenic characteristic in PC:PS membrane systems. These divalent cations bind to the negatively charged polar group of the PS molecules reducing the electrostatic repulsion, therefore favoring vesicle aggregation [80]. Furthermore they force the PS lipid molecules to change from laminar to hexagonal configuration, which in turn destabilize the PC:PS lipid bilayer making it prone to fuse over contact with another PC:PS membrane [80]. Other small organic molecules as *n*-hexyl bromide and short-chain alcohols are known to induce membrane hemifusion and fusion [81, 82]. Peptides [68], polymers, and drugs [83], have also been reported as fusogenic agent. The most refined and sophisticated fusogenic machinery in term of rapid vesicle fusion, is the neuronal SNARE assembly (soluble N-sthylmaleimide-sensitive factor attachment protein receptor) [78]. It is responsible for the exocytic process of small synaptic vesicles (30–50 nm) and neurotransmitter release in a sub-millisecond time scale [84]. SNARE proteins are a vast family of small transmembrane proteins with more than 36 members in

humans, 25 in *saccharomyces cerevisiae*, and 54 in *Arabidopsis thaliana* [10]. All SNARE members posses a highly conserved SNARE motif, an evolutionary characteristic that allows the identification of this protein family. The SNARE motif consists of a 60 – 70 amino acids sequence that are arranged in heptad repeats (figure 8) [85, 86]. Neuronal SNAREs have been the focus of a strong biochemical research during the past decade, which has identified three different SNARE types essential for synaptic exocytose. They are located in both the neuronal plasma membrane and the small synaptic vesicles respectively. Syntaxin and SNAP-25 are localized within the plasma membrane and are known as target SNAREs (t- SNAREs) [84]. And synaptobrevin resides in the synaptic vesicles (v-SNAREs) [10]. SNARE assembly is thought to be initiated at the N-terminal of the protein of the syntaxin/SNAP-25 complex (figure 8), and proceed toward the C-terminal transmembrane domains or membrane anchors, in a process referred to as zippering [87].
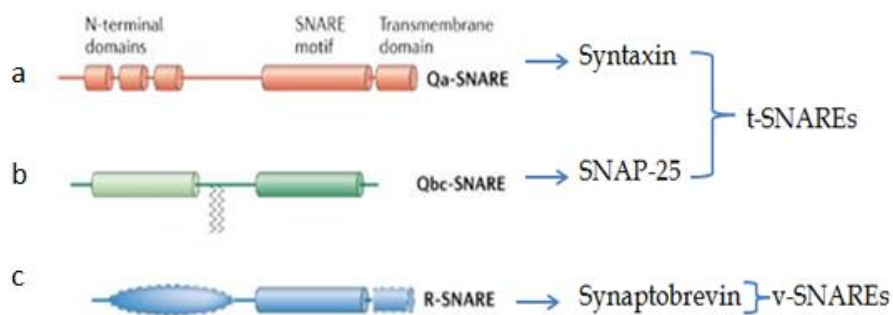
Figure 8 Domain structure of neuronal SNARE protein, a) syntaxin belong to the so called Qa-SNARE subfamily due to the highly conserved glutamine residues in its structure. It has a transmembrane domain which is connected to the SNARE motif via a short linker, the SNARE motif is linked to three antiparallel helix bundles at the N-terminal of the protein. b) SNAP-25 is a 25-kDa protein lacking of transmembrane domain, it is normally anchored to the target membrane via association with syntaxin. c) Synaptobrevin anchors the vesicle bilayer via the transmembrane domain, while the remains of the proteins interact with the syntaxin/SNAP-25 complex to trigger fusion. Image taken from [10].

How SNARE proteins trigger sub-millisecond vesicle-membrane fusion, is something which remains elusive. However experimental evidences and computational simulations, have demonstrated the existence of a large protein complex called the SNAREpin [88, 89]. It is composed by two t-SNARE, the v-SNARE, synaptotagmin (a Ca^{2+} sensor protein) [90], complexin [91], Sec1/Munc18 homologs [92], Munc13 [93], and synaptophysin [94]. These proteins cooperate together to release the energy needed to drive fusion in a sub-millisecond respond, after Ca^{2+} stimulus in the synapse. SNARE proteins assemble within the SNAREpin complex into a parallel four helix coiled-coil structure, in a *trans* configuration with their C-terminal oriented toward their respective membranes (figure 9) [95]. Recent experimental evidence using nanodiscs to inspect the SNAREpin assembly, has identified two fundamental steps in the zippering pathway of the parallel four helix SNARE proteins complex [96];

- First, the N-terminal of both syntaxin/SNAP-25 (t-SNAREs) and synaptobrevin (v-SNARE) interact to initiate the formation of the parallel four helix structure. The zippering process of the N-terminal helixes is arrested by the action of complexin, which bind to the forming SNAREpin. This intermediate step is called *half- zippered* (figure 9). The half- zippered stage is associated to vesicle-membrane docking, in addition it has been report to bend the target membrane increasing its curvature at the fusion point [97].

- In a second step, during the Ca^{2+} influx at the synapse zone, complexin proteins dissociate, setting the half- zippered SNAREpin free. The zippering process then continue toward the C-terminal portions providing sufficient energy to drive fusion; this stage is known as *fully zippered* (figure 9) [97].
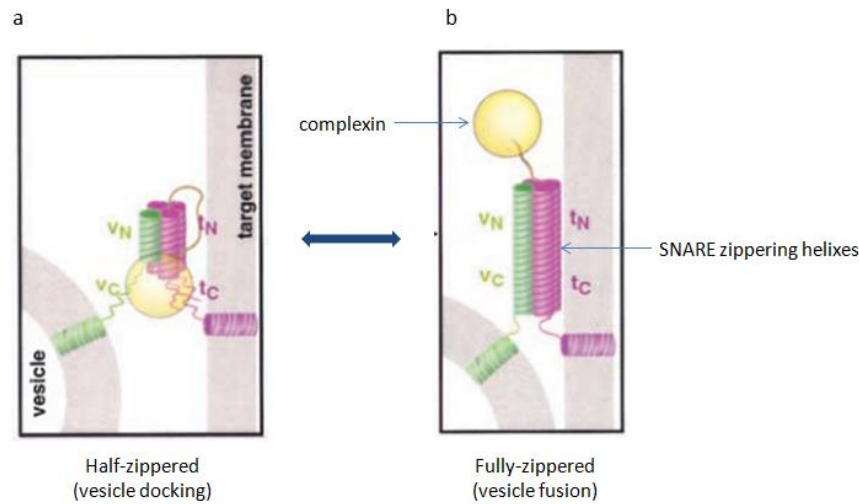
Figure 9 Representation of the two basic steps during the SNAREpin zippering process, a) the zippering SNAREpin starts from the N-terminal domains of both syntaxin/SNAP-25 (t-SNAREs) and Synaptobrevin (v-SNARE), binding of complexin proteins arrest the zippering process originating a so called half-zippered intermediate step. b) over Ca2+ influx, complexin proteins dissociate from the SNAREpin, the zippering process then continue toward the C-terminal portions providing sufficient energy to drive fusion, this stage is known as fully zippered. Image taken from [97].

In addition to the SNAREpin discovery, further in vitro experiments have demonstrated that out of the many proteins forming the SNAREpin structure. The t-SNARE/v-SNARE complex is the minimum essential machinery to trigger membrane fusion [10]. However the number of SNARE complex responsible for triggering fusion in real cells remains unknown. Preliminary evidence and models predict that 10 – 15 SNARE complexes are required to trigger sub-millisecond fusion in vivo [97]. They should organize themselves around a 1 – 2 nm fusing pore, but no conclusive evidence about the SNARE complex numbers has been reported so far. However, in vitro experiments have shown that one SNARE complex is sufficient to fuse SUVs, but the time scale of this in vitro process are in the order of 10 to 100 milliseconds far from the in vivo sub-millisecond fusion process [98]. A remarkable experiment using a high resolution dual-trap optical tweezers has calculated the force of a single t-SNARE/v-SNARE complex to be around 14 pN during the membrane fusion and its associate free energy to be 36 k_BT (k_B is the Boltzman's constant) [87].

1.2   Patch Clamp Technique

Patch clamp technique allows to control and manipulates the electric potential of a single membrane patch or the whole cell (*voltage clamp*). And record the change in membrane potential in respond to a current flowing through ion channels or action potential (*current clamp*) [99]. Thus, the investigation target of the patch clamp techniques are: voltage dependent ion channels (Na^+, K^+, Ca^{2+}, Cl^-) [100], receptor activated channels by neurotransmitters and hormones [101, 102], second messenger activated channels [103, 104], cAMP, and G proteins [105, 106]. Other important cellular parameter that can be studied via path clamping is the cell membrane capacitance [107, 108]. The membrane capacitance provides information about the surface area of the cell membrane and its changes. Continuous monitoring of cell capacitance reviles important biological phenomena as endocytosis and exocytosis in secretory cells [109, 110]. For instance, exocytosis can be measured by an increase in membrane capacitance when exocytotic vesicles fused into the plasma membrane of a cell [99, 111].

1.2.1   Patch Clamp Configurations

The very first approximation or configuration for a patch clamping recording was to attach a thin micropipette tip to a cell membrane [99]. Since then, several other configurations have been developed depending on the experimental requirement of the recording e.g., membrane integrity, membrane orientation, and continuity of the intracellular space and micropipette solution [112]. Figure 10 depicts the standard patch clamping configurations; the most important aspect of all these configurations is the formation of a very high resistance between the micropipette tip and the lipid bilayer [113]. The seal resistance normally reaches 10^9 Ω and it is better known as gigaseal [99]. Its main function is to prevent undesirable ion currents between the tip and the bilayer [114]. The basic configuration approach is called *cell-attached*, it isolates a small patch by applying a negative pressure through the micropipette to the lipid membrane (figure 10a). In

this configuration the gigaseal is a critical factor since it determines the background noise from which the transport channel current must be separated [99]. Another aspect of this configuration is that neither the lipid membrane potential nor the intracellular environment can be controlled.
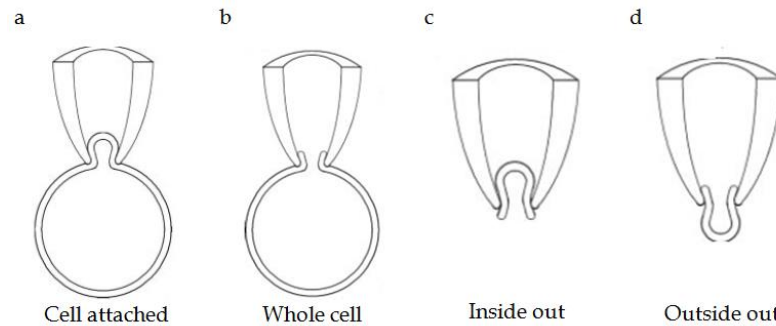
Figure 10 a) Illustration of a cell attached patch clamp configuration, b) Illustration of a whole cell patch clamp configuration, c) Inside out patch clamp configuration, d) Outside out patch clamp configuration [99].

However, if the goal of the patch clamp recording is to elucidate the influence of an intracellular component on a single transport channel current or its activity, the chosen configuration is *inside out* recording (figure 10), since it enables to change the cytosolic side of the patch to control completely the bath solution [112]. The *outside out* configuration (figure 10d), involves a resealing of the lipid membrane so that the outer membrane side faces the bath solution. This configuration is used to study how intracellular components or ligands affect a single transport channel [112]. One of the most used patch clamp configuration is the *whole cell* recording (figure 10b), in this configuration the lipid membrane is ruptured by applying a considerable negative pressure or voltage pulse to the membrane patch, controlling both the intracellular and extracellular environments of the cell [114]. With this method all ion channels in the cell membrane are recorded then, researchers may establish an average ion current response for the entire cell. This configuration is also the one used when it comes to measure lipid membrane capacitance, since it establish a low resistance and physical continuity between the cell and the micropipette lumen [99].

1.2.2 Equivalent Circuit of the Whole Cell Configuration

Since whole cell was the chosen configuration to record capacitance signals throughout the present work, an explanation of its main electrical parameters is given.
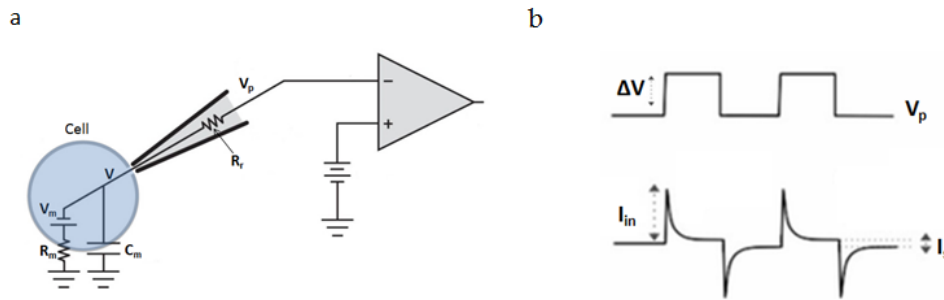
Figure 11 a) Equivalent circuit of a whole cell configuration. Cm and Rm are the cell membrane capacitance and resistance respectively, Vm is the is the cell resting potencial and Rr is the resistance associated to the attached micropipette. b) Vp is the excitation voltage and I its corresponding current response.

Biological cells possess both an intrinsic resistance and capacitance. They can be modeled by a capacitor and an electric resist in parallel. Furthermore, if we take into account the contribution of the attached micropipette during the recording signal, the equivalent circuit produced a resistant in series with the parallel cell circuit (figure 11a). If we excite the equivalent circuit with square pulses of a certain amplitude ΔV, and assuming $R_m \ll R_r$, the current response of the circuit is given by Ohm's law [112]:

$$I_{in} = \frac{\Delta V}{R_r} \quad \text{and,} \quad I_s = \frac{\Delta V}{R_m} \tag{11}$$

The rate at which the lipid membrane potential changes is dictated by the charging of the membrane capacitance and its current decays exponentially with a time constant τ, equivalent to:

$$\tau = R_\tau \, C_m \qquad\qquad (12)$$

$$R_\tau = \frac{R_m R_r}{R_m + R_r} \qquad\qquad (13)$$

1.2.3 Capacitance Measurement Technique for Lipid Bilayer

The time domain technique and *sinusoidal excitation* [115], they are known to produce the most reliable results when measuring membrane capacitance. These techniques rely on the equivalent circuit presented in figure 11a. In addition to the intrinsic micropipette resistance, it also possesses an intrinsic capacitance corresponding to the sum of the micropipette and others source of capacitance at the input of the amplifier and it is in the order of several pico-farads [99]. This capacitance is neglected in the circuit since its effects are easily compensated. *Rr* has a value on the order of $\approx$ 10 MΩ, $R_m \approx$ 1 GΩ, V_m is responsible for any *DC* current presented at the holding potential of the cell membrane [99], it can be ignored in an *AC* analysis of the circuit but is important if the *DC* current is used in the estimation process.

1.2.3.1 Time Domain Technique

If we consider a micropipette potential as the one shown in figure 11b, and the equivalent circuit to be ideal, the current response of the circuit will be given by the following expression;

$$I_{in} = (I_0 - I_s)e^{-t/\tau} + I_s \qquad\qquad (14)$$

Where, I_0 is an initial current transient, I_s is the relaxation value of the current respond, t is the time after the pulse input voltage. Right after the pulse the impedance of the lipid membrane capacitance is $C_m \approx 0$, and R_r received the whole

V_m potential [99]. After current relaxation, C_m is charged to a new voltage given the following relaxation current;

$$I_S = \frac{\Delta V}{R_m + R_r} \tag{15}$$

The time constant of C_m was described in equation (12), and the associated resistance in equation (13). Solving the mentioned equations the lipid membrane capacitance C_m is given by:

$$C_m = \tau \left({}^1\!/\!R_r + {}^1\!/\!R_m \right) \tag{16}$$

$$R_r = \frac{\Delta V}{I_0}$$

$$R_m = \frac{(\Delta V - I_S R_r)}{I_S}$$

1.2.3.2 Sinusoidal Excitation (Lindau-Neher Technique)

When the aim of the patch clamp experiment is to have a high resolution measurement of the lipid membrane capacitance or to record small capacitance variations, e.g. as a consequence of a single vesicle fusing with a lipid membrane, a sinusoidal excitation is the indicate technique to used [109]. Let us, consider a sinusoidal voltage being applied to an ideal resistance. By Ohm's law we know that the resulting signal will be a sinusoidal current having the same frequency as the applied voltage. If we now apply the same stimulus to a capacitor, the resulting current will have the same frequency as the voltage but with a phase shift of 90°. The governing equation for the capacitor is given by:

$$e^{jwt} = \cos(wt) + j * \sin(wt) \tag{17}$$

The resulting sinusoidal signal for the capacitor can be expressed as follows:

$$v(t) = Re[V_0 e^{jwt}]$$

$$i_c(t) = Re[(jwC)V_0 e^{jwt}] \tag{18}$$

We can define the expressions in brackets as the complex voltage and complex current respectively. The impedance of the circuit element is the ratio of a complex voltage to a complex current [99, 109]. Since impedance can be used to calculate complex current from complex voltage, exactly the same way as Ohm's law relates current to voltage. The impedance of a capacitor and a resistor is:

$$Z_c = {}^1/_{jwC} \quad \text{and} \quad Z_R = R \tag{19}$$

From electronics we know that the admittance Y is consider to be the inverse of the impedance Z and that they follow the governing rules used to analyze resistor networks, for the case of R_m and C_m:

$$Y = Y_{C_m} + Y_{R_m} = JwC + {}^1/_{R_m} \tag{20}$$

Now, considering the current respond of the circuit and solving the total admittance of this equivalent circuit (figure 11a):

$$Y(w) = \frac{(1+jwC_m R_m)}{R_t(1+jwC_m R_\tau)} \tag{21}$$

$$R_\tau = \frac{R_m R_r}{R_m + R_r}$$

$$R_p = R_m + R_r$$

The Lindau-Neher technique uses a Lock-in amplifier (phase sensitive detector); in our case implemented in the patch clamp software to resolve the real and

imaginary part of the admittance values, and therefore the corresponding capacitance and resistance of the lipid membrane [116].

1.2.4 Patch Clamp Amplifiers

There are two main amplifier circuits in a patch clam setup; a current to voltage converter and a lock-in. The first line of amplification in a patch clamp system is an ultra-sensitive current to voltage converter, transforming small picoampere currents from the measuring micropipette to a voltage that can be processes by a computer [99]. Small picoampere currents are measured as a voltage drop across a large resistance element, used as a feedback of an inverted operational amplifier [117]. However, a higher valued resistor increases the sensitivity of the amplifier, then a single capacitor (C_f) is used for the resistance to be almost infinitive (figure 12). The use of a feedback capacitor (C_f) lowers the Johnson thermal noise intrinsic to resistors in the order of *GΩs*. Capacitors also possess a faster respond, and have wider dynamic range compare to resistors [114]. The feedback capacitor may cause a mismatch in the frequency response of the system, therefore a differentiator is used for frequency respond correction (figure 12, A2). A switch S_f is used to discharged periodically the feedback capacitor, thus preventing the current input to cause the voltage V_1 to rise linearly with time and saturate the operational amplifier *A1* [99]. When S_f is closed the output of A2 does not reflect the input current any-longer, then a second switch S_h together with a capacitor is used to freeze the output voltage during the discharge of C_f.
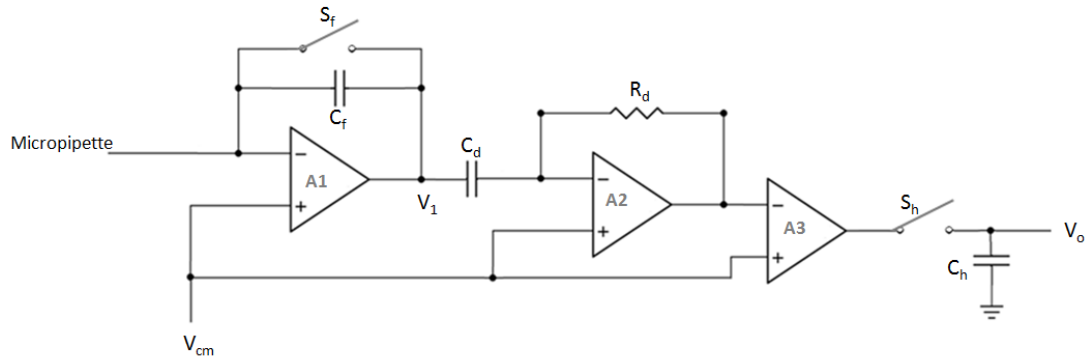
Figure 12 Current-voltage converter used as a first line of amplification in a patch clamp system

1.2.4.1 Lock-in Amplifier

In order to resolve single fusion events during a patch clamp recording, a combination of the current to voltage converter and a separate hardware lock-in amplifier is used to detect the small capacitance variation [99]. A lock-in amplifier is used to measure a very small signal whose amplitude is smaller than the noise associate to it [116]. It locks to a set frequency, filtering and discarding all others. An *AC* voltage or current is detected at the inlet and a *DC* voltage proportional to the input signal is produced [116]. Figure 13, depicts a block diagram of a lock-in amplifier; a current to voltage converter (figure 12) is used to amplify a given input signal, which is modified in its phase and magnitude. A noise level is added to the input signal due to the measurement procedure [99]. Then, the phase sensitive detector (PSD) multiplies it by the internal reference frequency. The result of this procedure is the sum of a component with the double frequency, a component of zero frequency, and the noise that was added to the input signal. The low pass filters the *AC* frequencies and only keeps the *DC* component. The level of the input signal that correspond to the same frequency and phase as the reference signal is then amplified [116].
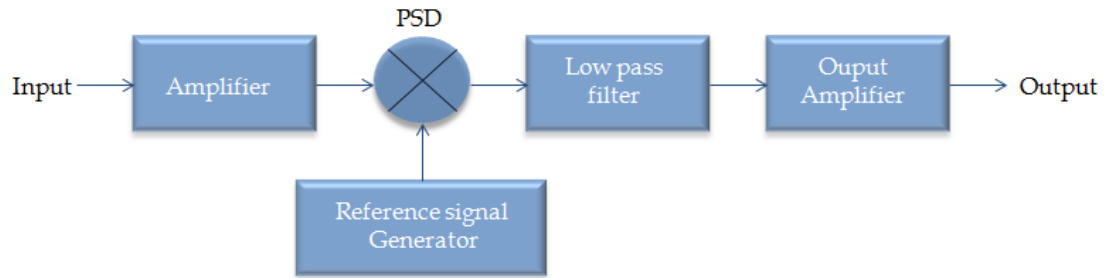
Figure 13 Block diagram of a lock-in amplifier

1.2.5 Patch Clamp Amplifier Setup

We used the EPC 10 patch clamp amplifier (HEKA, Germany) for our experimental setup; it is controlled digitally via the Heka electronics software (Patchmaster). The software provides a programmable pulse generator to excite the sample and a digital oscilloscope to monitor both the excitation signal and the sample response. The patch clamp amplifier system consists of two pieces of hardware, the probe or headstage and the main unit.

- *Headstage.* It comprises the first line of electronics for the signal processing and amplification of the sample response to a giving stimulus. Its main component is a sensitive current to voltage converter amplifier, and it also contains the electronic needed to inject signals to the amplifier. Special care has to be given to the headstage electronics, since it is very sensitive to static electricity and it may cause serious damage to its electronics. To touch or attach a micropipette to the headstage, the user must ground himself/herself to avoid any risk of damage.

- *Main Unit.* It contains the power supply, the signal processing electronics, the A/D and D/C converters and the connectors for analog and digital input/output. All the calibration adjustments are made by digital switches including those which depend on the properties of the components in the

41

headstage. The calibration parameters are unique for every amplifier and probe combination, thus if the probe need to be exchange a new hardware calibration has to be performed. Before doing a measurement with the patch clamp amplifier the main unit must be switched on, allowing a warming up of about 30 minutes. The main unit also has a high quality ground for grounding additional components e.g. a microscope.

The EPC 10 patch clamp amplifier system can be synchronized with a high speed camera and externally trigger video capturing. Among several analysis software packages for data analysis, we mostly used the in-built function called LockIn, which allows measuring changes in membrane capacitance.

Figure 14 Patch clamp amplifier system

2. Materials and Experimental Set-up

In the following chapter we give a detail description of the molecules, fabrication techniques and protocols for the microfabrication of microfluidic schemes used in the present thesis. A complete description of the experimental setup and an explanation of its main parts will be given as well.

2.1 Experimental Setup

Figure 15, depicts the experimental setup use to create and study artificial lipid and protein bilayers in microfluidics devices. We used a Zeiss Axiovert 25 phase contrast inverted microscope with 10X, 20X and 40X objective systems, the microscope was coupled to a homemade light source. Two different digital cameras were used to image artificial bilayers within the microchannels, a CCD PCO 1600 (PCO AG, Germany) providing a capturing velocity of 30 frames per second and a maximum resolution of 1600 x 1200 pixels. And a high speed camera Photron Fastcam SA3 with a capturing velocity up to 2000 frames per second at a pixel resolution of 1024 x 1024. One of the above described cameras was chosen depending on the experimental requirement for high resolution or high speed respectively. Video capturing was done with the CamWare software in the case of the PCO 1600 camera and the Photrom Fastcam viewer for the SA3 camera. Flow velocities inside the micro-chips were regulated by means of homemade syringe pumps, driven by dc motors and controlled by a program written in LapView (National Instruments Corporation). These pumps represent a volume driven system for the experiment. In case a pressure driven system is required, motor pumps can be easily substituted by a hydrostatic system to control flows in microchannels. Glass syringes of 500 µl and 1 ml (Hamilton®, Switzerland) were used to inject the test liquid within the microfluidics device. Teflon tubing was use to connect the syringes to the microfluidics devices. A patch clamp amplifier

(HEKA EPC10, Germany), was integrated in the experimental setup to excite and measure currents and capacitance of the bilayers. The connection between the patch clamp amplifier and the microfluidics chip was done via Ag/AgCl electrodes carefully inserted in the microchannels, the amplifier was control using the software Pachtmaster (HEKA, Germany).
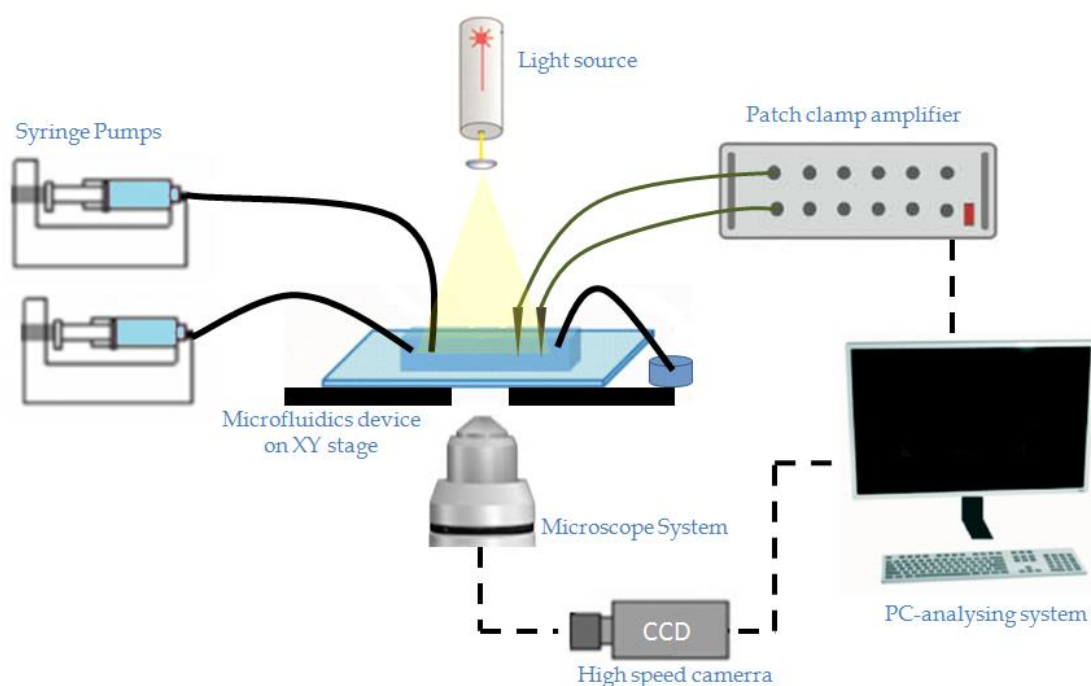
Figure 15 Experimental setup for artificial bilayers production and study in microfluidics platforms.

2.2 Lipid Molecules

Five different types of lipids were used to form artificial lipid bilayers in microfluidics geometries:

- **Monoolein:** *1-(cis-9-Octadecenoyl)-rac-glycerol (*sigma-Aldrich, Germany*),* is a relatively simple molecule composed of a single hydrocarbon chain, which is attached to a glycerol backbone by an ester bond (figure 16a). The remaining two hydroxyl groups of the glycerol moiety confer polar

characteristics to this part of the molecule (head) [118]. Thus, they may form hydrogen bonds with water in aqueous solutions. In contrast, the hydrocarbon chain (tail) is strongly hydrophobic, rendering monoolein into an amphiphilic molecule with an overall HLB (hydrophilic lipophilic balance) value of 3.8 [119]. It is partially soluble in water, but very soluble in oil and chloroform.

- **DPhPC:** it is made of a phosphatidylcholine molecule (head) and two hydrocarbon chains which have been synthetically saturated using methyl groups (tail) (figure 16b). Saturated lipids occur naturally in archaebacterial, but not in mammalian membranes. Hydrocarbon chains of DPhPC are less susceptible to photo-oxidation and degradation than unsaturated linear chain lipids (DOPC) [120, 121]. It is very soluble in oils and chloroform, and partially soluble in water.

- **DOPC:** As a natural occurring lipid, Phosphatidylcholine (PC) is in general the most abundant lipid in animal cell membranes. It has been reported to be more common in the outer leaflet of the cell membrane where it functions as part of the permeability barrier to insulate the internal chemistry of the cell [122]. It is soluble in oils, chloroform, and partially soluble in water. (figure 16c)

- **DOPS:** Phosphatidylserine (PS) is the most abundant negatively charged phospholipid in eukaryotic membranes. It is a key element directing the binding of proteins and contributes to the electrostatic association of polycationic ligands with cellular membranes, it is found mainly in the inner leaflet of the plasma membrane figure 16d) [123].
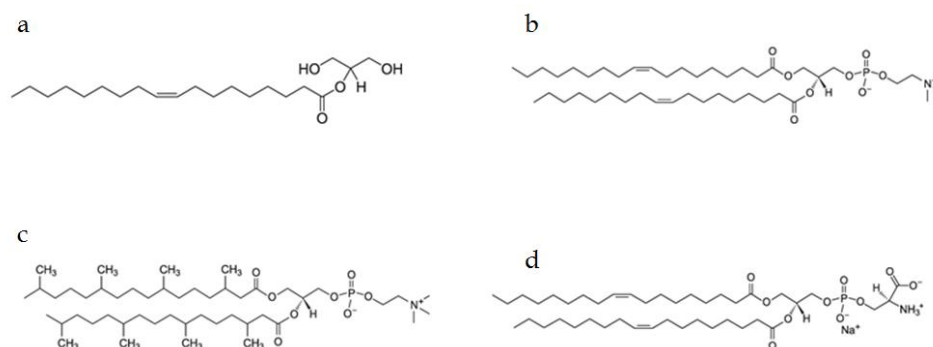
Figure 16 Chemical structure of the different lipid molecules; a) Monoolein, b) DOPC, c) DPhPC, d) DOPS.

2.3 Preparation of SNARE-SUVs

Small unilaminar vesicles (SUVs) containing both t-SNARE and v-SNARE proteins were provided by Prof. Pincet (CNRS, France). SNARE proteins were purified and reconstituted into SUVs following the protocol described in [124]. All lipids were dissolved in a 2:1 (vol:vol) mixture of $CHCl_3$:methanol. Typically, 1 µM total lipid was used, with a composition that was 73 to 83 mol % (DOPC), 15 to 25 mol % (DOPS), and 2 mol % fluorescently labeled lipids, using nitrobenzoxadiazole (NBD) or rhodamine (RHO).

2.4 Micro-device Fabrication Techniques

One of the key aspects to ensure microdevices performance and manufacturability is the material properties such as wettability, chemical resistance, optical transparency, and biocompatibility [125]. From the biological point of view glass is a perfect candidate to manufacture microfluidics devices, however glass microfabrication is a rather complex and expensive process. Polymeric materials such as PDMS, PMMA and UV-glue have become the best option for a wide range of applications due to their reduce fabrication cost, fabrication times, volume and properties. In the following a description of the fabrication technique for each polymer is given.

46

2.4.1 Photolithographic Technique

Photolithography was the primary tool to fabricate PDMS and UV-glue microdevice temples or masters. For this purpose, a clean room equipped with a state of the art uv-exposer for contact lithography was used, to optically transfer a designed microfluidics channel patterns from a photomask to a silicon wafer cover with a photosensitive material called photoresist [125]. SU-8 family (MicroCHEM) are epoxy based negative resists optically transparent and photo imageable to near UV (365 nm) wavelength radiation. A negative photoresist means that the portion of the thin film covering the Si-wafer exposed to a UV light beam crosslinked rendering it insoluble in solvents like the standard developer solution (mr-Dev600, Micro Resist Technology GmbH). We now center in the photolithography process from pattern conception to final wafer developed.

1. The process of a microfluidic device fabrication starts with the pattern conception and design by using a commercially available drawing software packages. In our case the software chosen was AutoCAD®. The pattern is then transferred to a film photomask (JD Photo Tool, UK). A photomask is an opaque polyester film with transparent areas (microchannels), and dark areas (walls). The transparent areas allow UV-light beams to pass through the mask crosslinking the photoresist on the silicon wafer, while the dark areas prevent the passage of UV-light. Figure 17, depicts the main steps in the photolithography process.

2. Prior to coat a photoresist layer, the silicon wafer is carefully rinsed with isopropanol and acetone to remove any undesirable particles. After rinsing, it is recommended to place the wafer 2 minutes on a hot plate at 200 °C for a complete solvent evaporation. An adequate amount of SU-8 (depending on the microchannel thickness) is deposited onto the wafer; i.e. 2 gr of SU-8 for a 3 inches wafer.

3. The wafer is then placed in a spin coater to uniformly spread the photoresist on its surface achieving a desirable height (thickness) *h* for the microchannels. Spin coater parameters are optimized depending on the SU-8 type and the desire film thickness (table 2). The following expression approximates the film thickness *h* for this process.

$$h = kC\, \frac{\mu}{\omega^2}^{1/3}$$

Where *C* is the initial polymer concentration, *k* is a constant, *ω* is the angular rotation velocity and *μ* is the photoresist viscosity [126].

4. Subsequently, the spin coated wafer was soft baked at 65 and 95 °C to dry the photoresist film and improve adhesion to the wafer. Immediately after soft baking the wafer is transferred to the UV exposure and placed on the sample holder. The photomask is placed onto the wafer and it is exposed to UV light (λ= 365 nm) for about 30 sec depending on the SU-8 used (table 2).

5. After exposure, the exposed wafer is placed back on a hot plate for post baking at 65 and 95 °C respectively. The post baked wafer is introduced in a small beaker containing developer solution. It is mechanically shaken and after around 5 min (depending on the SU-8), the un-crosslinked photoresist is removed from the wafer, leaving only the designed microchannel geometries on it. Now the SU-8 master is ready to be used for PDMS molding.
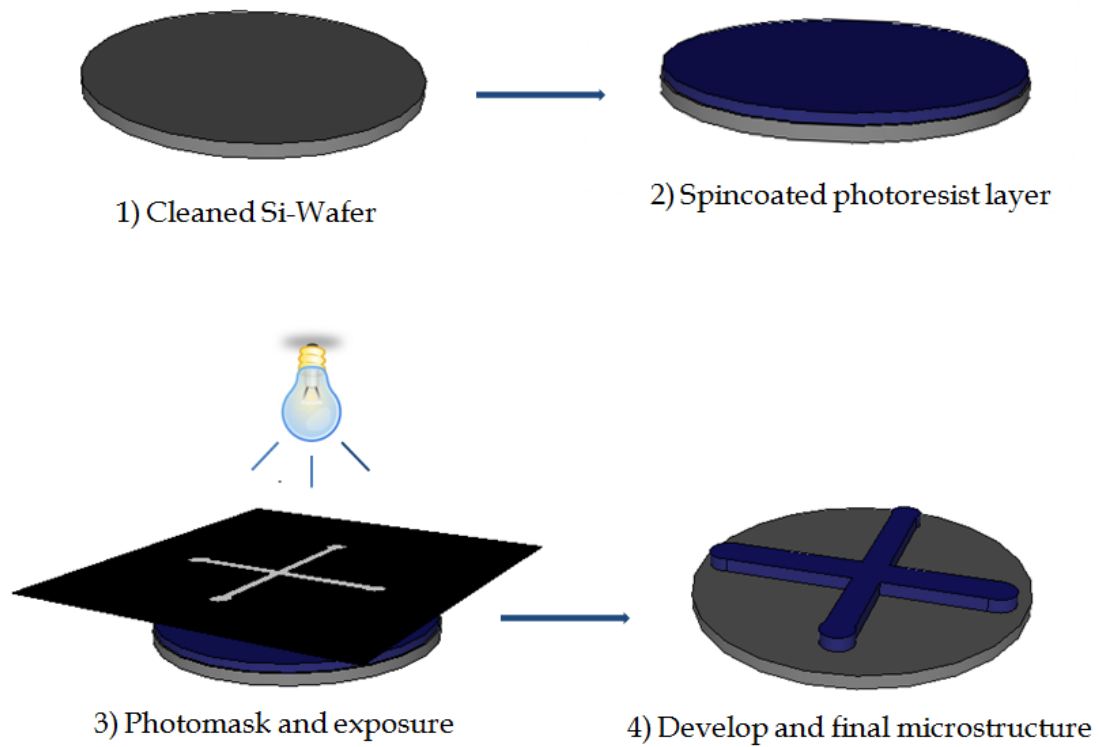
Figure 17 Microfabrication process of a SU-8 master for soft lithography. A silicon wafer is carefully cleaned with solvents to remove any dust particle, then a photoresist layer is spin coated on it. The coated wafer is exposed to UV-light, and finally the un-crosslinked photoresist is removed from the wafer leaving only the designed microchannel on it.

	SU8-50		SU8-100	
Channel height	*30 µm*	*50 µm*	*30 µm*	*50 µm*
Spincoat velocity	2000 rpm	1500 rpm	2000 rpm	1500 rpm
Soft bake 65 °C	4 min	5 min	4 min	5 min
Soft bake 95 °C	13min	15 min	13min	15 min
Exposure 15 mW/cm²	30 sec	30 sec	30 sec	30 sec
Post bake 65 °C	1 min	1 min	1 min	1 min
Post bake 95 °C	2 min	2 min	2 min	2 min
Develop	2 min	5 min	2 min	5 min

Table 2 Microfabrication parameters for different microchannel thickness using SU8-50 and SU8-100 photoresist.

2.4.2 Polydimethylsiloxane (PDMS) Molding

PDMS belongs to a family of polymers known as polysiloxanes or generally speaking silicones, which are characterized by a siloxane backbone of silicon and oxygen atoms [127]. As a material, it is non-toxic, chemically inert, biocompatible, it has a low glass transition temperature and is transparent from the visible wavelengths into the near ultraviolet wavelengths [125]. A major reason for the popularity of PDMS as a microfluidic material, is its relatively low cost and its ease of fabrication which allows a constant production of microdevices from a single SU-8 master. The PDMS elastomer Sylgard™ 184 (Dow Corning GmbH, Germany) was used to fabricate the majority of the micro-devices in the present work. Sylgard™ 184 consists of two different liquids, a liquid silicon robber base (vinyl-terminated PDMS) and a catalytic agent, which is a mixture of a platinum complex and copolymers of methylhydrosiloxane and dimethylsiloxane. The PDMS molding process is as follows:

1. The two different components of the Sylgard™ 184 kit (PDMS base and the catalytic agent) are poured in a container with a ratio of 10:1 w/w respectively, the solution is mixed for around 6 minutes to guaranty a proper mixing of the two components.

2. A SU-8 master (2.4.1) is placed in a petri dish and the PDMS/agent mixture is then poured over it. As a result of the mixing process and pouring of the PDMS solution many air bubbles are generated in the liquid and due to its high viscosity, their self-removal is time consuming. To quickly remove these bubbles the petri dish is introduced in a desiccator until all the air bubbles disappear.

3. After air bubbles removal the sample is placed on a hot plate at 70 °C for two hours since the cross-linked process via the hydrosilation reaction between vinyl groups ($SiCH=CH_2$) and hydrosilane groups (SiH) is a

temperature dependent process. After the thermal curing (solidification), a PDMS strip containing the microchannels is peeled off from the SU-8 master (figure 18). Holes have to be punched in the PDMS strip to work as inlets and outlet for the microfluidics device.

4. The final fabrication step is to plasma treated the PDMS strip surface and a clean glass slice with a low temperature oxygen plasma (Diener electronic GmbH, Germany). Upon plasma treatment the PDMS and the glass activated surfaces are brought into contact sealing the microfluidics chip (figure 18e-f). Surface plasma treatment renders the microchannels hydrophilic. To accelerate the hydrophobic recovery of the PDMS surface, the final closed device is place on a hot plate over night at 135 °C.
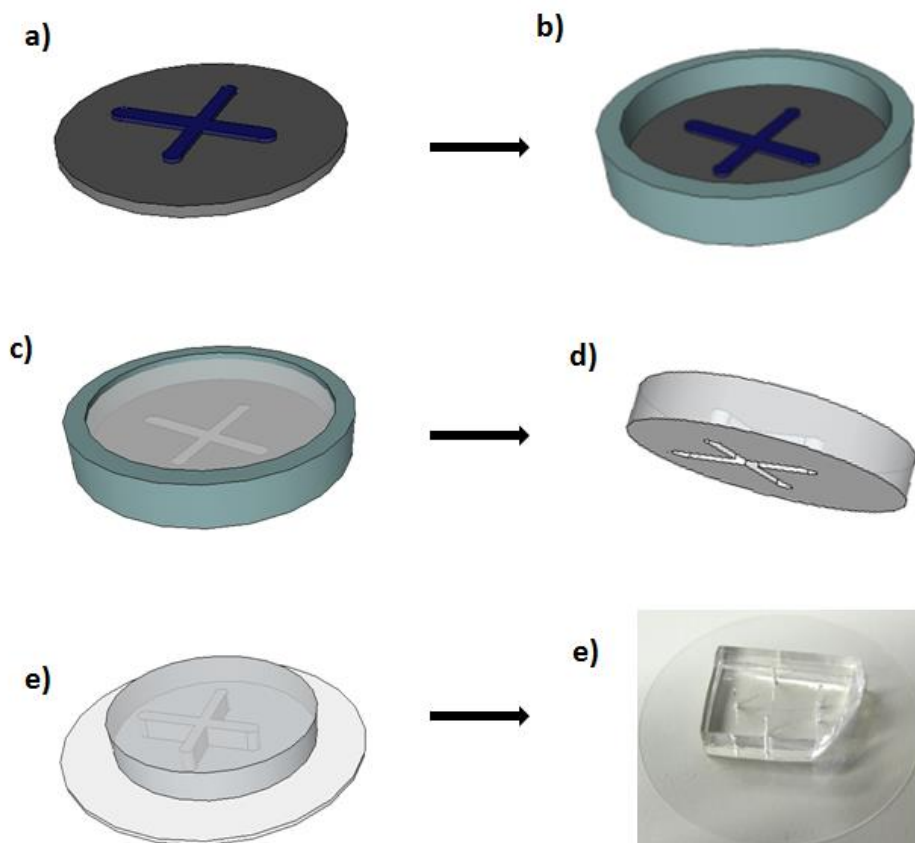
Figure 18 PDMS molding. a)-c) SU-8 master and PDMS production process, d) PDMS strip peeled off from the US-8master, d)-e) final Microfluidics device after plasma bonding and thermal hydrophobic recovery.

2.4.3   UV Glue Microdevice Fabrication Process

UV glue NOA83H (Norland Optical Adhesive No. 83H, Edmund Optics, Germany) is a fast UV curing glue that has been proved to work successfully for the fabrication of microfluidics devices. It possesses high transparency and its stiffness after intense UV light curing is comparable to PDMS. It is sensitive to the entire range of long wavelength light from 320 to 380 nanometers with peak sensitivity around 365 nm, cure times dependent on UV light intensity and thickness of the glue layer. A disadvantage of UV glue comperes to PDMS is that its surface cannot be functionalized with oxygen plasma to be bounded covalently to a glass slice. To fabricate a UV glue microfluidic device, we need a PDMS replica master, since after intense curing; UV glue can be easily removed from the PDMS strip. On the contrary, to mold a UV glue device directly from a SU-8 silicon master is a rather hard process due to the strong adhesion between UV glue and the Si-wafer after intense curing.

1. The fabrication process begins with the production of a SU-8 master using a "negative photomask" geometry (figure 19a), as a result only the photoresist at the microchannels pattern is removed after thermal crosslinking and developing of the SU-8 wafer. A PDMS strip is now molded from the SU-8 wafer using the same procedure explained in section 2.4.2.

2. Once the PDMS replica master has been successfully created, we deposited drops of UV glue on the surface of the PDMS master. Due to the hydrophobicity of the PDMS, the UV glue applied on it tends to dewet immediately, therefore a clean glass slice is pressed against the master making the UV glue spread over the whole PDMS surface. Special care has to be taken to avoid air bubble formation during this pressing process.

3. The sample is now placed under a UV lamp for 10 minutes to ensure a strong curing of the UV glue. After curing, the glass slice bonds strongly to the UV glue microchannels. Then, it is carefully removed from the PDMS master.

4. To seal the UV glue microchannels, we used a thick glass slice with holes to serve as inlets and outlets of the microdevice. We press the two glass slices against each other making sure the holes coincide with the microchannel. The sample is then placed on a hot plate at 120 °C for 10 minutes to completed the UV glue curing and ensure a strong seal between the two glass slice.

5. In order to inject the different liquid phases into the UV glue microchannels via Teflon tubing, Nanopores™ are attached to the inlet and outlet holes on the glass (figure 19b) by means of a thermo adhesive tape. The final microdevice is again placed on a hot plate at 120 °C for around 2 hours, to guarantee a perfect adhesion of the nanopores to the glass. Weight is placed onto the nanopores during the thermal bonding process.

To unbound the nanopores, the whole microfluidics device is heated up to 200 °C. The glass slices are immersed in dichloromethane to remove the UV glue. The glass slice and nanopores can be cleaned and reused to fabricate new UV glue microdevices.
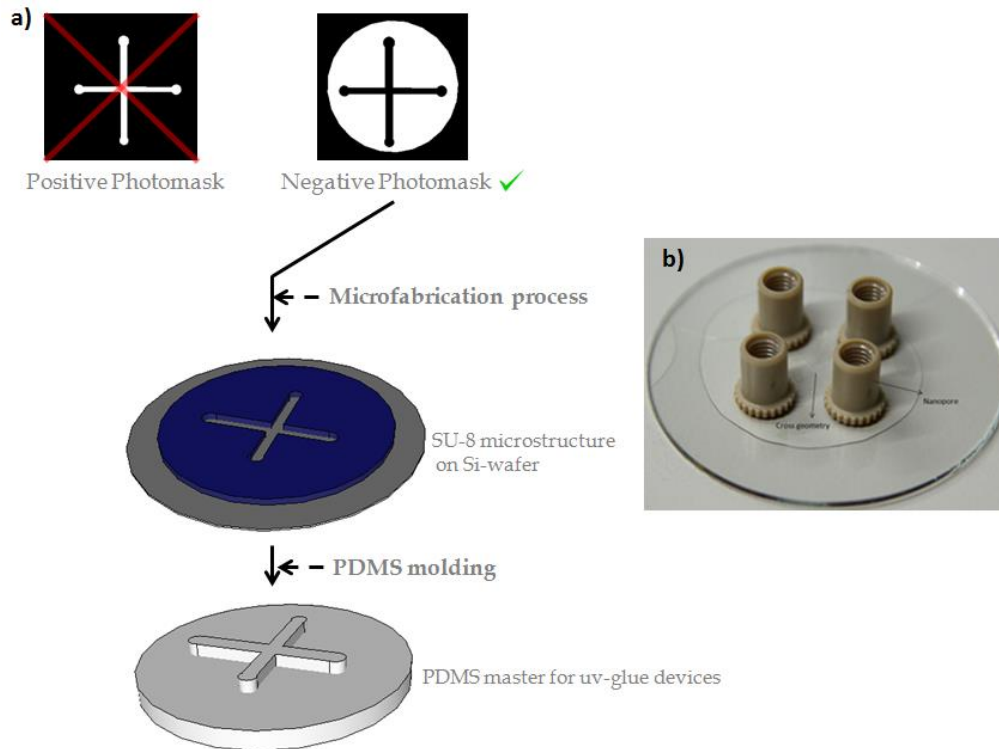
Figure 19 UV glue microfabrication process. a) PDMS replica mold fabrication, b) finished UV glue device with nanopores for liquid injection.

2.5 Microelectrode Fabrication

For a conventional patch clamp experiment, two electrodes are required; a reference electrode in the bath solution and a test electrode in the head-stage of the patch clamp amplifier. Normally, these electrodes are silver wires coated with AgCl. They provide electrical connection between the head-stage of the patch clamp amplifier and the pipette solution. In the following a detail description of the fabrication process of the two electrodes is given.

1. The first step in the fabrication of an electrode is to select an adequate pipette material for the experimental needs. The pipette will provide isolation of the Ag/AgCl wire lowering the recording noise, in addition it provides the container in which the Ag/AgCl wire contacts the bath solution. The dielectric noise parameter, which describes the AC conductivity of a glass is a key factor for the selection of pipette glass type,

for instance soft glasses e.g. soda and flint glass, present conductivity around 1 kHz that is enough to become a major source of thermal noise during the patch clamp recording. Hard glasses e.g. borosilicate and aluminosilicate have lower dielectric loss and produce less noise [128]. In the present work we selected borosilicate glass capillaries (Sutter instrument, USA) having both O.D. 1 mm : I.D. 0.5 mm and O.D. 1.5 mm : I.D. 0.86 mm to fabricate pipettes.

2. Once the adequate glass capillary has been selected. We used a P-97 Pipette Puller (Sutter instrument, USA) to fabricate the test and reference pipettes. P-97 Pipette Puller has a horizontal arrangement and applies a motorized force to pull the glass in one or multiple steps depending on the final pipette tip requirements. For microfluidics application the shape of the pipette tip is not a major concern since no special procedure such as cell gigaseal has to be performed. Therefore, the pipette pulling can be done in a single step. A ramp test was done prior to the pulling procedure; this test determines the amount of heat required to melt the borosilicate glass. The heat value established by the ramp test will depend on the heating filament type installed in the puller and the type and dimension of the glass. For the O.D. 1 mm borosilicate capillary the ramp test result was *Heat: 792 (R)*, then the following program was use for micropipette pulling; *Heat: R + 15 = 807, pull: 0, velocity:50, time: 150.* The same protocol was used for the O.D. 1.5 mm borosilicate capillary, producing similar result in the micropipette tip.

3. After micropipettes preparation we focus on the Ag/AgCl wires. New Ag wires having 250 µm in diameter (Goodfellow, Germany) were immersed in a glass petri dish with 99.8% ethanol for around 10 minutes, and then carefully rinsed with abundant Millipore water and finally dry with a nitrogen gun. Next, Ag wires were chlorided by immersing them in a 150 mM NaCl solution (8.8 mg/ml NaCl in Millipore water). The Ag wire to be chlorided contact the positive terminal of a power supply (voltcraft VLP

1303 pro, Germany). A second Ag wire contacts the negative terminal closing the circuit. A current at ≈ 1.5 mA/cm² is applied for 25 minutes. The chloriding wire darkens while the wire at the negative pole bubbles. The chlorided wires are place in a laminar flow bench to avoid dust particles adhering to them.

4. A 0.5% agarose salt bridge is prepared to work as a pipette solution by dissolving 0.5 g of agarose powder in a small beaker containing 25 ml of the 150 mM NaCl solution. To dissolve the agarose powder completely, the beaker is placed on a hot plate at 135 ˚C during approximately 30 minutes until a totally transparent liquid is reached. Preparing agarose solution may involve some danger, due to sudden explosion of the solution while heating. Normally it is prepared in a microwave oven, but during the electrode elaboration no explosion was observed even after 2 hours of continuous heating at 135 ˚C.

5. Now we have all the elements to build a reference electrode: we take one of the pulled micropipette and introduce it in the beaker containing the agarose solution to fill up the micropipette by the action of capillary forces. In case the pipette tip is to narrow it can be broken at the tip to obtain a bigger opening and fire polished to achieve a perfectly round shape. After the agarose solution has filled up the micropipette an Ag/AgCl wire is introduced, the chlorided side of the wire must reach the micropipette tip to be as near as possible to the measuring point. Before the solution solidifies a silicone drop is applied to the 0.5 mm opening of the micropipette to hold the wire and prevent contamination.

6. The same procedure as described above is performed to produce the test electrode but instead of closing the micropipette with a silicone drop, it is attached and soldered to the micropipette holder provided by Heka Electronics.
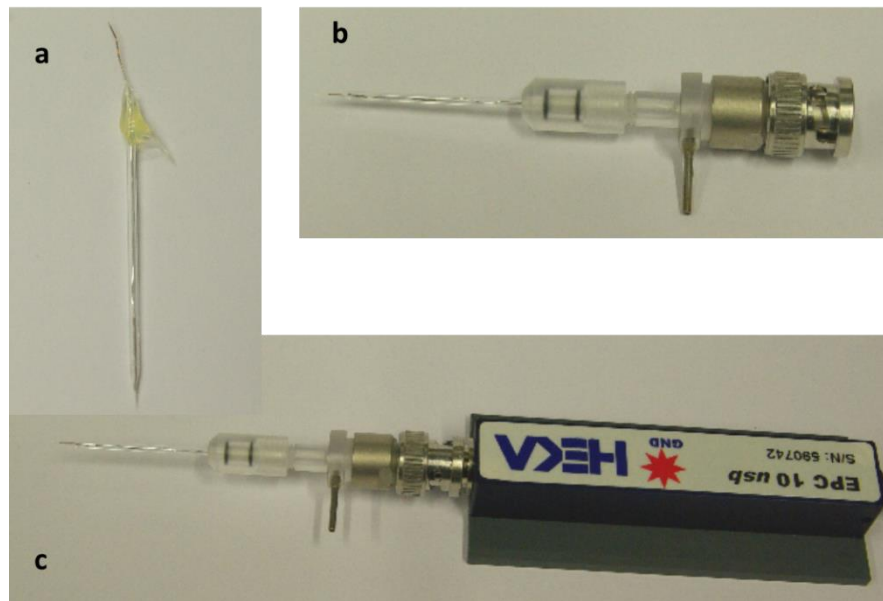
Figure 20 Electrode fabrication for patch clamping experiments. a) Ground or bath electrode, b) Test electrode and pipette holder, c) Test electrode integrated to the headstage (probe) unit.

3. Microfluidic Schemes for Bilayers Production

We present the microfluidic geometries developed for the present thesis, the main advantages and disadvantages of each geometry will be highlighted.

3.1   From Droplet Emulsion to Bilayers

Droplet based microfluidics enables the generation of controllable discrete micro-volumes by using two immiscible liquids, e.g. water-in-oil (W/O) or oil-in-water (O/W) [129]. In micro-emulsion systems, surfactants are dispersed in one of the two immiscible phases to prevent coalesces [130]. Surfactant molecules lower the surface tension, preventing coalescence and ensuring the integrity of the droplet emulsion[131]. Let us consider a water-in-oil system with Span 80 ($C_{24}H_{44}O_6$) surfactant, once the surface tension value decreased to ≈ 4.8 mN/m, each water droplet has been fully covered for a dense amphiphilic molecules monolayer. At this point two independent droplets could be brought into contact forming a surfactant bilayer at the contact area, due to the interaction of the hydrophobic tails from each monolayer (figure 21a-b). If the commonly used surfactants e.g. Span 80 ($C_{24}H_{44}O_6$) are substituted for either artificial or natural occurring lipids, an artificial lipid bilayer is created at the contact area between a pair of droplets, which resembles a natural occurring cell membrane. This constitutes a basic model to study membranes properties and their interactions with proteins in a most easy to handle and control environment. Another advantage of microfluidics system to produce lipid bilayers, is the decreased in pre-stabilization time of water droplets prior to lipid bilayer formation. Due to the continuous flow of lipid molecules in a microfluidic chip (figure 21 c-d) [132].
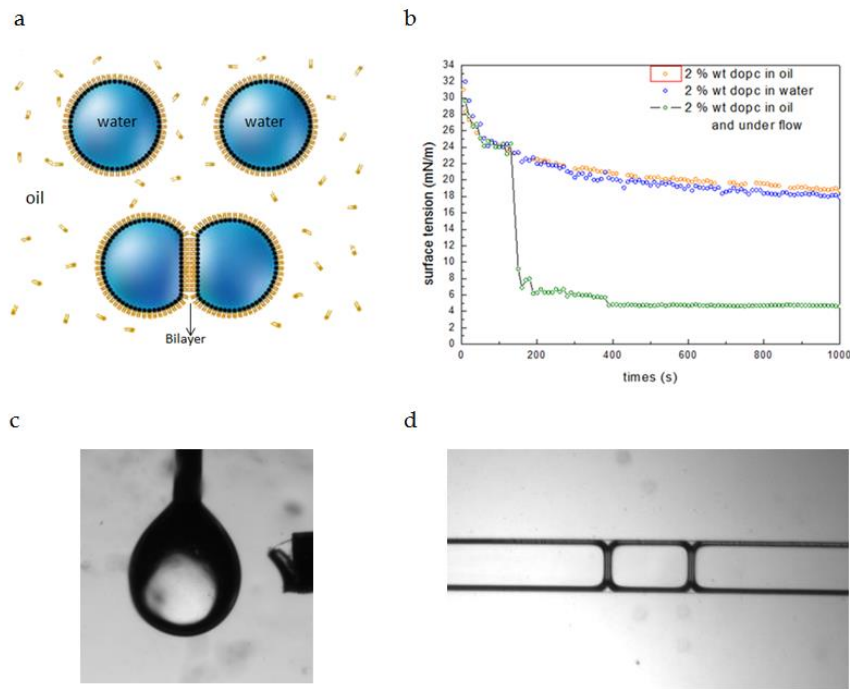
Figure 21 a) pre-stabilization time of two water drops in a lipid oil solution before forming a lipid bilayer. b) surface tension evolution over time; traces orange and blue depict a simple diffusion scenario, green trace depicts the influence of a lipid flow around the drop. c) a capillary applying a flow around a water drop. d) stable artificial membranes in a micro-channel [132].

3.2   Microfluidic Cross Scheme

The cross channel geometry was introduced by Funakoshi in 2006 [133], and since then it has become one of the most used microfluidic platforms to produce artificial bilayers. Figure 22a, illustrates a typical setup for this geometry. The test liquids (water and a lipid-oil solution) are injected into the microdevice by means of syringe pumps. Prior to bilayer formation, the device is perfused with the lipid-oil solution for about one hour to ensure a strong hydrophobicity of the PDMS micro-channel walls. Two independent water fingers are injected in the vertical channels of the cross geometry. The interfaces of both water meniscus are rapidly decorated with lipids molecules due to the transport of micelles to the interfaces [132]. After a few minutes, a dense lipid monolayer has covered the oil-water interfaces (figure 22a-b). The two water fingers are carefully brought into

contact to form a free standing lipid bilayer at the water-water interface (figure 22c-d). Special care is given to the contacting process of the water fingers, since a strong water flow may cause coalescence or uncontrollable bilayer production. To gain control over the production process, a valve was placed at the outlet channel of the cross geometry to minimize the influence of the flows. Using this geometry, lipid bilayers with a diameter up to 500 µm could be produced in a well controllable fashion.
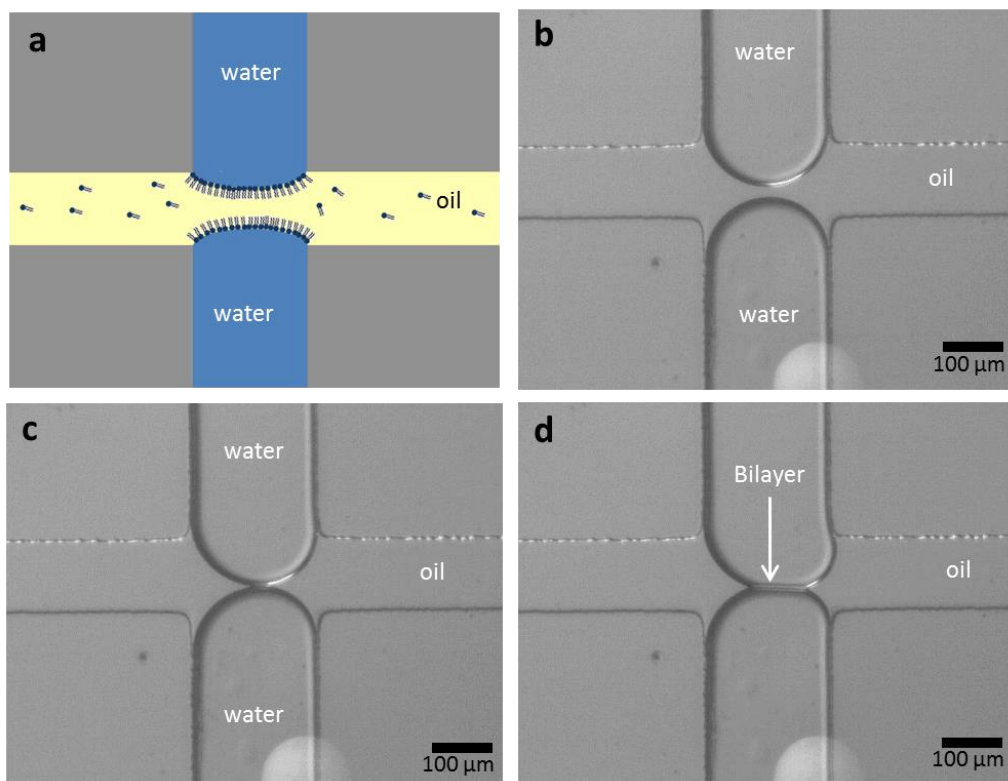
Figure 22 a) Scheme of a cross geometry setup. b) A PDMS cross geometry with two water fingers at the intersection area. c) Approximation of the water finger. d) Free standing bilayer generation.

3.3   Parallel Micro-Channels Scheme

A parallel micro-channel consists of a single wide micro-channel (main channel for the following) having only one inlet and outlet, respectively (figure 23a). The main channel is split downstream into two sub-channels by means of a geometrical step. The geometrical step possesses a gap to allow the formation of lipid bilayers (figure 23a). Either a three way micro-valve could be used to select the test liquid to be injected into the device or independent channels could be attached to the main channel prior the bifurcation, creating a T-junction like structures (figure 23b). As it was described previously the whole device is perfused for an hour with the lipid-oil solution, then water is injected into the chip displacing the lipid-oil solution throughout the main channel. The water finger is split in two fingers at the step. The two split water fingers continue to flow to the outlet reaching the channel gap. At this point they contact each other forming a lipid bilayer (figure 23c-d). An advantage of this geometry over the cross channels is its superior control over the generated bilayer, furthermore the bilayer could remain in place while the channel is being perfused. This could allow the injection of e.g. another test liquid with relevant biomolecules to study their influence on the formed membrane. Figure 23e-f, depicts this scenario, a lipid bilayer is created and after some minutes a second test liquid colored with a dye is injected into the device without disrupting the membrane, this process can be repeated throughout the membrane life time. This geometry also allows the formation of many lipid bilayers simultaneously by increasing the number of gaps in the geometrical step.

A variation of the parallel micro-channels geometry is achieved by using two totally independent micro-channels, each with its own inlet and outlet. A gap is also used to form the lipid bilayer. Controlling bilayer formation is a challenging process in this geometry due to flow fluctuation inside the device. At least four micro-valves need to be used, one per inlet and outlet respectively, in order to stop the flows in the channels (figure 23g). There are two main advantages of the geometry; the first-one is the possibility of creating asymmetric bilayers, it means that the lipid composition is different for each monolayer (figure 23h). The second-

one is the possibility of conducting experiments to affect only one of the monolayers in the lipid bilayer while the other remains intact.
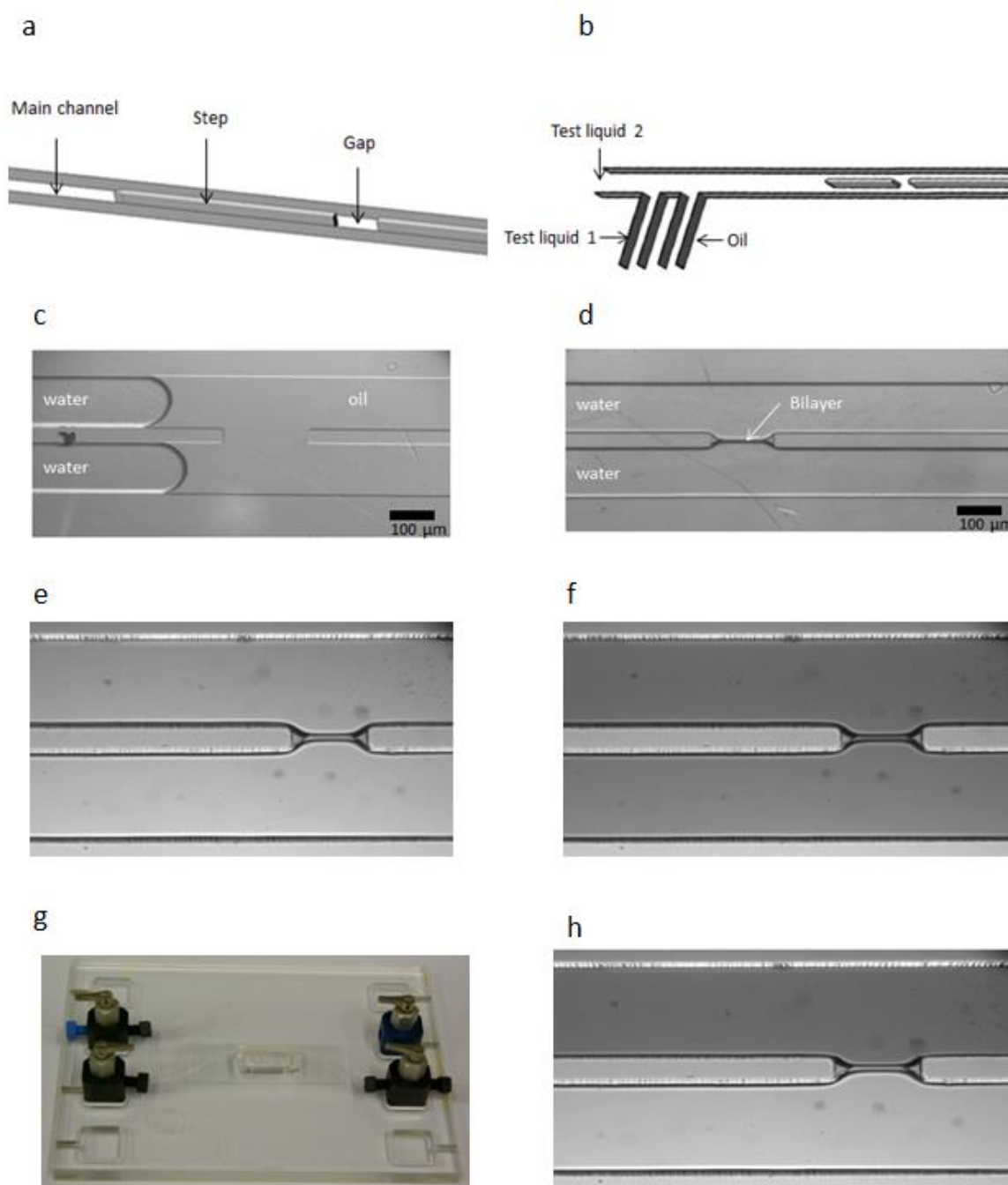
Figure 23 a) schematic view of a Parallel micro-channels. b) T-junction like structures. c)-d) free standing bilayer generation. e)-f) flow of different test liquids throughout membrane life time. g) four valves setup to control individual Parallel micro-channels, h) asymmetric bilayers formation.

3.4   Microfluidic Schemes for Lipid Bilayer Interactions

In the following, we will describe the microfluidics platforms used in the present work to study lipid membrane interaction.

3.4.1   Modified Cross Geometry

By a slight modification of the cross-channel geometry (section 3.2) we are able to form two independent lipid bilayers in a very controllable fashion. The horizontal channel was modified to have a Y-junction before the channel intersection (figure 24a). One of the Y-junction channels is used to inject the lipid-oil solution into the device, while the two droplet fingers are brought face to face to the intersection area. After some minutes a lipid monolayer covers both water fingers. The oil flow is stopped and a third water finger is injected by the second channel of the Y-junction displacing the lipid-oil solution in the horizontal channel (figure 24b). Special care has to be given to the flow velocity of the third water finger, since a high flow prevents a fine control of the bilayer formation process. A slow flow velocity allows the water fingers at the vertical channel to contact each other favoring the formation of a single bilayer instead of two. Within the time frame of the water-oil displacement, the third water finger is decorated with a lipid monolayer. All three fingers are brought into contact creating two independent free standing bilayers facing each other (figure 24c-e). The two bilayers are kept separated by continuously flushing water from the Y-junction channel, to allow the interaction of the two bialayers a gentle flow is applied at each inlet of the vertical channel moving both lipid bilayers towards each other. The details and physics of the membrane interaction will be explained in chapter 4.
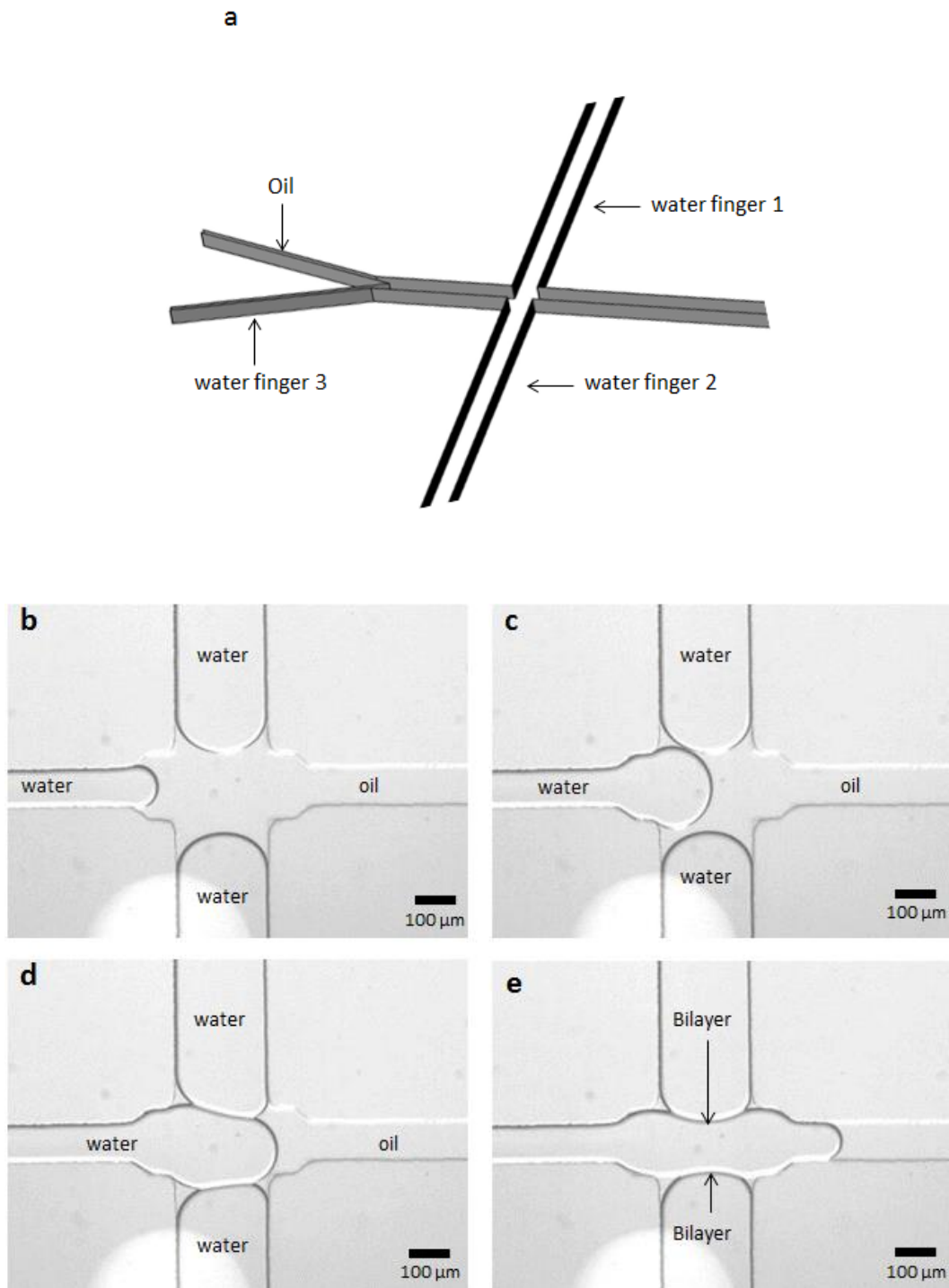
Figure 24 a) cross channel modification to form two free standing lipid bilayers b) oil displacement by a third water finger. c)-e) two free standing bilayers formation process.

3.4.2 Three Parallel Micro-Channels Scheme

Using a channel as the one described in section 3.3, it is possible to created two lipid bilayers facing one another, by increasing the number of geometrical steps in the main channel (figure 25a). The water finger entering the geometry is split in three at the steps; they flow in each of the three micro-channels displacing the lipid-oil solution throughout the device. After a successful surfaces lipid coverage, two free standing lipid bilayers are created at the micro-channel gaps as a result of finger interactions (figure 25c-d). The same result is achieved by using three totally independent parallel micro-channels, each having a valve at each inlet and outlet, respectively. The control over membrane generation is more difficult than in the wide channel case but, it has the advantage that to induce membrane interaction is enough to apply a flow at the top and button micro-channel while their respective outlet valves are closed and the middle micro-channel valve remains open.

A modification of the central micro-channel, by introducing a Y-junction at its inlet (figure 25d), allows the formation of two asymmetric membranes facing one another. Through each of the Y-junction micro-channels different lipid-water solutions are injected (figure 25d). If both lipid-water flows are adjusted to the same velocity and due to the laminar flow characteristic governing such a system, the two different lipid-water solution flow in the middle channel one on top of the other without a significant mixing of both solution (figure 25d). In this way two asymmetric free standing bilayers are created at the micro-channel gaps (figure 25e-g).
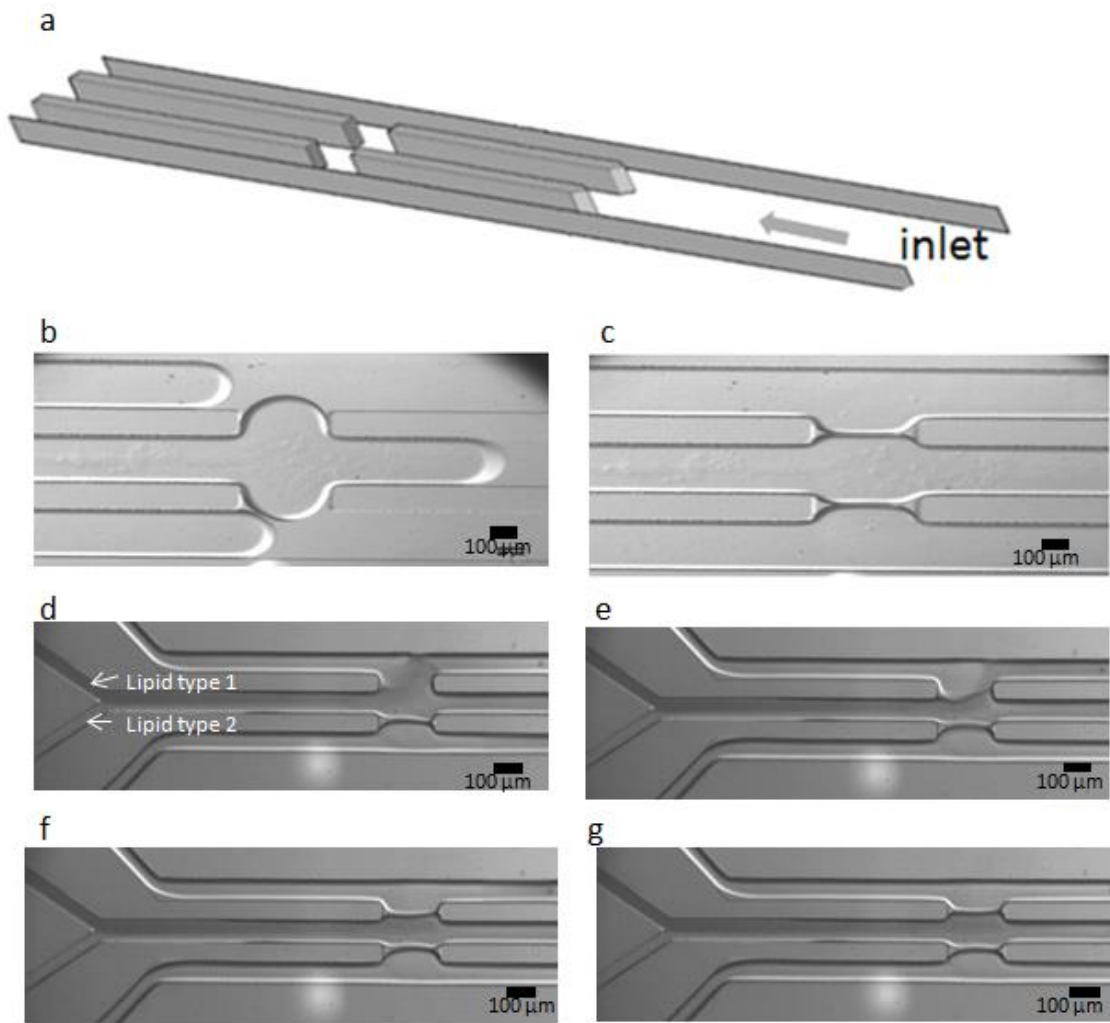
Figure 25 a) Three Parallel Micro-Channels Scheme b)-c) two free standing bilayers formation process d) schematic view of the three independent parallel micro-channels geometry. e) – g) free standing asymmetric bilayers generation.

4.   Interaction Between Lipid Bilayers

In the present chapter we explore the dynamics of individual free standing lipid bilayers formation and bilayers interaction leading to a controlled generation of intermediate fusion state (hemifusion). For this purpose we used the microfluidic scheme described in chapter 3, allowing for simultaneous optical and electrophysiological measurements.

4.1   Dynamics of Lipid Bilayer Formation

A cross geometry device made of PDMS, plasma-bond to a cover glass slice was used to produce artificial lipid bilayers (section 3.1), the liquid flows were volume controlled and the entire process was monitored by optical microscopy and supplemented with a patch clamp amplifier. Monoolein, DPhPC, and DOPC were used as lipid molecules dissolved in squalene or a mixture of squalene-decane and decane-mineral oil respectively (Table 3). A phosphate buffer (pH=7) was used as a polar phase. As it was discussed in chapter 3, once the lipid-oil solution contacts the buffer phase, lipids molecules create a monololayer at the oil-buffer interface. When the two buffer fingers are brought into contact, the lipid monolayers interact to form an artificial lipid bilayer (figure 26). To understand the dynamics of the membrane formation process we used a high speed camera (Photron SA-3) set to a minimum of 1000 frames per second and a high magnification of the monolayers contact area.
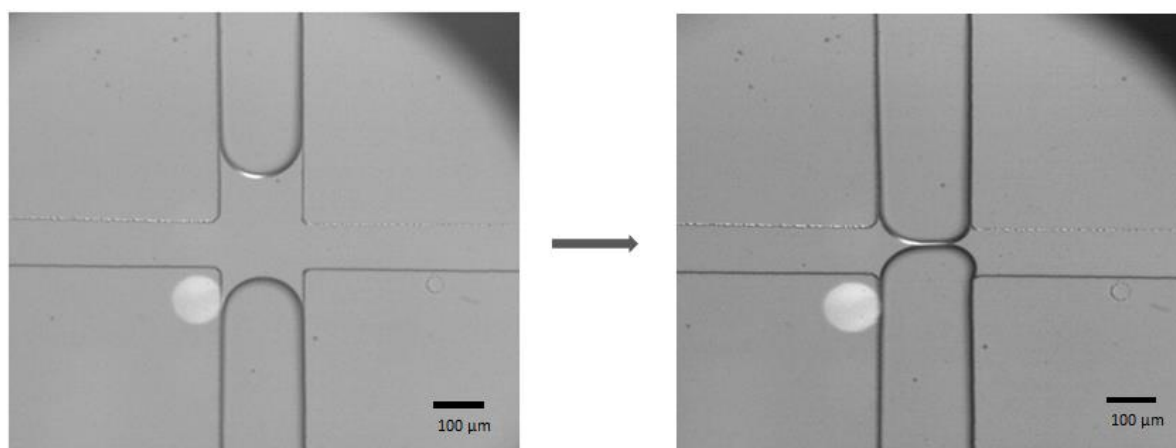
Figure 26 Formation process of an artificial lipid bilayer; the horizontal channel was perfused with a monoolein-squalene solution, and two buffer fingers are injected in the vertical channel.

Lipid Molecule	Concentration	Non-Polar Phase	Polar Phase
Monoolein	8 mg/ml	Squalene	Phosphate buffer
DPhPC	7.5 – 15 mg/ml	Squalene	Phosphate buffer
DPhPC	15 – 30 mg/ml	Decane–mineral oil/Squalene [25-75%], [50-50%] and [75-25%]	Phosphate buffer
DOPC	5.5 – 12 mg/ml	Squalene	Phosphate buffer
DOPC	12 – 25 mg/ml	Decane–mineral oil/Squalene [25-75%], [50-50%] and [75-25%]	Phosphate buffer
POPC	5.5 – 12 mg/ml	Squalene	Phosphate buffer
POPC	12 – 25 mg/ml	Decane–mineral oil/Squalene [25-75%], [50-50%] and [75-25%]	Phosphate buffer

Table 3 Lipid-oils concentrations used to create artificial lipid bilayers.

Figure 27, shows details of the bilayer formation process; seconds after contacting the water fingers, a wave is observed propagating along the forming free standing bilayer followed by a change in brightness of the lipid bilayer area. This wave corresponds to the drainage (expulsion) of the oil film as a result of the hydrophobic tails interactions of the opposed lipid monolayers (zipping process). It is worth to mention that the zipping process does not start immediately after fingers contact, it seems to be a rather random process. The displacement of the oil always starts from one side of the contact area and moves with constant velocity towards the opposite side of the forming bilayer (figure 27a). A sudden start of the monolayer-zipping somewhere in the middle of the contact area was never observed during the experiments. The velocity of the bilayer zipping process may be described as the first derivative of the created lipid bilayer's diameter with respect to time; it can be extracted from the recorded frames by measuring the lipid bilayer area, and the zipping time. The results for the four different types of lipids (DOPC, DPhPC, monoolein and POPC) used in the present work are plotted in figure 27b. It is interesting to note that the observed zipping velocities of DOPC, monoolein and POPC (0.9, 0.5, and 0.3 µm/ms respectively) scale with an accuracy of about 20 % with the membrane interfacial tension (4.1, 0.9, and 1.8 mN/m). The comparison of the various determined values can be found in Table 4.
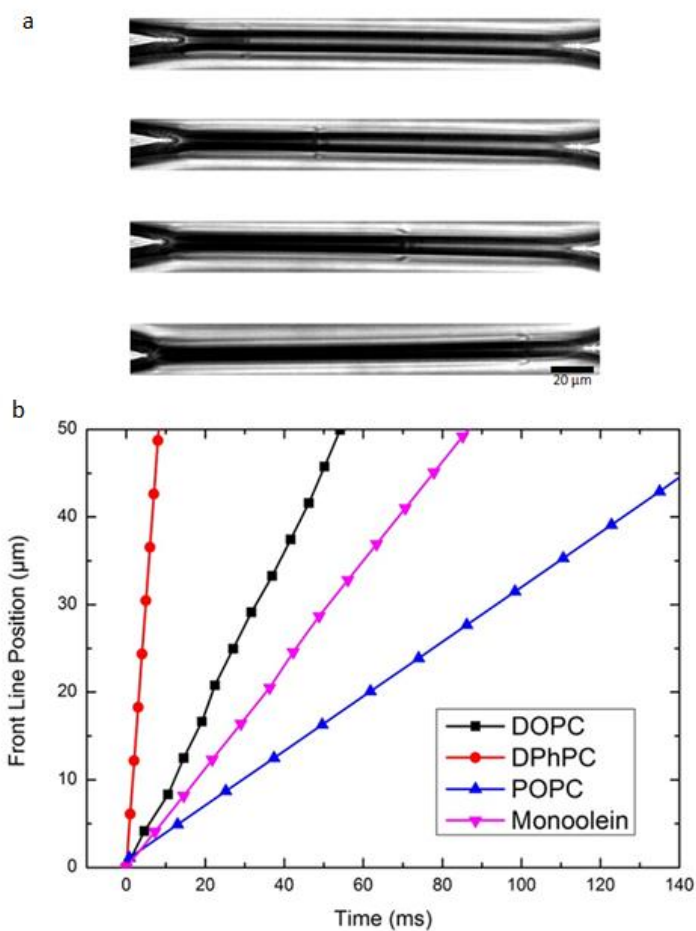
Figure 27 a) time-resolved micrograph of a free standing lipid membrane formation in a microfluidic system. b) front line position as a function of time for four different types of lipids.

	DOPC	**DPhPC**	**POPC**	**Monoolein**
Surface tension γ (buffer-oil interface) [mN/m]	4.1	4	0.9	1.8
Contact angle θ (single bilayer) [deg]	22	23	23	23
Membrane tension $\Gamma = 2\gamma \cos\theta$ (single bilayer) [mN/m]	7.6	7.36	1.66	3.31
zipping velocity dL/dt (single bilayer) [μm/ms])	0.92	6.09	0.32	0.54

Table 4 Table summering the experimental values of surface tension γ, contact angle θ, zipping velocity dL/dt, membrane tension Γ for all the lipid molecules used in the experiments.

The lipid bilayer formation process was simultaneously monitored with a path clamp amplifier. A test and ground electrodes were inserted carefully through the PDMS device at the two inlets of the vertical channel (figure 28a). Capacitance traces were recorded using the built-in lock-in function of the *patchmaster* software. Patch clamping results show that the lipid bilayer formation is not an immediate process, corroborating the observed optically. Rather, it seems to emerge from a two steps process as tested for the four different lipids. Figure 28b shows a normal capacitance trace recorded during the formation of a single monoolein bilayer; when the two monolayers are first brought into close proximity, a contact area is formed having a capacitance value of $C \approx 17 \, \text{pF}$. The specific capacitance was calculated to be $C_s \approx 0.54 \, \text{mF/m}^2$, indicating a thickness of the contact area of $d_1 \approx 36 \, \text{nm}$. The calculated initial thickness of the contact area is about one order of magnitude larger than the typical thickness of a monoolein membrane ($\approx$ 3 nm) [134], suggesting that an oil film of about 33 nm thickness is still present between the two monolayers (figure 28b). After the two monolayers are a few seconds in contact, the capacitance value measured across the contact area increases suddenly (within about 250 ms depending on the lipid type) to $C \approx 200 \, \text{pF}$. Subsequently to the sudden increase a further slow increase in the total capacitance signal is observed which corresponds to a further increase in contact area, due to the buffer flow (Figure 28b). The area increase comes to a hold when the geometric limitations of the microfluidic device are reached. The corresponding thickness of the contact area with 200 pF was calculated to be 3 nm ($C_s \approx 6.3 \, \text{mF/m}^2$) for monoolein. For the DOPC, DPhPC, and POPC the resulting bilayer thickness was 5.5 nm. These values are in agreement with lipid bilayer thickness reported in literatur meaning that the two monolayers, which were separated by an oil film after initial contact, have self-assembled into an oil-free bilayer. The above described free standing bilayer formation process is highly reproducible and a solvent free bilayer can be safely assumed when the initial two monolayers are in contact for times longer than a few seconds.
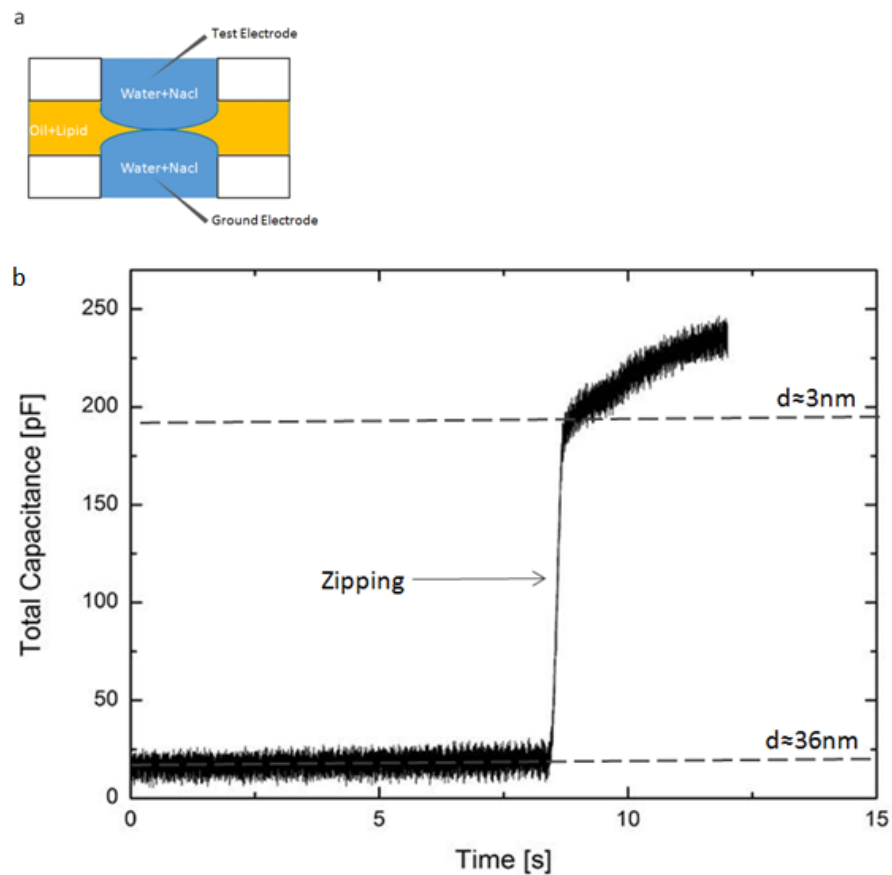
Figure 28 a) Experimental setup; test and ground electrodes were inserted through the PDMS device at the two inlet of the vertical channel, a buffer solution at 150 mM NaCl was used as electrolyte solution b) Total capacitance trace and thickness reduction of the lipid membrane.

4.2   Membrane Fusion Intermediate (Hemifusion)

We produced two parallel (face to face) oil-free lipid bilayers, which are brought into contact with one another. The entire process is monitor by direct optical visualization and simultaneous capacitance measurements. Figure 29a, shows a photographic sequence of a lipid bilayer interaction process.
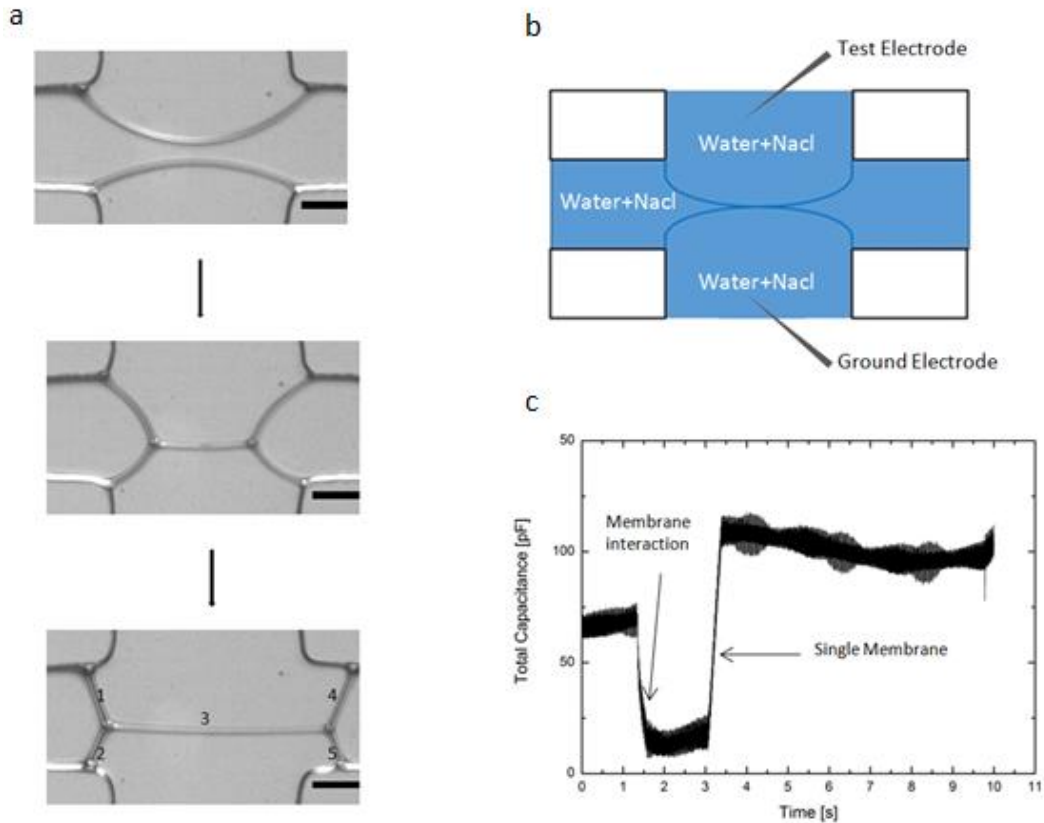
Figure 29 a) Image sequence of two parallel DPhPC bilayers interaction process. After bilayer interaction a single lipid bilayer emerged and propagated in the horizontal channel. b) Schematic view of the corresponding microfluidic situation. c) Total capacitance trace of the bilayers interaction process.

As a result of the interaction process it can be observed that the two water fingers in the vertical channel did not coalesce. Moreover a single lipid bilayer emerged and propagated in the horizontal channel (figure 29a). By analyzing the total capacitance trace we can understand the dynamic of the interaction process (figure 29c). In a first stage, a capacitance value close to ≈ 60 pF is registered, this value correspond to the two parallel lipid bilayers before contacting them. In a second stage, a sudden drop in the capacitance trace is observed, it corresponds to the appearance of additional bilayers 1, 2, 3, 4, 5 (Figure 29a bottom picture). In a third stage, an increase in total capacitance is observed following the same fashion of a single lipid bilayer formation process (section 4.1). It seems to be that as a result of two bilayers interaction process, a single bilayer is produced (bilayers "3" Figure 29a bottom picture). To prove the previous statement, we have to eliminate the

contribution of bilayers 1, 2, 4, 5 (Figure 29a bottom picture), guarantying a measured capacitance signal from the interesting contact area, bilayer number 3 in figure 29a (bottom picture). To avoid any undesirable capacitance contribution from the other resulting bilayers, the water finger injected in the horizontal channel contains ultra-pure water, free from any salt (Nacl). While in the vertical channel the water fingers contains Nacl (figure 30a). The capacitance trace obtained during the first seconds after converging two DPhPC bilayers is displayed in figure 30b. At $t \approx 0$ s, the two bilayers are touching each other as determined from optical measurement and the total capacitance value is equal to $C \approx 40$ pF. This capacitance value stays stable until $t \approx 6.5$ s, when a spontaneous increase of the capacitance value to $C \approx 200$ pF is observed. The capacitance value further increases, due to an increase of contact area.
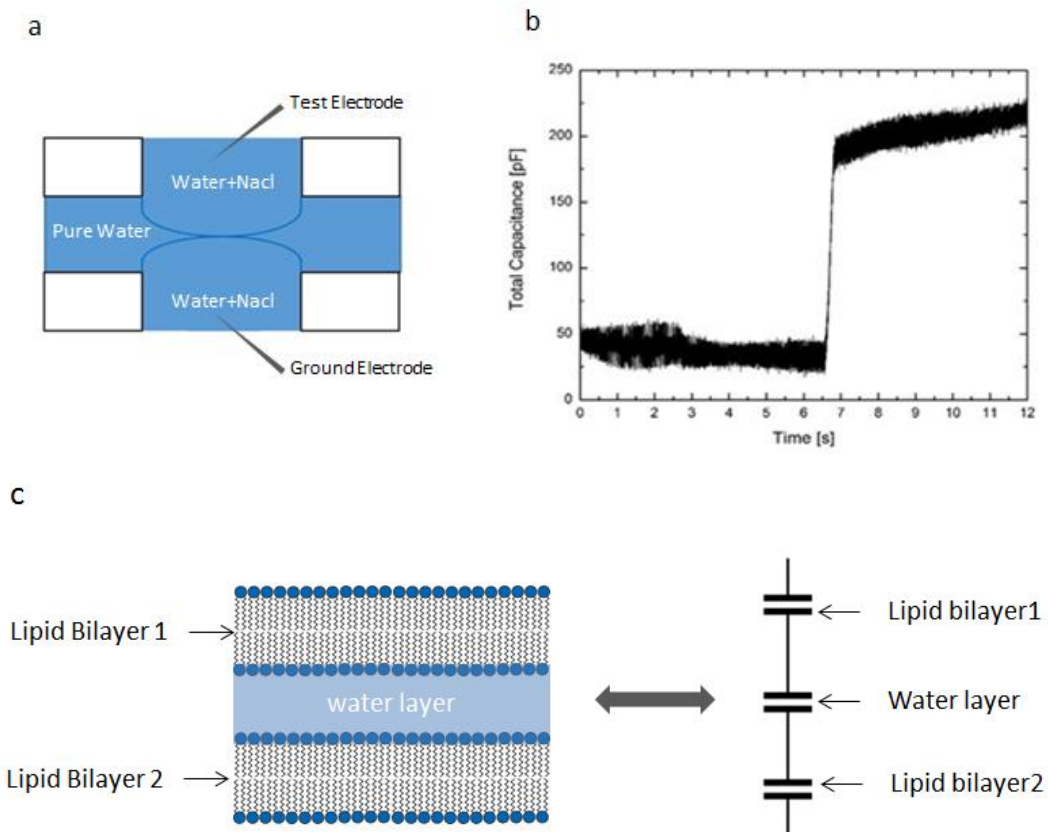
Figure 30 a) Schematic view of the corresponding microfluidic situation; it is important to note that there are no ionic charges into the middle channel. b) Total capacitance measurement during the interaction of two DPhPC bilayers. c) equivalent circuit of three dielectrics in series considered to calculate the thickness of the water layer separating two lipid bilayers.

Using the optically measured contact area, the specific capacitance at the initial bilayers contact is calculated to be $C_s \approx 0.75 \ mF/m^2$. The layered system consists of a thin water layer sandwiched between two solvent free bilayers. To calculate the thickness of the water layer, an equivalent circuit of three dielectrics in series is considered (figure 30c). Using the dielectric constants of the involved lipids $\epsilon_l \approx 2.2$ and that of pure water $\epsilon_{water} \approx 88$, yields:

$$\frac{1}{C_s} - \frac{2d_{DPhPC}}{\epsilon_0 \epsilon_L} = 0.64 \ \mu m \tag{22}$$

0.64 µm represents the thickness of the water film separating the two oil-free lipid bilayers. Following the total capacitance trace, a sudden increase in the capacitance value is measured (figure 30c), the specific capacitance at this point is calculated to be $C_s \approx 3,78 \ mF/m^2$ revealing a reduced thickness of only ≈ 5 nm of the contacted DPhPC bilayer, which corresponds to the expected thickness of a single lipid bilayer [29]. This demonstrates that the analyzed structure which emerges at t ≈ 6.5 s after contacting the two lipid bilayers is indeed a hemifused state [77, 135]. This hemifused state is long-living, and can be stabilized for more than 1 hour. Moreover, no rupture of the resulting single membrane (i.e. fusion event) could be observed without external stimulation. From these findings we may conclude that this state of hemifusion can be considered as an equilibrium state.

4.3   Dynamics of Hemifusion Diaphragm (HD) Expansion by Simultaneous Optical and Capacitance Inspection

Now, we analyze the above explained fast formation of a hemifusion diaphragm in more detail, by comparing the simultaneous recorded capacitance trace and the optical high speed micrographs. This allows a better understanding of the dynamic of the HD formation process. After some seconds of bilayer-bilayer contact, a symmetry breaking is observed at the contact area (figure 31a). This symmetry breaking starts at a random position within the contact area of the two bilayers, and finally the hemifusion diaphragm is created. Zooming in the bilayers contact area, the symmetry breaking resembles a travelling wave localized and reflected several times within an area of 10-30 μm. During these fluctuations an initial HD region is formed within ≈ 10 ms and the capacitance trace increases from ≈ 40 pF to ≈ 100 pF (figure 30b). Assuming the just formed initial HD area to have the thickness of a single lipid bilayer ≈ 5 nm, the thickness of the remaining water layer can be calculated to about ≈ 150 nm. It is remarkable that the initial thickness of the water layer is reduced by about 500 nm during ≈ 10 ms. After the initial HD region is formed, distinct structures emerge at the boundaries of the HD area (contact lines) which travel both outwards from this area, see figure 31b.
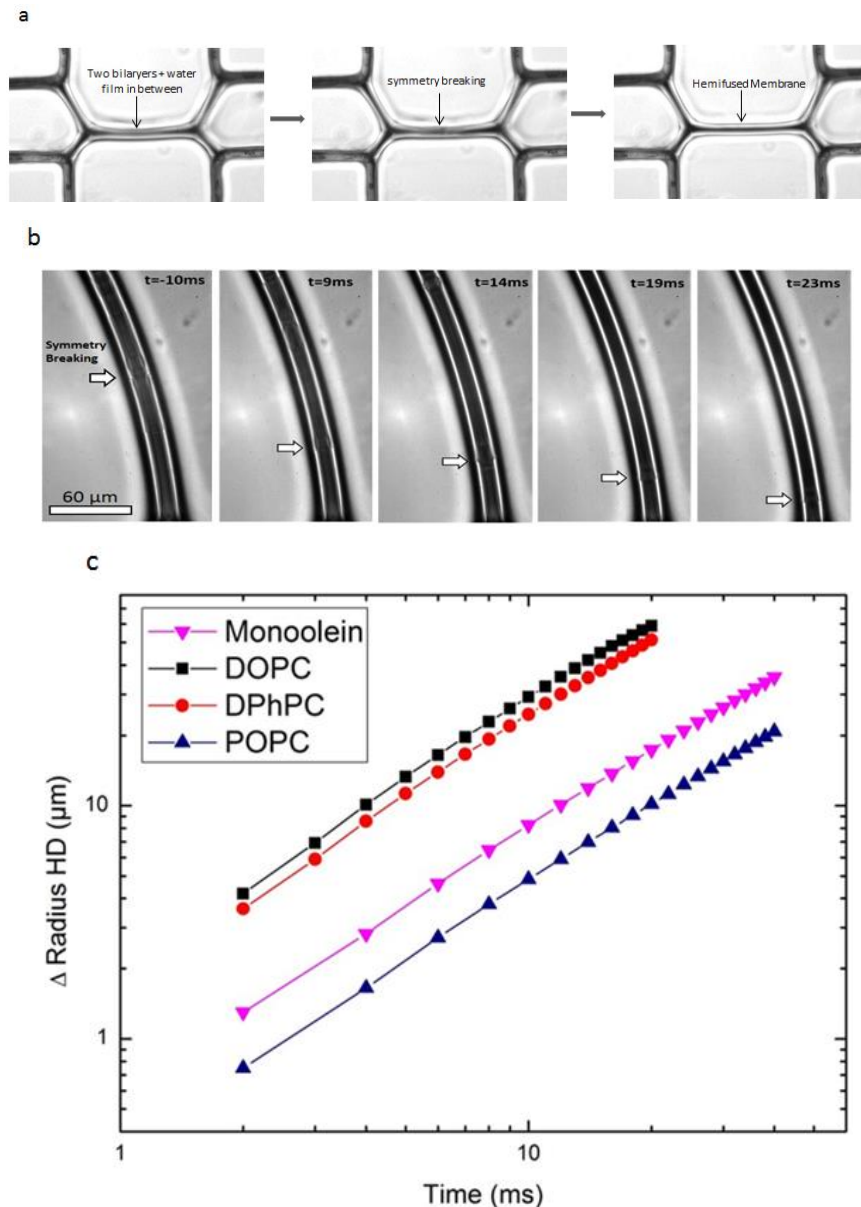
Figure 31 a) Bilayer contact, symmetry breaking, and final hemifused membrane. b) Microscope series showing the evolution of two interacting DPhPC bilayers during a dewetting process, the white arrow is indicating the border of the HD region during time evolution. c) HD radius as function of time plot, the radius evolution R is indicating a linear power law dependence function of time with an exponent equal to 1,14 ; 1,11 ; 1,09 ; 1,08 for DPhPC, DOPC, Monoolein and POPC respectively.

The increase in radius of the travelling contact lines is very fast ≈ 1 mm/s and linear in time ($\Delta R \sim t^{1,1}$) for each of the test lipids; DPhPC, DOPC, Monoolein, and POPC. The fast and linear drainage velocity could indicate that the further expansion of the HD region is driven by a dewetting with no-slip boundary conditions process of the confined water film [136, 137]. For a dewetting process

the velocity $\frac{d\Delta R}{dt}$, should scale linearly with the spreading coefficient, i.e. the membrane tension Γ, For an equilibrium hemifused bilayer the membrane tension can be expressed as:

$$\Gamma_{HD} = 2\,\Gamma\cos\theta_{HD} \tag{23}$$

Here, Γ is the membrane tension of a single bilayer which can be calculated from the measured surface tensions of lipid decorated oil/water-interfaces and θ_{HD} is the contact angle of the hemifused membrane, which can be determined from the optical micrographs. Using those values reveal that the drainage velocity, $\frac{d\Delta R}{dt}$, scales linearly with spreading coefficient, Γ within a accuracy of about 15%. Based on these findings we can additionally calculate the increase in hemifused area A_{HD} during the dewetting process (figure 32a), by using a capacitance model circuit, where the non-dewetted area and the dewetted area are in parallel (figure 32b), by solving the capacitance model circuit we have that:

$$A_{HD}(t) = \frac{A_{total}B - \frac{C(t)}{\varepsilon_0\varepsilon_L}}{B - \frac{1}{d_{DPhPC}}}\;\;with\;\; B = \frac{\varepsilon_{water}}{2d_{DPhPC} + d_{water}} \tag{24}$$

Assuming the thickness of the non-dewetted area $(A_{total} - A_{HD})$ as constant $\approx$ 150 nm (water plus two bilayers) and the thickness of the dewetted area A_{HD} as $\approx$ 5 nm (single bilayer) the increase of the hemifused area A_{HD} can be determined to $A_{HD} \propto t^2$, in agreement to the radial expansion expected for a dewetting process. Thus we may conclude that the further growth of the hemifusion diaphragm after formation of an initial hemifusion area can be identified as a dewetting process. It is remarkable that the growth rates observed for free standing hemifusion diaphragms (~ 1 mm/s) are about five orders of magnitude larger than observed for supported bilayers (~ 0.01 µm/s) [138]. Considering the observed initial fluctuations and the following dewetting process it is immediately clear that the presence of a solid support will significantly influence the drainage process. Moreover, supported bilayers experience Van der Waals forces from the substrate,

which additionally affect the forces acting on the membrane. The massive influence of a solid support can be also seen by similar measurements determining the formation of hemifused states between giant unilamellar vesicles (GUV) in bulk [139]. The observed formation speeds (~ 4 µm/s) are about two orders of magnitude smaller than observed here, and the kinetic growth of the HD area is linear with time.
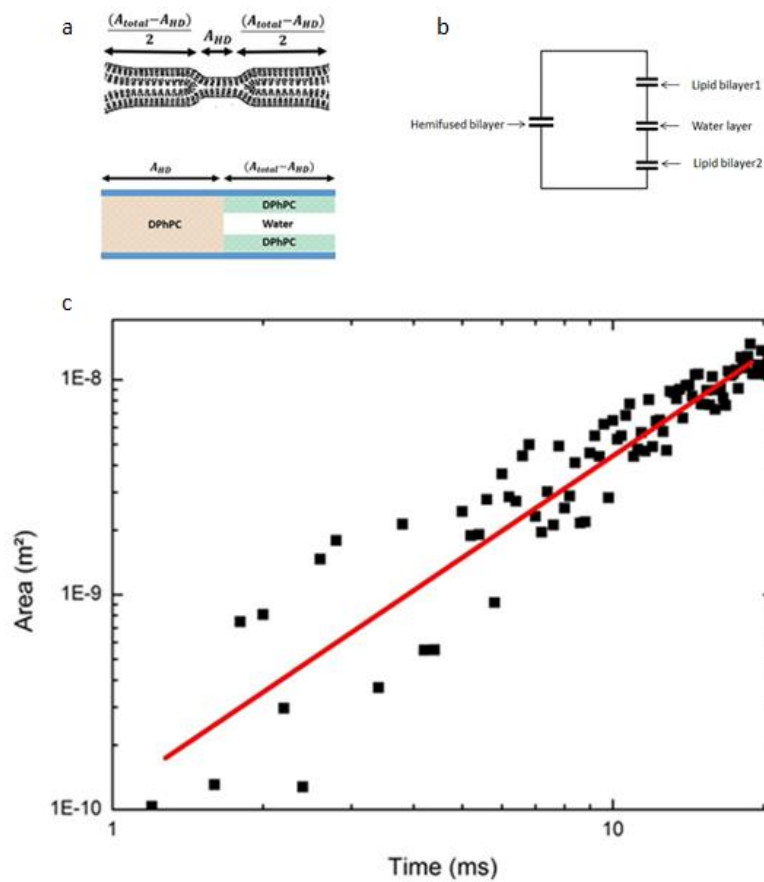
Figure 32 a) Schematic representation of the proposed dewetting mechanism that leads to hemifusion. b) Schematic representation of the corresponding dielectric circuit during the dewetting mechanism. c) Calculation of the HD area A_{HD} as a function of time t from total capacitance measurements. The area evolution A_{HD} is indicating a quadratic power law dependence function of time with an exponent equal to 1,9 for DPhPC molecules.

	DOPC	DPhPC	POPC	Monoolein
Membrane tension $\Gamma = 2\gamma \cos\theta$ (single bilayer) [mN/m]	7.6	7.36	1.66	3.31
Contact angle θ_{HD} (hemifused state) [deg]	55	54.5	54	56
Membrane tension $\Gamma_{HD} = 2\Gamma \cos\theta_{HD}$ (hemifused state) [mN/m]	8.7	8.54	1.95	3.7
Radius of HD growth velocity dR/dt (hemifused state) [μm/ms]	2.95	2.57	0.52	0.89

Table 5 Table summering the experimental values of membrane tension Γ for a single and hemifused bilayer and the Radius of HD growth velocity for a single state of hemifusion. These values are reported for DOPC, DPhPC, monoolein and POPC molecules.

4.4   Realization and Characterization of a Membrane Electrofusion Event

As we demonstrated previously, the hemifusion diaphragms formed for all tested lipids are very stable and can be considered as equilibrium or dead end state. To drive such a stable hemifusion diaphragm to fusion, certain proteins (SNAREs) could be incorporated into the bilayer (chapter 5). Alternatively, a sufficiently large electric field can be applied across the hemifusion diaphragm to trigger lipid membrane fusion (electro-fusion), as commonly used to fuse mammalian cells or synthetic vesicles [65]. Here, electro-fusion is applied as the easiest possibility to trigger the fusion of a single and stable hemifusion diaphragm. As no ionic charges are dispensed in the horizontal channel (figure 30a). Only the central bilayer of the hemifusion diaphragm is targeted when applying a voltage across the hemifusion diaphragm. The measured current signal during such a voltage ramp with continuously increasing voltage amplitude is shown in figure 33a for a monoolein-HD. The signal is reversible for applied voltages up to about $U \approx 210$ mV as long as only subcritical hydrophilic nanopores are appearing due to the applied voltage. From the membrane capacitance determined in this electroporation region, the effective membrane thickness d can be calculated and plotted as a function of the applied trans-membrane voltage, (figure 33b). From the effective bilayer thickness d, the

corresponding critical radius of nanopores r_c can be found applying equation (6). The transmembrane voltage reduces the critical radius of the pore, which is obtained by $\Delta W(r, U) = 0$.

$$r_c(U) = \frac{\sigma}{\Gamma + \frac{\varepsilon_o(\varepsilon_{water} - \varepsilon_L)}{2d}U^2} \tag{25}$$

Using this approach, the critical radius can be calculated to $r_c \approx 2.8\,\text{nm}$ for $U \sim 10\,\text{mV}$ and $r_c \approx 0.7\,\text{nm}$ for $U \sim 210\,\text{mV}$. This small critical pore radius explains that fusion is triggered when applying a voltage larger than $210\,\text{mV}$ for sufficiently long times whereas the breakdown voltage is observed to about $U_c \approx 300\,\text{mV}$, as observed in figure 33c-d. This HD-breakdown voltage is lower than the breakdown voltage of $U_c \approx 500\,\text{mV}$ reported for a free standing monoolein bilayer in a similar geometry [134]. This difference is probably due to the increased membrane tension in the state of hemifusion.
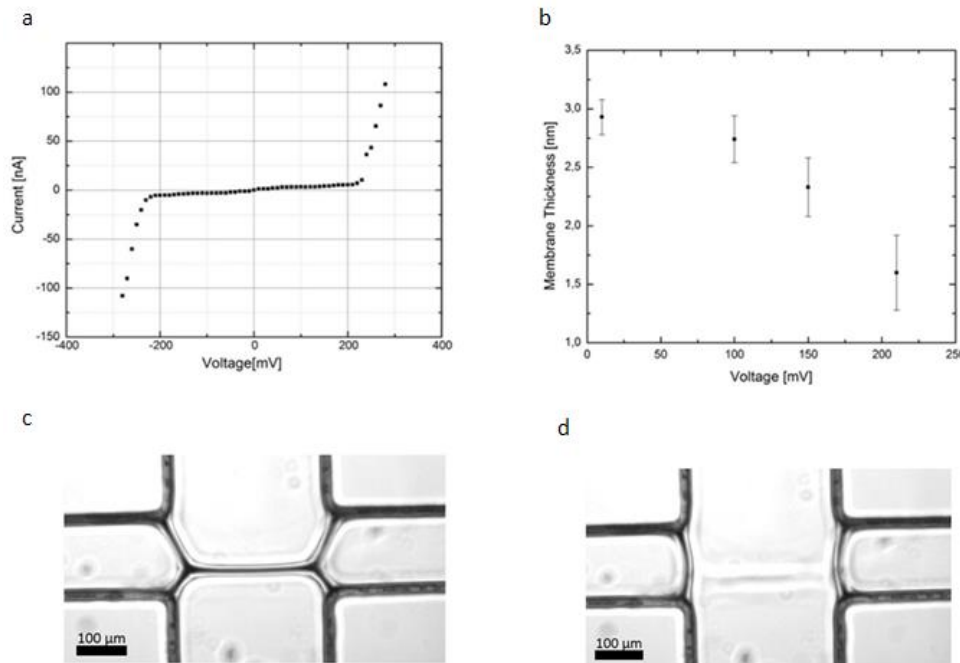
Figure 33 a) Direct measurement of a ionic transport as function of the applied voltage with a hemifused monoolein membrane. b) Evolution of a hemifused monoolein membrane thickness as function of the applied voltage. c) Single fusion event.

5. SNARE Mediated Fusion of Single Vesicles with Free Standing Lipid Bilayers

In the present chapter we address the insertion of fusogenic proteins (SNAREs) in free standing lipid bilayers. Furthermore we study single fusion events between a lipid bilayer and SUVs mediated via SNAREs interaction. Single fusion events are inspected using both optical and electrophysiological measurements.

5.1 Free Standing Lipid Bilayer for SUVs Fusion

Lipid bilayer composition is important to mediated vesicle fusion. We used a binary lipid system composed of 90% DOPC and 10% DOPS in squalene to produce free standing lipid bilayers. PC lipids are neutral molecules while, PS lipids are negatively charged. The present of charged PS molecules is intended to maintain an electrostatic repulsion between the free standing lipid bilayer and the small unilamellar vesicle (SUVs), avoiding spontaneous fusion events to occur. The microfluidic scheme introduced in section 3.2, was used to produce the respective lipid bilayer. Prior to each SUVs fusion experiment, the lipid membrane thickness was measured via the specific capacitance parameter as described in section 4.1, ensuring no oil film between the lipid membrane.

5.2 t-SNARE Proteins Delivery to Free Standing Lipid Bilayer

t-SNARE proteins were reconstructed into the bilayer of SUVs (from now on called T-SUV), having a DOPC/DOPS lipid composition with 15-25% PS lipids and 2% of fluorescent labeled lipids (NBD/Rhodamine). The protein to lipid ratio was 200:1, and the SUVs size was about 50 μm resembling the size of synaptic vesicles (30–50 μm) [140]. As mention earlier, PS lipids present in both the free standing lipid bilayer and the SUVs experience an electrostatic repulsion

preventing spontaneous fusion to happen. A fluorescent test was done in order to confirm the non-spontaneous fusion assumption. Figure 34a shows a fluorescent image of a free standing lipid bilayer created by bringing together two buffer droplets (125 mM KCl and 10 mM HEPES) containing T-SUV. No fluorescent markers are observed in the lipid membrane region, the process was continuously monitored for 45-60 minutes, which is the time scale of our experiment. Thus we may infer that the lipid composition of both the free standing lipid bilayer and SUVs effectively repulse each other by the present of PS lipids and non-spontaneous fusion occurs.
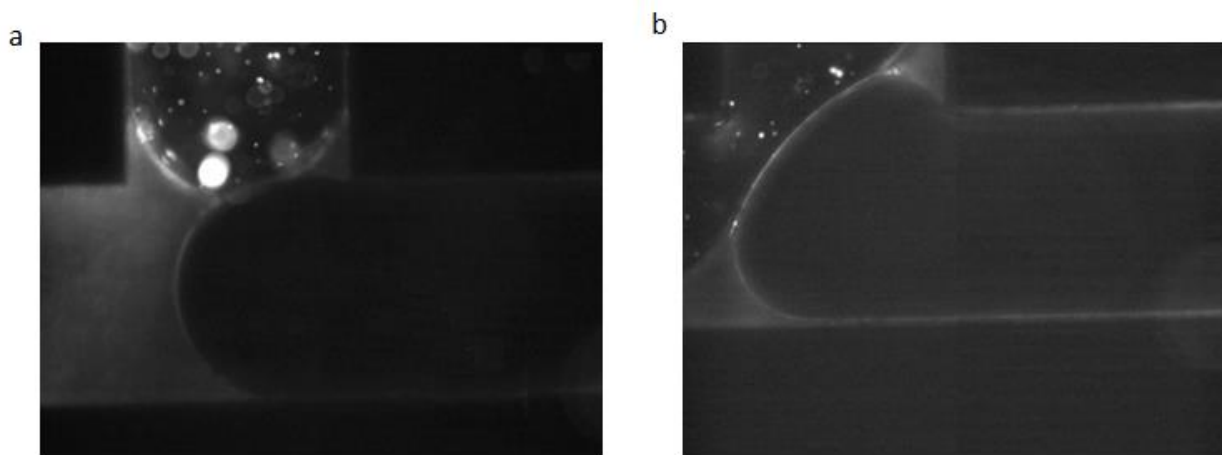
Figure 34 a) the droplet on top contain fluorescent T-SUVs, while the bottom contain only buffer solution, the lacking of fluorescent markers in the free standing lipid bilayer confirms that no spontaneous fusion of the T-SUVs occurs. b) reproduction of the previous scenario but this time a 25mM CaCl2 was added to the buffer composition, fluorescent markers in the lipid bilayer region infer the T-SUVs to bilayer fusion. *Images courtesy of Dr. Fleury.*

t-SNARE proteins where inserted into the free standing lipid bilayer by the action of divalent cations Ca^{2+}. Figure 34b, shows the same scenario described previously in which two buffer droplets containing T-SUVs are used to create a lipid bilayer. A 25mM CaCl2 was added to the previous buffer composition (table 6). After 10 minutes fluorescent signals can be clearly seen at the lipid bilayer region (figure 34b). It means that Ca^{2+} ions present in the buffer successfully induce the fusion of the T-SUVs to the free standing lipid bilayer. The negative PS headgroups readily adsorb the Ca^{2+} ions, forming bonds through the carboxylate oxygen of the PS

headgroups. Thus reducing the electrostatic repulsion between the lipid bilayer and the T-SUVs, favoring fusion. Furthermore, the uptake of Ca^{2+} by the negatively charged sites of PS headgroups causes the formation of *trans* Ca^{2+}-phospha-tidylserine complex. This brings the negatively charged PS headgroups close together forcing the hydrocarbon tails of the lipid bilayers to face the hydrophobic phase [68], thereby adopting a H_{II} phase. As a result of the H_{II} phase formation; there is an increase of lipid bilayer interfacial tension resulting in lateral compressibility and structural defects. These changes in PC:PS bilayer surface is extremely necessary for destabilization of the lipid bilayers resulting in membrane fusion.

Buffer composition	T-SUVs composition POPC/POPS	Lipid membrane composition POPC/POPS	Fusion activity
125mM KCl and 10mM HEPES	7.3:2.5	9:1	Negative
125 mM KCl, 10 mM HEPES, 10 mM $CaCl_2$	7.3:2.5	9:1	Negative
125 mM KCl, 10 mM HEPES, 15 mM $CaCl_2$	7.3:2.5	9:1	Negative
125 mM KCl, 10 mM HEPES, 25 mM $CaCl_2$	7.3:2.5	9:1	Positive

Table 6 Fusion essay for T-SUVs and a free standing lipid bilayer system. Vesicle fusion is observed when 25 mM CaCl2 is added to the Buffer solution.

The previous experimental results demonstrate that indeed a transfer of fluorescent lipids occur from the T-SUVs to the free standing bilayer. However, from the fluorescent image is not evident that whole T-SUVs are incorporated in the lipid bilayer. For instance SUVs may be either sitting on top of the bilayer or hemifused to it. We performed A fluorescence recovery after photobleaching (FRAP) test to inspect the mobility of the fluorescent labeled lipids incorporated into the free standing lipid bilayer (Appendix, A2). Figure 35, depicts the fluorescent recovery experiments. Firsts, a FRAP test was carry out on a pure

PC/PS membrane having 2% NBD. By using a soumpasis fit the diffusion coefficient for the lipid molecules was found to be 7,5 μm²/s. As a second step, T-SUVs were allowed to fuse to the free standing lipid bilayer in the present of Ca²⁺, over a period of 30 minutes. After photobleaching the fluorescent recovery follows the soumpasis fit as in the previous case and the diffusion coefficient for the lipid molecules was 7,5 μm²/s. The later result shows that the fluorescent lipid molecules coming from the T-SUVs are fully incorporated in the free standing bilayer. If there would be any T-SUVs partially attached to the lipid bilayer a deviation in the Soumpasis fit should be expected and the fluorescent recovery should have some discrepancies with respect to the pure PC/PS experiment. At this point we may conclude that Ca²⁺ trigger effectively the fusion of T-SUVs with free standing bilayer guaranteeing a successful delivery of T-SNARE protein into the lipid membrane.
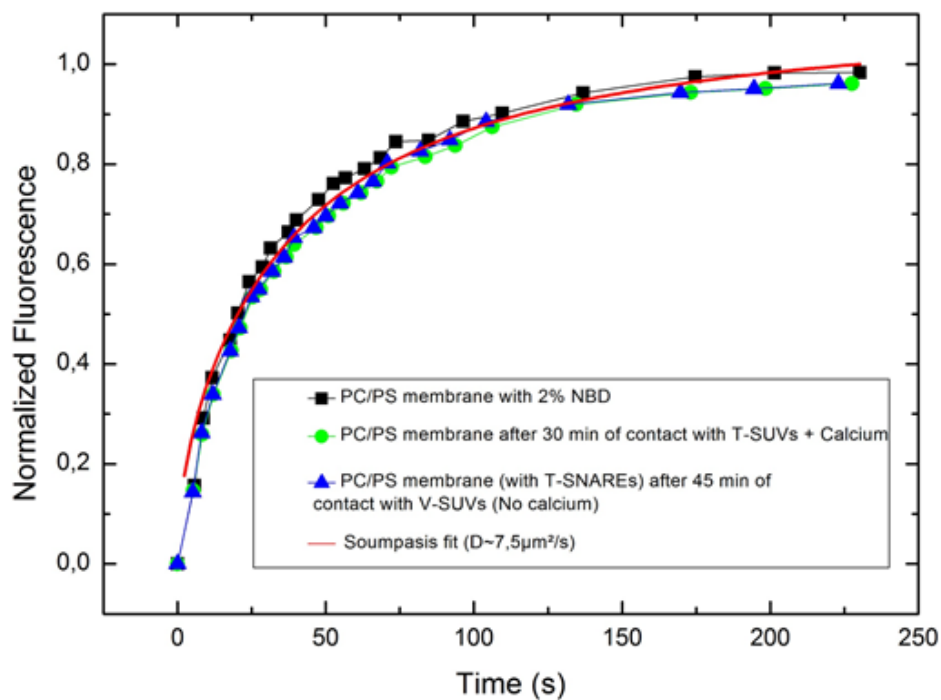
Figure 35 Experimental FRAP results. The black curve represents the fluorescent recovery of a PC/PS with 2% NBD fluorescent membrane. The green curve represents the fluorescent recovery of a lipid bilayer after allowing the fusion of T-SUVs via Ca2+. Blue curve, fluorescent recovery of a lipid membrane containing T-SNAREs after allowing V-SUVs to fuse (no Ca2+ in the buffer solution). The red curve represents the Soumpasis fit.

5.3 SNAREs Mediated Fusion between SUVs and Free Standing Lipid Bilayer

Once, t-SNAREs have been successfully incorporated in the free standing lipid bilayer (target lipid bilayer, from now on). We can explore fusion triggers by SNAREs proteins. In order to perform such a task, all the divalent ions Ca^{2+} responsible for the t-SNAREs insertion process must be completely removed from the microfluidic chip. During the experiments we exchanged 10 time the liquid volume of the microfluidic chip with a non- Ca^{2+} buffer (125mM KCl, 10mM HEPES). Due to the laminar flow in the system, the washing process was done without disturbing the created target lipid bilayer, guaranteeing a total extraction of the Ca^{2+}. After Ca^{2+} removal, a solution containing V-SUVs (50 nm) in buffer (125mM KCl, 10mM HEPES) was injected into the microfluidic chip. After 45 minutes of V-SUVs injection, we register fluorescent markers in the target lipid bilayer meaning that V-SUVs are indeed fusing to the target lipid bilayer. As no Ca^{2+} is presents in the buffer we may conclude that the coupling interaction between t-SNAREs in the target lipid bilayer and the v-SNAREs in the V-SUVs is the responsible mechanism to trigger fusion. A FRAP measurement was performed to determine if the fusion process was total or partial. Figure 35 (blue curve) shows the fluorescent recovery trace after photobleaching. It follows exactly the same behavior that in the cases of T-SUVs and the reference experiment. This means that the lipids presented in the V-SUVs membrane were incorporated into the target lipid bilayer and that this process was driven by SNARE proteins interaction.

5.4 Single Fusion Event Mediated by SNARE Proteins

After proving the completion of SUVs fusion by means of SNARE proteins. We address in the following the visualization and measurement of a single fusion event in a microfluidic chip. To do so, we diluted the V-SUV buffer concentration

to reduce the amount of SUVs in the solution. The procedure described in section 5.3 for V-SUV buffer injection in the chip was exactly repeated. Figure 36a, depicts a fluorescent V-SUV in close proximity of a target lipid bilayer (t-SNAREs are inserted). The fusion process was also monitor from the top side view, which allows a better inspection of the fusion process. In Figure 36b, a sequence of a single fusion event is observed. The V-SUV is freely moving on the target lipid bilayer until a t-SNARE/v-SNARE complex is formed, docking the vesicle to the bilayer. The single fusion event process concludes with the spreading of the V-SUVs lipid molecules along the circular area of the target lipid bilayer.
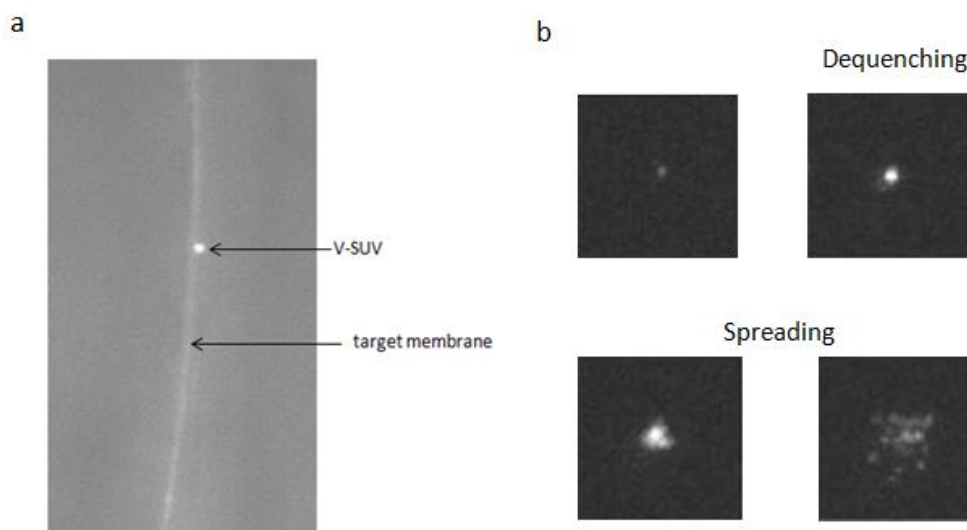
Figure 36 a) fluorescent side view image of a single V-SUV in close proximity to a target lipid membrane. b) Top view of a single fusion event, the fusion process can be divided in three steps V-SUV docking to the target membrane, dequenching of the fluorescent V-SUV, and finally the spreading of the vesicle lipids in the target membrane. *Images courtesy of Dr. Fleury.*

Changes in electrical capacitance of the target lipid bilayer were measured during a fusion event process, by using a combination of the patch clamp amplifier (EPC 10) and a software lock-in system (Patchmaster), providing a low noise capacitance recording down to the femtofarad levels (fF), which correspond to the change in membrane capacitance due to the fusion of a single SUV [111] (Appendix, A1). Figure 37, shows a trace of the total capacitance measurement

during T-SUVs to lipid bilayer fusion mediated by Ca^{2+}. Small jumps of the total capacitance are observed in the trace, which corresponds to a single vesicle fusion event. The capacitance step duration is about 300 ms and it represents the timeframe between the beginning of the pore opening and its end.
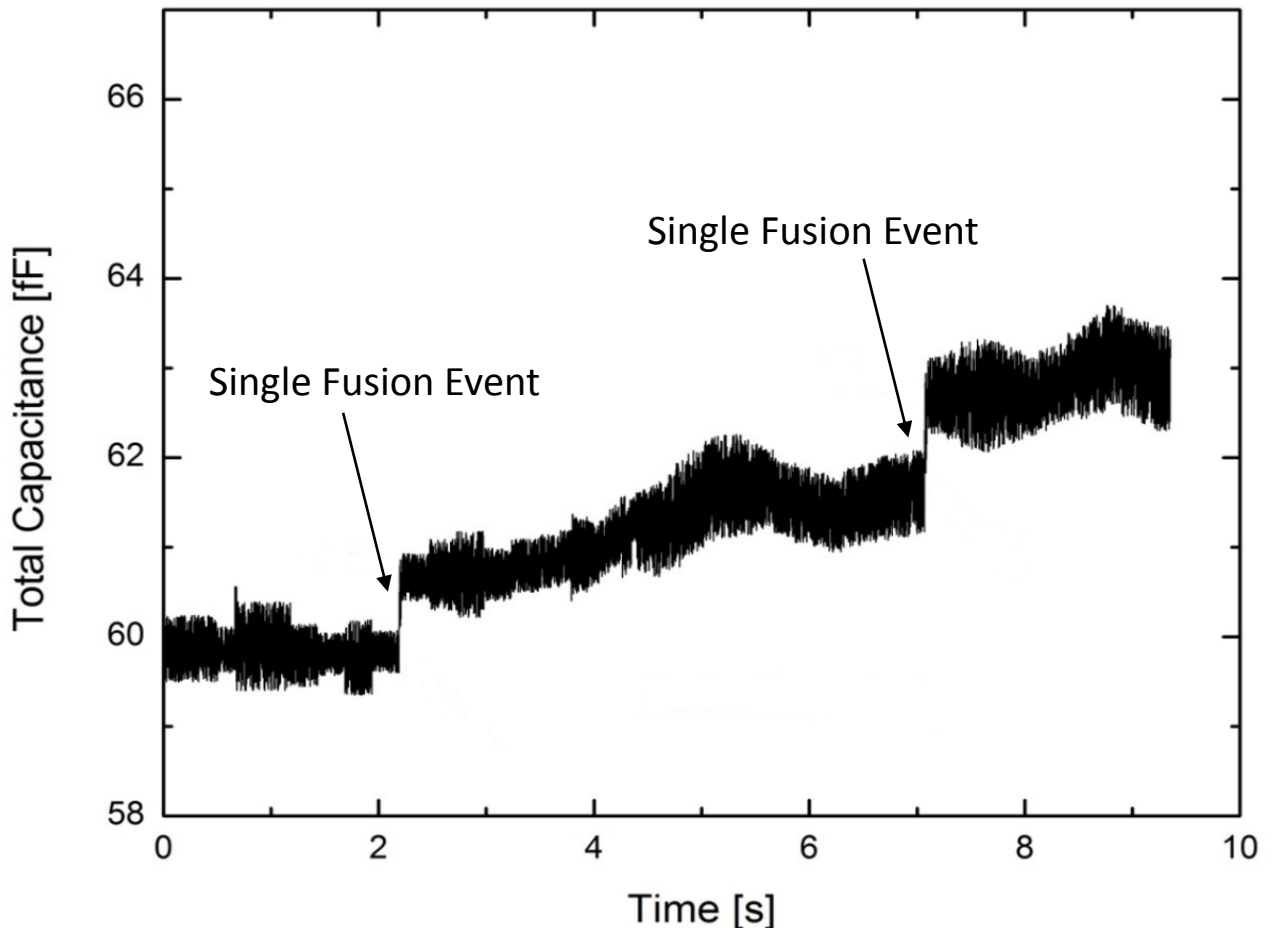
Figure 37 Capacitance trace of a free standing lipid membrane while a diluted solution of T-SUVs buffer + Ca2+ was allowed to fuse. A clear capacitance step can be observed in the trace, each of these steps correspond to the single fusion event of a vesicle. A data point was taken every ms.

The same procedure to measure lipid bilayer capacitance was applied for the case of SNARE mediated fusion events. A histogram was done with the different fusion times corresponding to both the Ca^{2+} mediated and the SNARE protein mediated fusion (figure 38). For SNARE protein mediated fusion, the resulting fusion step has an average of 75 ms. This is much faster that the 325 ms obtained

in the case of Ca²⁺ mediated fusion. Beside the fact that SNARE proteins decrease significantly the fusion time, this in vitro experiment is still far from the sub-millisecond fusion time obtained in real synaptic transmission. It is worth to notice that in real cells the fusion of synaptic vesicle is accomplished for a large protein complex composed of different proteins that cooperated together to achieve sub-millisecond fusion time.
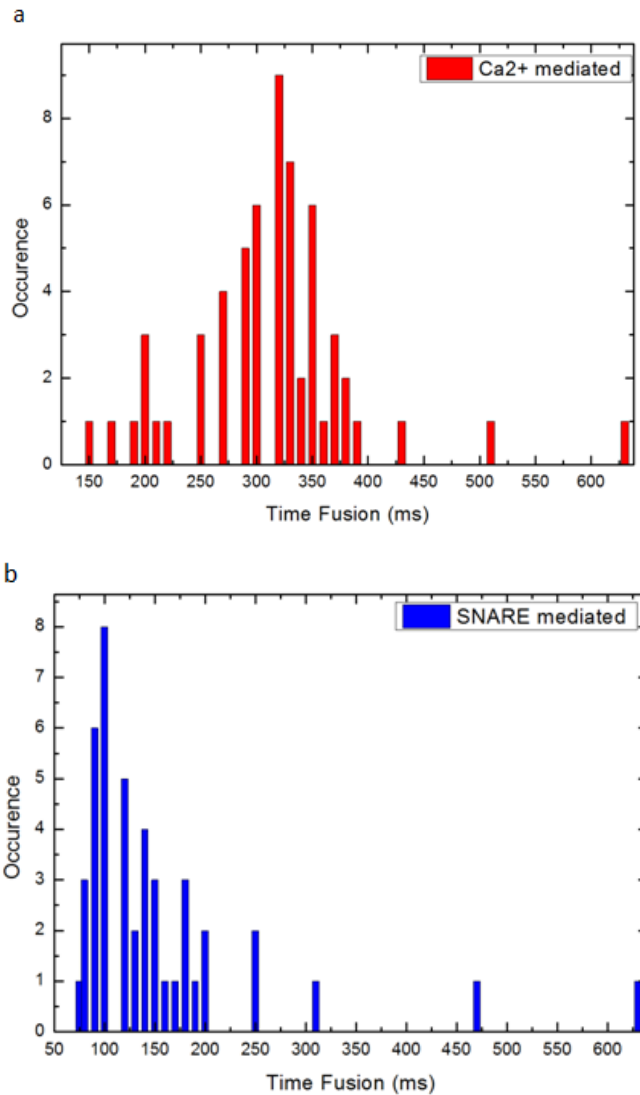
Figure 38 Statistic of the fusion event fusion time. a) depicts the histogram of the SUV fusion mediated by Ca2+ b) -SUVs to lipid membrane fusion times mediated by SNAREs.

6.   Adhesion Properties of Hydrophobin Bilayers

In this chapter, we address the production of hydrophobin protein bilayers in a microfluidic device. HFBI, an amphiphilic class II hydrophobin was selected as the test protein for the experiments. The ability of HFBI proteins to self assemble at oil/water and air/water interfaces is used to create HFBI bilayers in the developed chemes (chapter 3). Moreover, adhesion properties of the HFBI bilayers were characterized as a function of both the protein orientation and its charged amino acids distribution. For this purpose, three mutation variants and the wild type HFBI protein were used.

6.1   HFBI Protein Morphology

The crystallographic structure of HFBI hydrophobins shows two distinguishable regions; the hydrophobic patch which sequence is highly conserved in all class II members and a large hydrophilic region (figure 39a) [141]. The hydrophobic patch consists entirely of aliphatic side chains, comprising about half of all the aliphatic side chains of the hydrophobin molecule [142]. However, the hydrophilic region comprises the main part of the protein and it is characterized by six charged polar residues that are exposed on its surface (figure 39a) [24]. Four of these residues are located on top of the protein opposite to the hydrophobic patch (Asp40, Asp43, Arg45 and Lys50) (figure 39a). While the remaining two charged residues (Asp30 and Lys32) are located near the edge of the hydrophobic patch (figure 39a). Lienemman et, al. have produced three HFBI mutant types by replacing the charged residues with structurally related amino acids, neutrally charged [24]. HFBI$_{DK}$ represents the mutant variant in which both the positive charged residue lysine (K32) and the negative charged residue

aspartic acid (D30), are replaced for electrically neutral asparagine (N) and glutamine (Q), respectively. These two residues are located close to the hydrophobic patch of the protein molecule (figure 39b). In the case of HFBI$_{RK}$, only the two positive charged residues on top of the protein molecule arginine (R45) and lysine (K50) were substituted by glutamine (Q) (figure 39c). The last mutant variant HFBI$_{DDRK}$ comprises a total substitution of both the negative and positive charged residues located on top of the protein, while the side charged residues next to the hydrophobic patch remains unaltered (figure 39d).
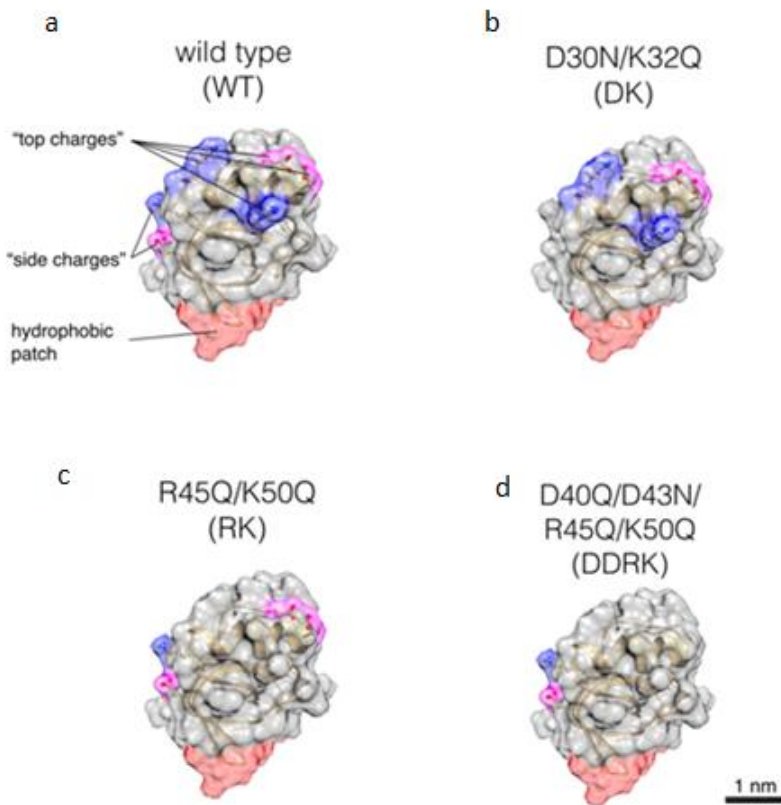
Figure 39 Three-dimensional structure of T. reesei hydrophobin HFBI. a) wild type HFBI, it possess a characteristic hydrophobic patch and a hydrophilic region with six charged polar residues. b) HFBIDK mutant variant in which both the positive charged lysine (K32) and the negative charged aspartic acid (D30), are replaced for electrically neutral asparagine (N) and glutamine (Q) respectively. c) HFBIRK, the two positive charged residues on top of the protein molecule arginine (R45) and lysine (K50) were substituted by glutamine (Q). d) HFBIDDRK comprises a total substitution of both the negative and positive charged residues located on top of the protein, while the side charged residues next to the hydrophobic patch remains unaltered.

6.2   HFBI Protein Solutions

HFBI proteins were dissolved in acetate buffer (pH 5, buffer concentration 10 mM) at a protein concentration of 100 µM and sonicated to dissolve protein aggregates. The acetate buffer contains a calculated ion concentration (ionic strength) of 6 mM. Solutions with higher ionic strength were prepared by adding NaCl to the acetate buffer. The ionic strengths of these buffers were adjusted to 100, 500, and 1000 mM.

6.3   Surface Tension of HFBI Proteins

Surface tensions γ of both the HFBI wild type and mutant protein monolayers at the oil/buffer and air/buffer interface were measured with the standard pendant drop method. For the oil/buffer case, droplets of protein buffer solution were created into the oil phase, the decrease in surface tension due to the adsorption of proteins at the interface was recorded over time until a plateau was reached (figure 40). For the air/buffer case, droplets of protein solution were created in air. Buffer droplets undergo a decrease in volume due to water evaporation during the protein adsorption process. When a complete surface film is formed, further evaporation leads to wrinkling of the droplets surface (figure 41). This wrinkling like effect causes a mismatch of the droplet shape calculation by the software, producing a large error in the surface tension values. However, to overcome this problem and to mimic the situation in the microfluidic channels, the surface tension evolution was recorded until the first wrinkles appeared. Then, the drop was slightly inflated again until it recovered its original shape, thus surface tension values were successfully measured indicating a complete and stable surface film. A detailed resume of all the surface tension values for the different liquid system used in the present work is given in table 7.
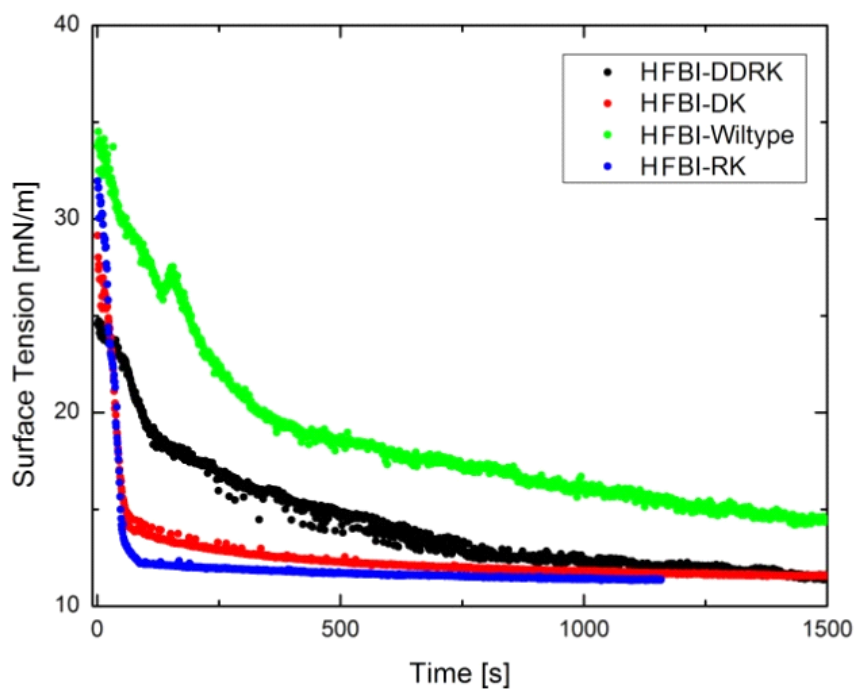
Figure 40 Surface tension trace for all the hydrophobins members; wild type HFBI, HFBIDK, HFBIRK, HFBIDDRK. The pendant droplet technique was used in all cases. The ambient phase for all members was hexadecane.
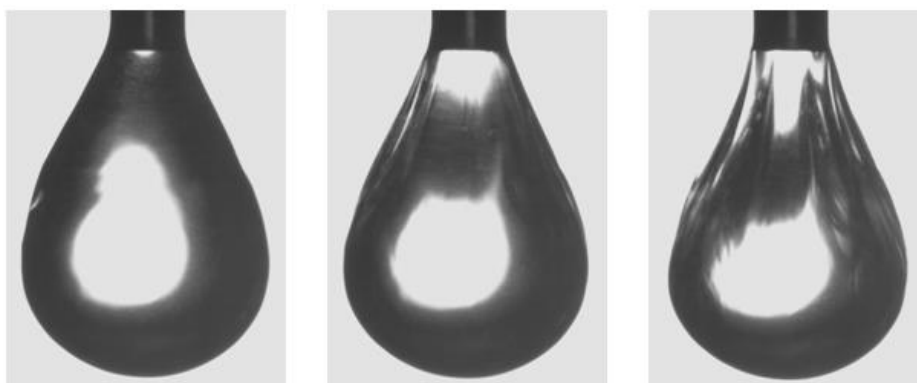
Figure 41 Wrinkle like effect observed during the surface tension measurement HFBI buffer droplets in air. For successfully measuring γ, the buffer droplet was force to recover its original shape by injecting additional buffer via the test needle.

	Surface Tension Values (mN/m)			
System	**HFBI_{Wild-type}**	**HFBI_{DK}**	**HFBI_{RK}**	**HFBI_{DDRK}**
hexadecane/ HFBI-buffer	13.9 ± 1.5	11.5 ± 1.1	11.4 ± 1.4	11 ± 1
FC-70/ HFBI-buffer	29 ± 1.2	28 ± 0.9	28 ± 1.2	31 ± 1.5
HFBI-buffer/air	17.1 ± 0.4	-------	-------	-------
HFBI-buffer/air	16.2 ± 0.6	-------	-------	-------
Surface Tension Values at Different Ionic Strengths				
100 (mM)	14.2 ± 1.8 mN/m	-------	-------	-------
500 (mM)	17.5 ± 2.3 mN/m	-------	-------	-------
1000 (mM)	20.3 ± 1.8 mN/m	-------	-------	-------

Table 7 Experimental surface tension values for all the different system used. The values on top correspond to the plateau values of figure 40. The bottom values correspond to a hexadecane/buffer system with increased ionic strength.

6.4   Production of HFBI Bilayers with Controllable Protein Orientation

First, free standing HFBI Bilayers, in which the hydrophilic regions and therefore the side charges of the proteins interact to form the core of a bilayer were fabricated using a UV glue microfluidic devices and an oil/buffer system as the one described in figure 42a-b. From now on we will call such a bilayer a *hydrophilic core HFBI bilayer.* It is important to note that, due to its wetting properties; a UV glue device provides hydrophilic microchannel walls which enables the formation of such a bilayer. To form a *hydrophilic core HFBI bilayer*, we used a buffer at a concentration of 20 µM. This values is well above the surface saturation concentration (SSC), which describes the behavior of hydrophobins in an analogy to the critical micelle concentration (CMC) used for normal surfactants [143].

Second, HFBI Bilayers, in which the hydrophobic patches of the proteins interact to form a bilayer (*hydrophobic core HFBI bilayer*), were produced using a PDMS microfluidic device and an oil/buffer system described in figure 42c-d. For a *hydrophobic core HFBI bilayer*, the buffer concentration was (5-10) µM HFBI proteins, well above the SSC. The decrease in protein concentration is due to the high affinity these proteins possess to PDMS walls, which results in protein aggregation on the wall affecting the bilayer formation process. No protein agglomeration was observed using a buffer concentration of (5-10) µM. The HFBI bilayer formation process follows the same protocol explained for the case of free standing lipid bilayers (chapter 3). In the case of a hydrophobic-HFBI bilayer, the experiment was supplemented with a patch clamp amplifier.
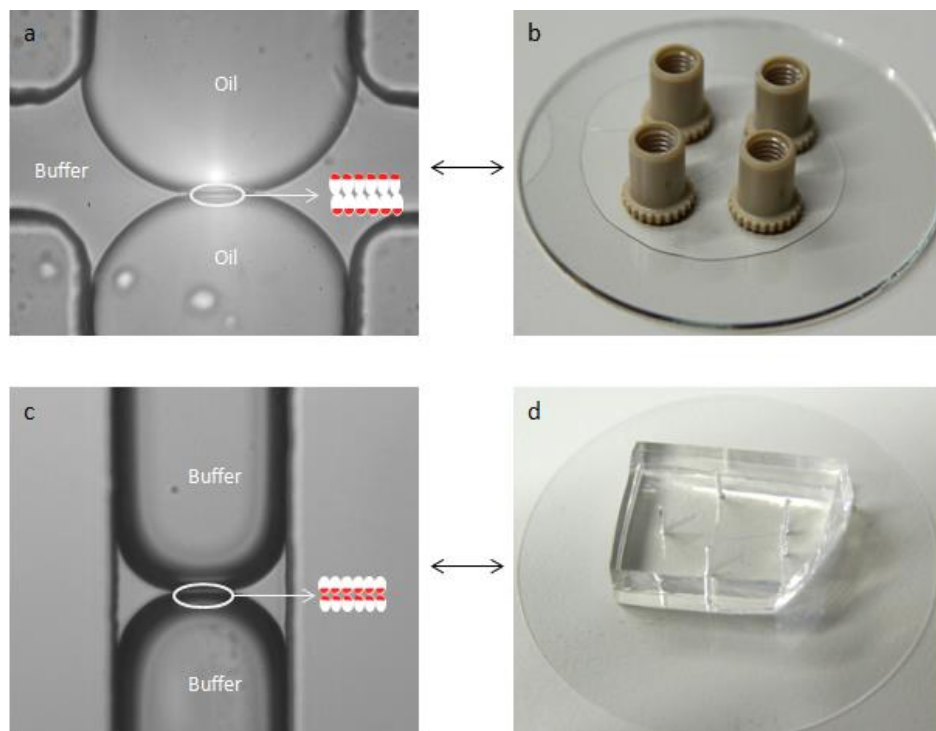
Figure 42 a) *hydrophilic core HFBI bilayer*, in which the hydrophilic regions and therefore the side charges of the proteins interact to form a bilayer. Two oil droplets were inserted into the vertical channel of a cross geometry, while the horizontal channel was perfused with a HFBI-buffer solution. b) UV glue microfluidic device. c) *hydrophobic core HFBI bilayer*, created by the interaction of the hydrophobic patches of the proteins. Two HFBI-buffer droplets were inserted into the vertical channel of a cross geometry, while the horizontal channel was perfused with oil. d) PDMS microfluidic device.

6.5   HFBI Bilayers Thickness

Before the characterization of HFBI protein interactions, within and across a free standing bilayer. We have to exclude protein multilayers formation and the present of an oil film in-between the protein bilayers. Therefore, capacitance traces were measured during the formation process of *hydrophobic core HFBI bilayer* (in a hexadecane/HFBI buffer system) (Figure 43). During the HFBI bilayer formation, a rapid increase in capacitance is observed, which stabilizes at 11.3 pF. The specific capacitance for the bilayer corresponds to 7.87 $\mu F/cm^2$ ± 0.2 $\mu F/cm^2$ (Inset, figure 43). The thickness of the *hydrophobic core HFBI bilayer* can be determined by applying equation 4 (chapter 1). However, the dielectric constant for HFBI proteins is unknown. The thickness of the layer can only be estimated by employing some assumptions: first, only the hydrophobic patch forms the capacitive insulating layer. Thus, with regard to the HFBI crystal structure, a layer thickness of approximately 3 nm is expected (whereas the full protein bilayer should have a thickness of ca. 6 nm). Second, as the amino acids at the hydrophobic patch are all aliphatic [142], we can assume a dielectric constant similar to pure hydrocarbons, i. e. ≈ 2.2 [144]. Computing the previous dielectric constant value with the specific capacitance measurement, results in a film thickness of 2.5 nm in the case of the hexadecane/HFBI buffer system. In addition, researches also report protein dielectric constants from 2 up to 5 for proteins similar to HFBI [145]. Using the given literature values for the protein dielectric constant, a maximum film thickness of 6.0 nm is determined. This gives rise to an uncertainty range for the thickness of the *hydrophobic core HFBI bilayer*, yet a multilayer formation can safely be excluded.

To exclude the present of an oil film in-between the bilayer, a complementary capacitance measurement for a *hydrophobic core HFBI bilayer*, in which the oil (hexadecane) phase was replaced by air was determined. The specific capacitance for the bilayer corresponds to 7.0 $\mu F/cm^2$ ± 0.9 $\mu F/cm^2$ (air/HFBI-buffer) (Inset, figure 43). Comparing the specific capacitance values obtained for the bilayers in both systems; hexadecane/HFBI-buffer and air/HFBI-buffer, respectively (Inset, figure 43). It should be safe to exclude any residual oil layer, considering the fact

that an increase in thickness always means a reduction of the capacitance. Therefore, an additional oil film between the HFBI bilayer would reduce the specific capacitance, yet a slightly higher value is observed (Inset, figure 43).
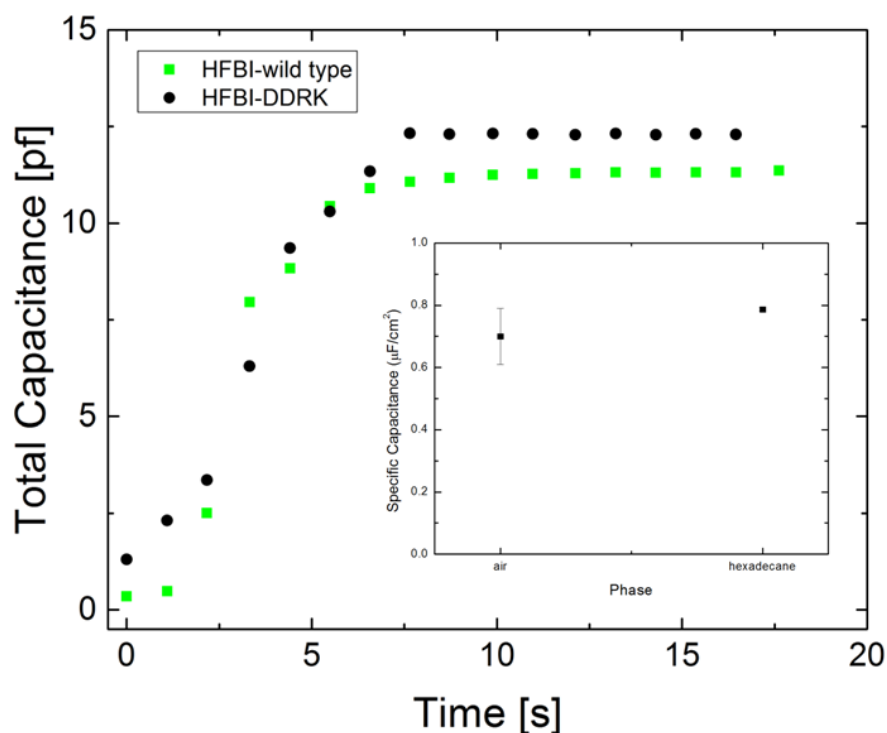
Figure 43 Total capacitance trace of a *hydrophobic core HFBI bilayer* formation process. A Hexadecane/HFBI-buffer system was used. The total capacitance was measured for both the HFBI$_{wild type}$ and the HFBI$_{DDRK}$. Inset: Specific capacitance values determined for a HFBI bilayer in both air/HFBI-buffer and Hexadecane/HFBI-buffer systems. Only HFBI$_{wild type}$ was used to compare both systems.

6.6   Adhesion Energy and Bilayer Tension of HFBI Bilayers

Adhesion energy (ΔW) values were obtained for HFBI bilayers containing wild type proteins and the three mutants described in 6.1. The Young-Dupré relation $\Delta W = 2\gamma \left[1 - \cos(\theta)\right]$, was used to calculated the corresponding adhesive energy between the HFBI monolayers. The bilayer contact angles were measured by optical inspection of the recorded video frames. While the surface tension values correspond to those in table 7. Figure 44, shows the results of the adhesion energy for the oil/HFBI buffer system. Surprisingly, the interaction energy between the hydrophobic patches of the proteins (*hydrophobic core HFBI bilayer*) is

much smaller than between the hydrophilic sides (*hydrophilic core HFBI bilayer*). This observation is independent from the chosen oil (Hexadecane or FC-70). Moreover, assuming that the area occupied by one protein is 3.2 nm² [19], with the absolute value of the interaction energy of a 1 mJ/m² for the hydrophobic patches (figure 44), the interaction energy per molecule pair can be estimated as ca. 0.9 k_BT. This is surprisingly small and about two orders of magnitude lower than the adsorption energy of an HFBI molecule to the alcane/water interface [146].
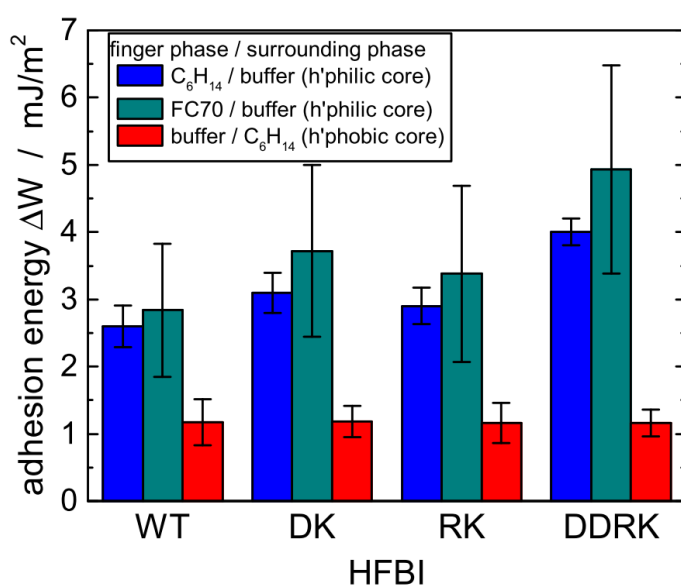
Figure 44 Adhesion energy values obtained for each HFBI protein member. Blue bars correspond to a *hydrophilic core HFBI bilayer* (hexadecane/buffer). Green bars, correspond to a *hydrophilic core HFBI bilayer* (FC-70/buffer). Red bars, correspond to a *hydrophobic core HFBI bilayer* (buffer/hexadecane).

HFBI bilayers tension values were calculated applying equation 7 (chapter 1). The values for the different oil/HFBI-buffer systems are depicted in figure 45. The highest value for the bilayer tension of a 55 mN/m was measured for FC70 (green bar, figure 45). Compared to the lysis tension for lipid vesicles, which typically ranges around 10 mN/m [147], the bilayer tension values obtained in the experiments are impressively large. That the HFBI bilayer can sustain these tensions without immediate rupture reflects the very high cohesion the hydrophobin molecules have in such a bilayer. The comparison of the different

tension values shows moreover that the bilayer tension follows the trends given by the surface tensions of the individual interfaces, whereas the bilayer orientation has little influence.
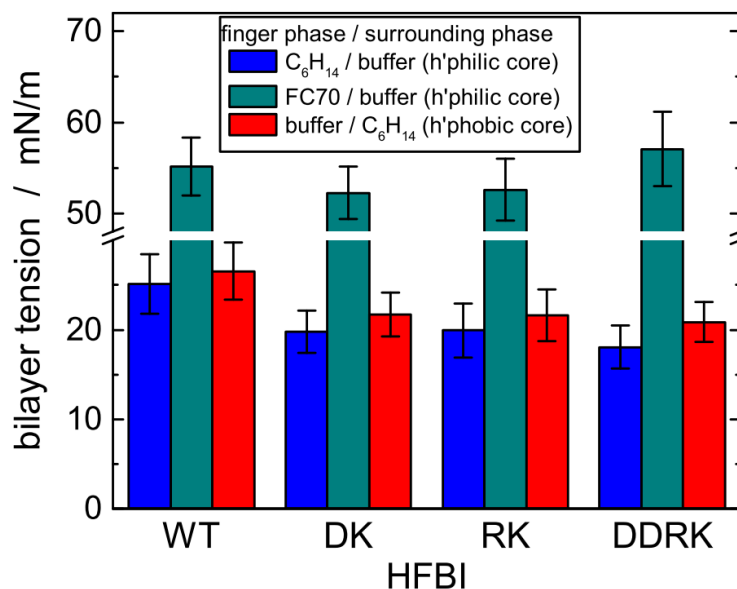
Figure 45 Bilayer tension values obtained for each HFBI protein member. Blue bars correspond to a *hydrophilic core HFBI bilayer* (hexadecane/buffer). Green bars, correspond to a *hydrophilic core HFBI bilayer* (FC-70/buffer). Red bars, correspond to a *hydrophobic core HFBI bilayer* (buffer/hexadecane).

Bilayer tension values varied slightly with respect to the different mutants used during the experiments (figure 45). All mutant HFBI bilayers present a lower tension than the wild type, with the exception of HFBI$_{DDRK}$ at the FC70/HFBI-buffer interface. These results follow once again the trend in surface tension for the different systems. For the adhesion energy ΔW, no significant differences for the *hydrophobic core HFBI bilayers* of the mutants compared to the wild type is observed (figure 44, red bars). This result can be understood, considering that the hydrophobic patch is preserved for all HFBI members. It shows, that the interaction energy is mainly determined by short-ranged interactions while the presence or the absence of charges at the outside of the bilayer, hardly affect adhesion energy. However, for *hydrophilic core HFBI bilayers*, the charge distribution on the hydrophilic region of HFBI proteins, highly influence the

adhesion energy. The HFBI$_{wild-type}$ presents the lowest adhesion energy, while the HFBI$_{DDRK}$ presents the highest. This indicates that a reduction of the absolute number of charged amino acids on the protein (WT: 6, DK and RK: 4, DDRK: 2) leads to a higher adhesion energy, whereas the net charge (-2 for RK, 0 for all others) seems to have little influence.

In order to prove the influence of the charges distribution on the adhesion energy. HFBI protein charges were screened using a higher concentration of ions in the buffer phase (100, 500, 1000 mM). These ion concentrations correspond, according to the Debye-Hückel theory, to Debye screening lengths of 1.0, 0.4, and 0.3 nm, respectively. It was observed that a higher ionic strength of the buffer leads to an increase in both the bilayer adhesion energy. For the highest ion concentration used (1000 mM), the energy is roughly doubled compared to the lowest salt case (6 mM). The same behavior holds for the bilayer tension (figure 46). These results corroborate the findings using mutated HFBI protein.
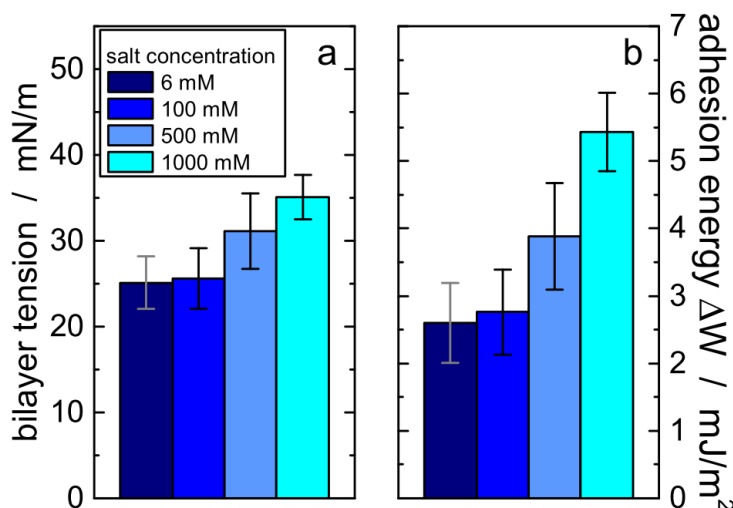
Figure 46 a) Bilayer tension, b) adhesion energy values. All the values were calculated for a *hydrophilic core HFBI bilayer* (hexadecane/buffer).

6.7   Week Nature of the HFBI Protein Interaction Energy

The obtained values for the adhesion energy of the HFBI protein-protein interaction are on the order of few k_BTs. Therefore, it would be expected that thermal fluctuations have an influence on the adhesion. To be able to observe this influence, we performed an experiment in which oil droplets covered with a HFBI monolayer interact with a HFBI layer on the bottom of a PDMS microchannel (figure 47a). First, we introduce a HFBI-buffer solution in a PDMS microfluidic channel, prefilled with FC-70. After 20 minutes, the oil between channel wall and the HFBI buffer interface is drained into the PDMS. This led to the adsorption of HFBI proteins at the PDMS bottom of the microchannel. Second, small monodisperse FC-70 droplets (1 – 5) µm were introduced in the buffer phase. Due to the densities of the FC-70 and the buffer, the oil droplets sink to the bottom of the channel (figure 47a). The HFBI monolayer surrounding the oil droplets interact with the HFBI proteins absorbed at the PDMS bottom of the channel. Third, the motion of the droplets at the bottom of the microfluidic channel was monitored. This motion could be approximated as a 2D Brownian motion. Interestingly, the obtained motion analysis at room temperature shows a clear subdiffusive behavior $<\Delta X^2> \propto t^\alpha$ $\alpha = 0.5$ (figure 47b). This subdiffuse behavior may be attributed to the weak adhesive interaction energy of the HFBI proteins, present in both the oil droplet and the PDMS bottom. To test this hypothesis, the experiment was repeated at a higher temperature (50 ˚C). The droplet motion analysis for this experiment results tend to a rather normal diffusion behavior of the oil droplets ($\alpha = 0.8$). Therefore, it can be concluded that the pair interaction energy between HBFI proteins should be in the order of few k_BT, in agreement with our previous measurements.
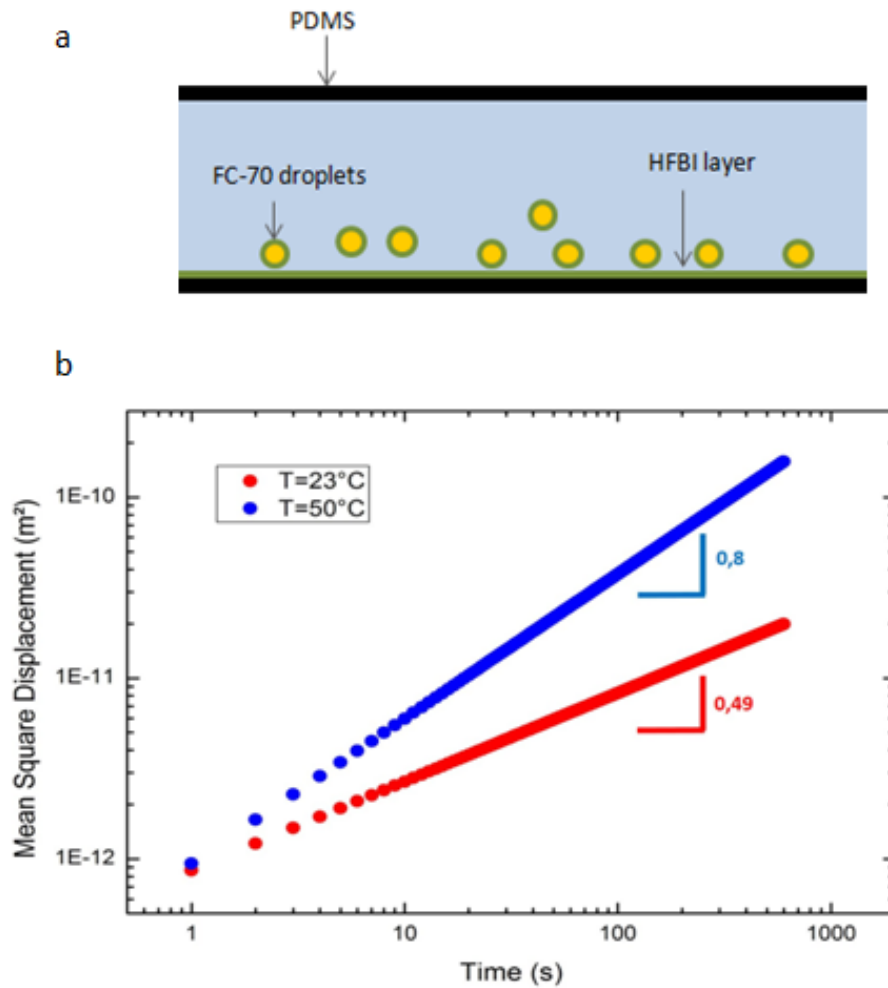
Figure 47 a) Experimental sketch of FC-70 droplets cover with a HFBI monolayer. Due to gravity droplets sink interacting with a HFBI layer on the bottom of a PDMS microchannel. b) mean square displacement of HFBIWT covered FC-70 droplets in contact with a HFBI protein covered PDMS wall. The slope of the curves indicates a subdiffusive behavior of the FC-70 droplets (red trace). An Increase in the temperature (50 ˚C), lead to a rather diffusive behavior of the FC-70 droplets (blue trace).

SUMMARY

A novel microfluidic scheme with simultaneous optical and patch clamping access for measurements, was presented to study artificial lipid bilayer fusion events and its intermediated states. The microfluidic scheme allows the manipulation of two independent lipid bilayers, which can be brought into contact and thus to study the dynamic of a hemifused state formation process. The formation of bilayers and hemifusion diaphragms is shown for four different lipids. Furthermore, capacitance measurements via patch clamping technique proofed the production of solvent free lipid bilayers and hemifusion diaphragms. In addition, Simultaneous optical inspection revealed a fast formation process of a hemifusion diaphragm which is five orders of magnitude faster than previously observed for supported lipid bilayers and two orders of magnitude faster than previously observed for unilamellar vesicles. The formation process of a hemifusion diaphragm could be divided into a very fast initial symmetry breaking process where an initial hemifusion diaphragm of about (20–60) mm is formed followed by growth of the hemifusion diaphragm which could be described by a dewetting process under no-slip boundary conditions. The corresponding hemifusion state formed by this process is equivalent to a dead end or equilibrium state and no spontaneous fusion could be observed. Furthermore, the formation of reversible nanopores in a monoolein hemifusion diaphragm was observed by electrofusion, while the breaking voltage for a monoolein hemifusion diaphragm turned out to be lower than for a single free standing monoolein bilayer.

The microfluidic scheme was also used to inspect single fusion events mediated by SNARE proteins between a lipid bilayer and small unillaminar vesicles (SUVs). t-SNAREs were successfully transferred from T-SUVs to a the lipid bilayer, by the action of divalent cations (Ca^{2+}) present in the buffer phase, cations mediate the fusion of T-SUVs to the lipid bilayer. After removal of Ca^{2+}

and T-SUVs, Fluorescent SUVs containing v-SNAREs (V-SUVs), were brought in contact with the lipid bilayer functionalized with t-SNAREs. The Fluorescent inspection of the lipid bilayer proofed the fusion of the V-SUVs to the bilayer, via the formation of a t-SNARE/ v-SNARE complex. Furthermore, FRAP experiments proofed the mobility of the fluorescent lipid transferred to the artificial lipid bilayer, discarding any partial fusion event. In addition, single fusion events were inspected via fluorescent microscopy and capacitance measurements (patch clamping). The fusion times for both, a single Ca^{2+} mediated fusion and a single SNARE mediated fusion event were successfully extracted from the capacitance traces. From the obtained results, it is evident that SNARE protein complex formation trigger fusion between bilayer faster than Ca^{2+}.

The microfluidic scheme was extended to produce free standing HFBI bilayer. The protein bilayers were produced with a controlled orientation of the HFBI proteins into the bilayer core, by tuning the wetting characteristic of the microchannel walls. Capacitance measurement results excluded the possibility of protein multilayer formation, while the comparison of the specific capacitance of HFBI bilayers formed in both oil/HFBI-buffer and air/HFBI-buffer systems, demonstrated the existence of solvent free HFBI bilayers. Furthermore, the wild type HFBI protein and three mutants were used to study the effect of the charged amino acids of the protein on the adhesive properties. The obtained results revealed that a reduction of the absolute number of charged amino acids on the protein surface, leads to an increase of the adhesion energy between HFBI monolayer.

APPENDIX

A.1

Guide to low noise on-cell capacitance measurements using the EPC 10

In this step-by-step protocol we describe how to practically obtain low-noise on-cell capacitance measurements using an EPC 10 and PATCHMASTER software.

General

Hardware Set-up:

For optimal noise performance an EPC 10 with increased bandwidth in high gain range should be used (ECP 10 with revision of at least I or K). For recording of high resolution sweeps of several seconds make sure that your PC has enough RAM (1 GB, 2 GB recommended). Recalibrate the EPC 10 with PATCHMASTER software.

Software Set-up:

Along with this guide we provide a set of default files for OnCell capacitance measurements.

Using the default OnCell_Cm example

The default configuration is adapted to PATCHMASTER version 2.15 (available for the HEKA web site: http://www.heka.com/download.html) and requires a PATCHMASTER installation of this version in the path C:\HEKA\Patchmaster. Furthermore the configuration is adapted for an EPC 10 Single patch clamp amplifier and a computer monitor resolution of 1024 x 768. Memory requirements have been adapted to a Pentium IV with 512 MB RAM running under Windows XP. Please copy the folder "OnCell_Cm" and the configuration file "OnCell_Cm.set" in your PATCHMASTER folder.

NOTE: In order to start your PATCHMASTER software with the provided configuration, drag the configuration file "OnCell_Cm.set" over the PATCHMASTER application.

If you are not using the "OnCell_Cm.set" file, please perform the most important settings in the configuration manually:

Turn on LockIn configuration and set the
- LockIn Mode: On Cell
- Calibration Mode: Manual
- Phase Shift: 0
- Attenuation: 1.0-Write to Notebook: should be off during routine measurements. Turn it on for inspection.
- Default Y Ranges: CM: 10 fF; GM: 1.0 nS

In the Configuration Window on pane General increase "Max. Sample Points" to the maximum allowed by the RAM in your computer. (If you exceed the RAM the following message appears: "There seems to be insufficient memory for the present Configuration settings...." Press "Undo Changes" and try to increase the "Max. Sample Points" by a smaller amount.

In the Macros menu turn off "Protocol to Notebook".
Load the following files:
- OnCell_Cm.pgf (Pulse Generator File)
- OnCell_Cm.pro (Protocol Editor File)
- OnCell_Cm.onl (Online Analysis File)

Description of the content of the OnCell_Cm files
In our configuration we use the following convention: AD channel 1 is the MUX channel (output of the active amplifier after Filter 1 prior to Filter 2), AD-channel 2 is the capacitance trace (named "LockIn_CM") and AD-channel 3 is the

conductance trace (named "LockIn_GM"). It is important to keep this order of channels for the protocols and the online analysis to work correctly.

The Pulse Generator File: OnCell_Cm.pgf

It contains the sequences SineTest and Rec20kHz.

SineTest:

Used for calibration of the LockIn.

Rec20kHz:

Used for the recording of capacitance changes.

In general the same as SineTest but with longer duration a smaller sine wave amplitude and (if required) more input and output channels. Please make sure that your recording sequence and your calibration sequence "SineTest" are identical with respect to the following critical parameters of the pulse generator:

- Sampling Frequency
- Sine Wave Frequency
- Points per Sine Wave Cycle
- Current Recording Channel (AD)

The Protocol File: OnCell_Cm.pro

It contains 6 default protocols. For calibration of the Locking we usetheprotocols

"ScanPhase", "AdjustPhase", and "GetAttenuation".

ScanPhase:

Varies the LockIn Phase setting and measures the change in Gm and Cm. Is used to quickly find the correct range of the phase setting.

AdjustPhase:

The LockIn Phase can be manually adjusted and the change in Gm is displayed. Is used to fine tune the LockIn Phase setting.

GetAttenuation:

Changes the C-Fast compensation of the amplifier and measures the CM with the LockIn at a given phase setting. Is used to calibrate the amplitude of the LockIn (Attenuation) via linear regression of the plot measured CM versus decompensated C-Fast.

Adjust_Osci:

Is a tool that helps setting the oscilloscope scaling offsets appropriately.

Conf_1:

Is a protocol that sets a custom configuration of the amplifier. Should be used to maintain the critical parameters of the amplifier unchanged between measurements. The critical parameters of the amplifier that might change the LockIn calibration are:

-   Recording Mode

-   Gain

-   Filter 1

    Filter 2 (if the current is measured on the Imon-2 channel)

-   Stim Filter

LinReg:

Performs a linear regression. Called from protocol "GetAttenuation".

The Online Analysis File: OnCell_Cm.onl

Four default analysis methods are provided. The methods "ScanPhase", AdjustPhase" and "GetAttn" are used to analyse and display the results during the calibration procedure of the LockIn. The fourth method "MeasureCm" is used to measure the mean values of Cm and Gm and the standard deviation of Cm at the beginning (cursor position 2-15%) of the trace.

The LockIn Calibration Procedure

Phase Calibration:

It is not obligatory to perform calibration only after the on-cell recording configuration has been established. Identical results are obtained with calibrations prior to patching, with the pipette above the solution or with a closed pipette in the solution. If you perform the calibration in the actual recording configuration, the seal has to be stable to allow for a correct and fast calibration. In any case it is crucial, that the amplifier settings and Pulse Generator settings are identical for calibration and recording (see above, "The Pulse Generator File" and "protocol Conf_1").

To get an overview on the phase setting, start protocol "ScanPhase". From a starting phase of

150° the phase is increased in 5° steps. At every phase two LockIn measurements are made, toggling the C-fast compensation by 50 fF inbetween. The resulting DeltaCm values are displayed in the upper graph and the DeltaGm values in the lower graph. The correct phase is reached if DeltaCm goes through its maximum and DeltaGm through its minimum. When the measurement passed the correct phase setting, terminate the protocol with the F12 key. The phase at minimum of DeltaGM is then automatically entered as LockIn Phase in the LockIn configuration. Fine tune the LockIn Phase with the protocol "AdjustPhase". Start the protocol. As starting phase angle the last entry in the LockIn configuration is prompted. Press OK. The DeltaGM values are displayed in two graphs. The upper graph provides an overview and the lower graph displays the DeltaGM value at higher resolution. The second graph is wiped every 20 measurements. Use the keys "1" and "2" to increment and decrement the phase by 10°, respectively. Use the keys "3" and "4" to increment and decrement the phase by 0.5°, respectively. Again, the optimal phase is found, when the DeltaGM has reached a minimum. Terminate the phase adjustment by pressing the "F12" key. You might find that the first measurement gives an outlying result that leads to a disadvantageous scaling of the graph. In such a case stop the protocol by pressing "F12" and restart it.

Amplitude Calibration:

At the given phase angle we now calibrate the amplitude of our Cm measurements. As calibration reference we use the C-Fast compensation of the EPC 10. Start the protocol "GetAttenuation". Starting from its auto compensation value the C-fast compensation will be reduced by 10 fF at a time. Then the Cm is measured with the LockIn and plotted against the difference in C-Fast compensation. This cycle is repeated 5 times and the slope is calculated by linear regression. The slope is the scaling factor for the amplitude (ratio of measured / expected capacitance change) and is set as "Attenuation" in the LockIn configuration.

NOTE: In case of a negative slope, please reduce the LockIn phase angle by 180° (LockIn configuration) and repeat the amplitude calibration.

Typical Phase and Attenuation Settings

The listed values were measured with a 1.5 pF capacitor connected to the headstage of an EPC 10 revision J. The capacitance measured with the C-fast compensation was: 2.37 pF (1.5 pF + 0.87 pF input capacitance of EPC 10, Tau = 91.5 nsec).

	Rec. Mode: OnCell, Gain: 50 mV/pA, Filter 1: 30 kHz Bessel, Current			
	Stim Filter: 2 µs		*Stim Filter: 20 µs*	
Sine Freq.	**Phase**	**Attenuation**	**Phase**	**Attenuation**
20 kHz	266.0 °	0.944	164.5 °	0.356
25 kHz	241.5 °	0.855	129.0 °	0.240
40 kHz	174.0 °	0.597	40.5 °	0.078

Practical guide

Open "OnCell_Cm.pgf" and define the amplitude and frequency of your sine wave in the "Sine Wave Settings" dialogue of the sequences "Rec20kHz",

and "SineTest" (we recommend 25 kHz for on-cell measurements of exo- and endocytic capacitance changes; 40 kHz, if the fusion pore is the main object of the study). Choose the maximally possible number of points per cycle (i.e. 8 for 25 kHz). For the optimal stimulus frequency for on-cell measurements of non-linear capacitance (charge movement in channels and transporters please refer to the original literature (Fernandez, 1982; Gale, 1997; Oliver, 1999). Minimise electromagnetic pick-up of the setup (grounding and shielding) and optimise setup for short, thick-walled borosilicate or quartz pipettes, used at a steep angle (low immersion depth). Pull sturdy pipettes, coat with sylgard (2-5 times) up to 50-75 μm from the tip (closer it would affect sealing).

Calibration

In your desired configuration (closed pipette, pipette above bath, on-cell configuration) adjust the amplifier settings (you might use the protocol *conf_1* to set all the crucial parameters). Perform the *Phase Calibration* and *Amplitude Calibration* described above.

Measurement

Obtain a high resistance (>10 GOhm) on-cell configuration with very little suction. Choose the recording settings (amplifier and pgf). If you wish, you could now confirm or fine-tune the phase setting, calibrate attenuation. Finally acquire a data sweep.

Post-recording correction of the phase settings

If channel flickers occur at a sufficient rate, use them for recalculation from current. Else you might want to apply slight suction manually or with a triggered air pump to elicit small suction pulses. Those result in an increase of patch capacitance.

Use lock-in configuration dialogue of Patchmaster for recalculation of apparent capacitance and conductance with a different phase until conductance changes are

not any longer reflected in the capacitance trace (channel flicker) or the suction-evoked capacitance changes are not reflected in the conductance trace.

Alternatively use the IGOR calculation macro for Re, Im/ω, G_p and C_V

A.2

A fluorescence recovery after photobleaching (FRAP) test to inspect the mobility of the fluorescent lipid incorporation into the lipid membrane (figure A2). The experiment was done as follows:

1. A lipid membrane was created with a T-SUV/buffer as described before, the membrane was image from top, and thus we have a circular view of the lipid membrane. The T-SUVs were allowed to interact with the membrane over a period of 30 minutes prior the photobleaching to ensure that most of the T-SUVs fused.
2. Photobleaching was performed on the fluorescent circular lipid membrane.
3. After Photobleaching the fluorescent recovery was measured. As the lipid membrane has a 2D circular shape, the recovery should follow the Soumpasis fit.
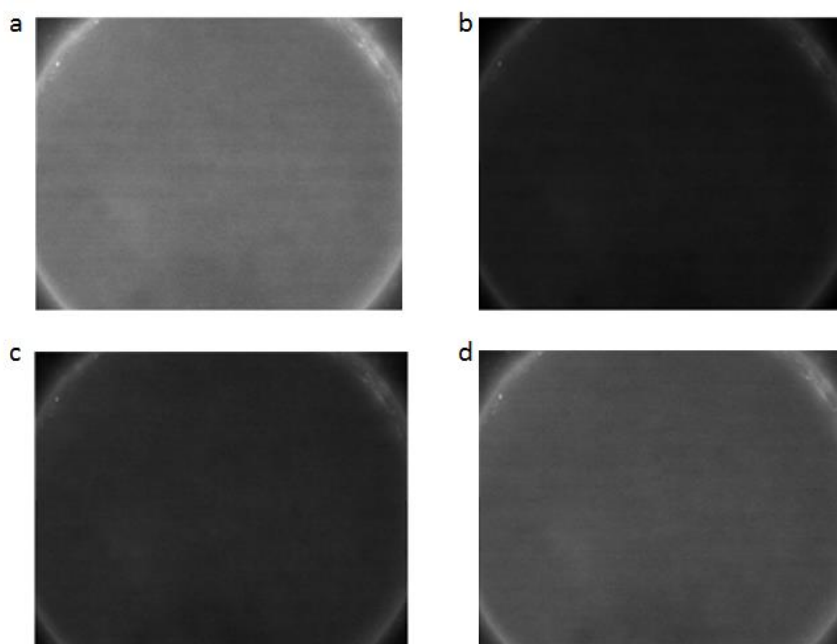
Figure A2 a) free standing lipid membrane image from top for FRAP test. T-SUVs were allowed to interact with the membrane over 30 minutes to ensure sufficient fusion events. b) Photobleaching of the lipid membrane. c-d) fluorescent recovery after Photobleaching. *Experiment done by Dr. Fleury.*

Bibliography

[1]   D. Balleza, "Toward Understanding Protocell Mechanosensation," *Orig. Life Evol. Biosph.*, vol. 41, no. 3, pp. 281–304, 2011.

[2]   R. V. Solé, "Evolution and self-assembly of protocells" *Int. J. Biochem. Cell Biol.*, vol. 41, no. 2, pp. 274–284, 2009.

[3]   T. Carletti and D. Fanelli, "From chemical reactions to evolution: Emergence of species" *Europhys. Lett.*, vol. 77, no. 1, p. 18005, 2007.

[4]   D. E. Hughes, "The bacterial cytoplasmic membrane.," *J. Gen. Microbiol.*, vol. 29, no. 1962, pp. 39–46, 1962.

[5]   J. B. Dacks and M. C. Field, "Evolution of the eukaryotic membrane-trafficking system: origin, tempo and mode.," *J. Cell Sci.*, vol. 120, no. Pt 17, pp. 2977–2985, 2007.

[6]   Y. Elbaz-Alon, M. Eisenberg-Bord, V. Shinder, S. B. Stiller, E. Shimoni, N. Wiedemann, T. Geiger, and M. Schuldiner, "Lam6 Regulates the Extent of Contacts between Organelles," *Cell Rep*, vol. 12, no. 1, pp. 7–14, 2015.

[7]   J. S. Bonifacino and B. S. Glick, "The Mechanisms of Vesicle Budding and Fusion," *Cell*, vol. 116, no. 2, pp. 153–166, 2004.

[8]   R. M. Epand and R. F. Epand, "Membrane Fusion," vol. 848, no. April, pp. 841–848, 2002.

[9]   D. Hoffmann, T. Grunwald, S. Kuate, and O. Wildner, "Mechanistic analysis and comparison of viral fusogenic membrane proteins for their synergistic effects on chemotherapy," *Cancer Biol. Ther*, vol. 6, no. 4, pp. 510–8, 2007.

[10]   R. Jahn and R. H. Scheller, "SNAREs — engines for membrane fusion," *Nat. Rev. Mol. Cell Biol.*, vol. 7, no. 9, pp. 631–643, 2006.

[11]   R. Jahn, T. Lang, and T. C. Su, "Membrane Fusion," vol. 112, no. 3, pp. 519–533, 2003.

[12]   H. Bayley, B. Cronin, A. Heron, M. a. Holden, W. L. Hwang, R. Syeda, J. Thompson, and M. Wallace, "Droplet interface bilayers" *Mol. Biosyst.*, vol. 4, no. 12, pp. 1191–1208, 2008.

[13]   M. B. Linder, G. R. Szilvay, T. Nakari-Setälä, and M. E. Penttilä, "Hydrophobins: the protein-amphiphiles of filamentous fungi," *FEMS Microbiol. Rev.*, vol. 29, no. 5, pp. 877–896, 2005.

[14] J. G. H. Wessels, "Developmental Regulation of Fungal Cell Wall Formation," *Annu. Rev. Phytopathol.*, vol. 32, no. 1, pp. 413–437, 1994.

[15] S. Askolin, M. Linder, K. Scholtmeijer, M. Tenkanen, M. Penttilä, M. L. de Vocht, and H. a B. Wösten, "Interaction and comparison of a class I hydrophobin from Schizophyllum commune and class II Hydrophobins Trichoderma reesei," *Biomacromolecules*, vol. 7, no. 4, pp. 1295–1301, 2006.

[16] S. Askolin, T. Nakari-Setälä, and M. Tenkanen, "Overproduction, purification, and characterization of the Trichoderma reesei hydrophobin HFBI," *Appl. Microbiol. Biotechnol.*, vol. 57, pp. 124–130, 2001.

[17] K. Scholtmeijer, M. I. Janssen, B. Gerssen, M. L. de Vocht, B. M. van Leeuwen, T. G. van Kooten, H. a B. Wösten, and J. G. H. Wessels, "Surface modifications created by using engineered hydrophobins.," *Appl. Environ. Microbiol.*, vol. 68, no. 3, pp. 1367–73, 2002.

[18] A. R. Cox, D. L. Aldred, and A. B. Russell, "Exceptional stability of food foams using class II hydrophobin HFBII," *Food Hydrocoll.*, vol. 23, no. 2, pp. 366–376, 2009.

[19] A. J. Green, K. a. Littlejohn, P. Hooley, and P. W. Cox, "Formation and stability of food foams and aerated emulsions: Hydrophobins as novel functional ingredients," *Curr. Opin. Colloid Interface Sci.*, vol. 18, no. 4, pp. 292–301, 2013.

[20] L. De Stefano, I. Rea, I. Rendina, M. Giocondo, S. Houmadi, S. Longobardi, and P. Giardina, "Organic-inorganic Interfaces for a New Generation of Hybrid Biosensors," *Biosens. - Emerg. Mater. Appl.*, pp. 311–332, 2011.

[21] K. Scholtmeijer, J. G. H. Wessels, and H. a B. Wösten, "Fungal hydrophobins in medical and technical applications," *Appl. Microbiol. Biotechnol.*, vol. 56, pp. 1–8, 2001.

[22] M. Sarparanta, L. M. Bimbo, J. Rytkoänen, E. Mäkilä, T. J. Laaksonen, P. Laaksonen, M. Nyman, J. Salonen, M. B. Linder, J. Hirvonen, H. a. Santos, and A. J. Airaksinen, "Intravenous delivery of hydrophobin-functionalized porous silicon nanoparticles: Stability, plasma protein adsorption and biodistribution," *Mol. Pharm.*, vol. 9, pp. 654–663, 2012.

[23] M. Lienemann, J. A. Gandier, J. J. Joensuu, A. Iwanaga, Y. Takatsuji, T. Haruyama, E. Master, M. Tenkanen, and M. B. Lindera, "Structure-function relationships in hydrophobins: Probing the role of charged side chains," *Appl. Environ. Microbiol.*, vol. 79, no. 18, pp. 5533–5538, 2013.

[24] Y. Corvis, A. Walcarius, R. Rink, N. T. Mrabet, and J. T. Hirvonen, "Charge-Based Engineering of Hydrophobin HFBI: Effect on Interfacial Assembly and Interactions," *Biomacromolecules*, vol. 4, no. 3, pp. 1750–1758, 2002.

[25] G. van Meer, D. R. Voelker, and G. W. Feigenson, "Membrane lipids: where they are and how they behave," *Nat. Rev. Mol. Cell Biol.*, vol. 9, no. 2, pp. 112–124, 2008.

[26] M. Shinitzky, *Biomembranes*, no. November. Weinheim, 1993.

[27] M. Edidin, "Lipids on the frontier: a century of cell-membrane bilayers.," *Nat. Rev. Mol. Cell Biol.*, vol. 4, no. 5, pp. 414–418, 2003.

[28] H. Kimizuka and K. Koketsu, "Ion transport through cell membrane.," *J. Theor. Biol.*, vol. 6, pp. 290–305, 1964.

[29] B. Alberts, A. Johnson, J. Lewis, K. Roberts, and P. Walter, "Molecular Biology of the Cell," pp. 195–262, 2008.

[30] C. F. Lee, C. P. Brangwynne, J. Gharakhani, A. a. Hyman, and F. Jülicher, "Spatial Organization of the Cell Cytoplasm by Position-Dependent Phase Separation," *Phys. Rev. Lett.*, vol. 111, no. 8, p. 088101, 2013.

[31] E. Rodriguez-Boulan, G. Kreitzer, and A. Müsch, "Organization of vesicular trafficking in epithelia," *Nat. Rev. Mol. Cell Biol.*, vol. 6, no. 3, pp. 233–247, 2005.

[32] C. B. Of and I. Protein, "Cell Biology of Intracellular Protein," no. Figure I, pp. 195–229, 1990.

[33] F. Scholkmann, D. Fels, and M. Cifra, "Non-chemical and non-contact cell-to-cell communication: a short review," *Am J Transl Res*, vol. 5, no. 6, pp. 586–593, 2013.

[34] J. D. Scott and T. Pawson, "Cell signaling in space and time: where proteins come together and when they're apart," *Science*, vol. 326, no. 5957, pp. 1220–1224, 2009.

[35] M. a. Lemmon and J. Schlessinger, "Cell Signaling by Receptor Tyrosine Kinases," *Cell*, vol. 141, no. 7, pp. 1117–1134, 2010.

[36] S. Reitsma, D. W. Slaaf, H. Vink, M. a M. J. van Zandvoort, and M. G. a oude Egbrink, "The endothelial glycocalyx: composition, functions, and visualization.," *Pflugers Arch.*, vol. 454, no. 3, pp. 345–59, 2007.

[37] S. Weinbaum, J. M. Tarbell, and E. R. Damiano, "The structure and function of the endothelial glycocalyx layer.," *Annu. Rev. Biomed. Eng.*, vol. 9, pp. 121–167, 2007.

[38] B. P. Head, H. H. Patel, and P. a. Insel, "Interaction of membrane/lipid rafts with the cytoskeleton: Impact on signaling and function: Membrane/lipid rafts, mediators of cytoskeletal arrangement and cell signaling," *Biochim. Biophys. Acta - Biomembr.*, vol. 1838, no. 2, pp. 532–545, 2014.

[39] P. Cowin and B. Burke, "Cytoskeleton-membrane interactions," *Curr. Opin. Cell Biol.*, vol. 8, no. 1, pp. 56–65, 1996.

[40] K. Boesze-Battaglia and R. J. Schimmel, "Cell membrane lipid composition and distribution: implications for cell function and lessons learned from photoreceptors and platelets," *J. Exp. Biol.*, vol. 200, no. Pt 23, pp. 2927–2936, 1997.

[41] Ü. Coskun and K. Simons, "Cell membranes: The lipid perspective," *Structure*, vol. 19, no. 11, pp. 1543–1548, 2011.

[42] E. Ikonen, "Cellular cholesterol trafficking and compartmentalization," *Nat. Rev. Mol. Cell Biol.*, vol. 9, no. 2, pp. 125–138, 2008.

[43] R. X. Tan and J. H. Chen, "The cerebrosides," *Nat. Prod. Rep.*, vol. 20, no. 5, p. 509, 2003.

[44] A. Engel and H. E. Gaub, "Structure and Mechanics of Membrane Proteins," *Annu. Rev. Biochem.*, vol. 77, no. 1, pp. 127–148, 2008.

[45] G. von Heijne, "Membrane-protein topology," *Nat. Rev. Mol. Cell Biol.*, vol. 7, no. 12, pp. 909–918, 2006.

[46] N. Gamper and M. S. Shapiro, "Regulation of ion transport proteins by membrane phosphoinositides," *Nat. Rev. Neurosci.*, vol. 8, no. 12, pp. 921–934, 2007.

[47] K. Moravcevic, C. L. Oxley, and M. A. Lemmon, "Conditional Peripheral Membrane Proteins: Facing up to Limited Specificity," *Structure*, vol. 20, no. 1, pp. 15–27, 2012.

[48] D. Marsh, L. I. Horváth, M. J. Swamy, S. Mantripragada, and J. H. Kleinschmidt, "Interaction of membrane-spanning proteins with peripheral and lipid-anchored membrane proteins: perspectives from protein-lipid interactions ," *Mol. Membr. Biol.*, vol. 19, pp. 247–255, 2002.

[49] J. N. Sachs and D. M. Engelman, "Introduction to the Membrane Protein Reviews: The Interplay of Structure, Dynamics, and Environment in

Membrane Protein Function," *Annu. Rev. Biochem.*, vol. 75, no. 1, pp. 707–712, 2006.

[50] H. Chiba, M. Osanai, M. Murata, T. Kojima, and N. Sawada, "Transmembrane proteins of tight junctions," *Biochim. Biophys. Acta - Biomembr.*, vol. 1778, no. 3, pp. 588–600, 2008.

[51] E. R. Pianka, "The Structure of the Phospholipids," *Ecology*, vol. 4, no. 1973, pp. 53–74, 2007.

[52] E. Evans, "Chapter 15 Physical actions in biological adhesion," *Handb. Biol. Phys.*, vol. 1, no. Structure and Dynamics of Membranes, pp. 723–754, 1995.

[53] F. Theillet, A. Binol, T. Frembgen-kesner, K. Hingorani, M. Sarkar, C. Kyne, C. Li, P. B. Crowley, L. Gierasch, G. J. Pielak, A. H. Elcock, A. Gershenson, and P. Selenko, "Physicochemical Properties of Cells and Their Effects on Intrinsically Disordered Proteins (IDPs)," *Chem. Rev.*, 2015.

[54] T. D. Brock and M. R. Edwards, "Fine Structure of Thermus aquaticus, an Extreme Thermophile," *J. Bacteriol.*, vol. 104, no. 1, pp. 509–517, 1970.

[55] M. R. Ammar, N. Kassas, S. Chasserot-Golaz, M.-F. Bader, and N. Vitale, "Lipids in Regulated Exocytosis: What are They Doing?," *Front. Endocrinol. (Lausanne).*, vol. 4, no. September, pp. 1–6, 2013.

[56] C. Salaün, D. J. James, and L. H. Chamberlain, "UKPMC Funders Group Lipid Rafts and the Regulation of Exocytosis," *Biochemistry*, vol. 5, no. 4, pp. 255–264, 2008.

[57] D. Chandler, "Interfaces and the driving force of hydrophobic assembly.," *Nature*, vol. 437, no. 7059, pp. 640–647, 2005.

[58] V. a. Frolov and J. Zimmerberg, "Cooperative elastic stresses, the hydrophobic effect, and lipid tilt in membrane remodeling," *FEBS Lett.*, vol. 584, no. 9, pp. 1824–1829, 2010.

[59] J. N. Israelachvili, D. J. Mitchell, and B. W. Ninham, "Theory of self-assembly of hydrocarbon amphiphiles into micelles and bilayers," *J. Chem. Soc. Faraday Trans. 2*, vol. 72, p. 1525, 1976.

[60] B. H. Morrow, P. H. Koenig, and J. K. Shen, "Self-assembly and bilayer-micelle transition of fatty acids studied by replica-exchange constant ph molecular dynamics," *Langmuir*, vol. 29, pp. 14823–14830, 2013.

[61] J. M. Seddon and R. H. Templer, "Chapter 3 Polymorphism of lipid-water systems," *Handb. Biol. Phys.*, vol. 1, no. C, pp. 97–160, 1995.

[62] M. Pavlin, T. Kotnik, D. Miklavčič, P. Kramar, and A. Maček Lebar, "Chapter Seven Electroporation of Planar Lipid Bilayers and Membranes," *Adv. Planar Lipid Bilayers Liposomes*, vol. 6, no. 07, pp. 165–226, 2008.

[63] R. Reigada and M. Fernandez, "Structure and Electroporation of Lipid Bilayers : a Molecular Dynamics Study," *Gen. Assem. Sci.*, 2011.

[64] J. D. Litster, "Stability of lipid bilayers and red blood cell membranes," *Phys. Lett. A*, vol. 53, no. 3, pp. 193–194, 1975.

[65] L. V Chernomordik, S. I. Sukharev, S. V Popov, V. F. Pastushenko, a V Sokirko, I. G. Abidor, and Y. a Chizmadzhev, "The electrical breakdown of cell and lipid membranes: the similarity of phenomenologies.," *Biochim. Biophys. Acta*, vol. 902, pp. 360–373, 1987.

[66] L. V. Chernomordik, J. Zimmerberg, and M. M. Kozlov, "Membranes of the world unite!," *J. Cell Biol.*, vol. 175, no. 2, pp. 201–207, 2006.

[67] J. a McNew, F. Parlati, R. Fukuda, R. J. Johnston, K. Paz, F. Paumet, T. H. Söllner, and J. E. Rothman, "Compartmental specificity of cellular membrane fusion encoded in SNARE proteins.," *Nature*, vol. 407, no. 6801, pp. 153–159, 2000.

[68] S. Mondal Roy and M. Sarkar, "Membrane fusion induced by small molecules and ions.," *J. Lipids*, vol. 2011, p. 528784, 2011.

[69] S. Martens and H. T. McMahon, "Mechanisms of membrane fusion: disparate players and common principles.," *Nat. Rev. Mol. Cell Biol.*, vol. 9, no. 7, pp. 543–556, 2008.

[70] G. Cevc and H. Richardsen, "Lipid vesicles and membrane fusion," *Adv. Drug Deliv. Rev.*, vol. 38, no. 3, pp. 207–232, 1999.

[71] L. V Chernomordik and M. M. Kozlov, "Mechanics of membrane fusion.," *Nat. Struct. Mol. Biol.*, vol. 15, no. 7, pp. 675–683, 2008.

[72] L. V. Chernomordik and M. M. Kozlov, "Protein-Lipid interplay in Fusion and Fission of Biological memebranes" *Annu. Rev. Biochem.*, vol. 72, no. 1, pp. 175–207, 2003.

[73] V. S. Markin, M. M. Kozlov, and V. L. Borovjagin, "On the theory of membrane fusion. The stalk mechanism.," *Gen. Physiol. Biophys.*, vol. 3, no. 5, pp. 361–377, 1984.

[74] V. S. Markin and J. P. Albanesi, "Membrane fusion: stalk model revisited.," *Biophys. J.*, vol. 82, no. 2, pp. 693–712, 2002.

[75] Y. Kozlovsky and M. M. Kozlov, "Stalk model of membrane fusion: solution of energy crisis.," *Biophys. J.*, vol. 82, no. 2, pp. 882–895, 2002.

[76] H. J. Risselada, G. Bubnis, and H. Grubmuller, "Expansion of the fusion stalk and its implication for biological membrane fusion," *Proc. Natl. Acad. Sci.*, vol. 111, no. 30, pp. 11043–11048, 2014.

[77] L. V. Chernomordik and M. M. Kozlov, "Membrane hemifusion: Crossing a chasm in two leaps," *Cell*, vol. 123, no. 3, pp. 375–382, 2005.

[78] N. Vardjan, J. Jorgacevski, and R. Zorec, "Fusion pores, SNAREs, and exocytosis.," *Neuroscientist*, vol. 19, no. 2, pp. 160–74, 2013.

[79] P. I. Kuzmin, J. Zimmerberg, Y. a Chizmadzhev, and F. S. Cohen, "A quantitative model for membrane fusion based on low-energy intermediates.," *Proc. Natl. Acad. Sci. U. S. A.*, vol. 98, no. 13, pp. 7235–7240, 2001.

[80] A. Portis, C. Newton, W. Pangborn, and D. Papahadjopoulos, "Studies on the mechanism of membrane fusion: evidence for an intermembrane Ca2+-phospholipid complex, synergism with Mg2+, and inhibition by spectrin.," *Biochemistry*, vol. 18, no. 5, pp. 780–90, 1979.

[81] P. Hornby and P. R. Cullis, "Influence of local and neutral anaesthetics on the polymorphic phase preferences of egg yolk phosphatidylethanolamine.," *Biochim. Biophys. Acta*, vol. 647, no. 2, pp. 285–292, 1981.

[82] J. a Veiro, R. G. Khalifah, and E. S. Rowe, "The polymorphic phase behavior of dielaidoylphosphatidylethanolamine. Effect of n-alkanols.," *Biochim. Biophys. Acta*, vol. 979, no. 2, pp. 251–6, 1989.

[83] L. Koubi, M. Tarek, M. L. Klein, and D. Scharf, "Distribution of halothane in a dipalmitoylphosphatidylcholine bilayer from molecular dynamics calculations.," *Biophys. J.*, vol. 78, no. 2, pp. 800–11, 2000.

[84] W. Wickner and R. Schekman, "Membrane fusion," *Nat. Struct. & Mol. Biol.*, vol. 15, no. n7, pp. 658–664, 2008.

[85] D. Fasshauer, "Structural insights into the SNARE mechanism," *Biochim. Biophys. Acta - Mol. Cell Res.*, vol. 1641, no. 2–3, pp. 87–97, 2003.

[86] A. T. Brunger, "Structure and function of SNARE and SNARE-interacting proteins.," *Q. Rev. Biophys.*, vol. 38, no. December 2005, pp. 1–47, 2005.

[87] Y. Gao, S. Zorman, G. Gundersen, Z. Xi, L. Ma, G. Sirinakis, J. E. Rothman, and Y. Zhang, "T (where k," vol. 28, 2012.

[88] T. Weber, B. V. Zemelman, J. a. McNew, B. Westermann, M. Gmachl, F. Parlati, T. H. Söllner, and J. E. Rothman, "SNAREpins: Minimal machinery for membrane fusion," *Cell*, vol. 92, no. 6, pp. 759–772, 1998.

[89] J. a McNew, T. Weber, D. M. Engelman, T. H. Söllner, and J. E. Rothman, "The length of the flexible SNAREpin juxtamembrane region is a critical determinant of SNARE-dependent fusion.," *Mol. Cell*, vol. 4, no. 3, pp. 415–421, 1999.

[90] S. J. Elledge, S. P. Jackson, R. A. Weinberg, F. E. Kleiman, J. L. Manley, T. Ouchi, Z. Q. Pan, J. Chen, Y. S. Kim, A. M. Jetten, S. G. Brodie, S. Kim, M. B. Kastan, M. Sgagias, K. H. Cowan, L. C. Brody, S. Fu, M. Lai, R. Baer, J. Chen, P. R. Andreassen, and J. Hohfeld, "how Synaptotagmin Promotes Membrane Fusion," no. May, pp. 1205–1209, 2007.

[91] D. Kümmel, S. S. Krishnakumar, D. T. Radoff, F. Li, C. G. Giraudo, F. Pincet, J. E. Rothman, and K. M. Reinisch, "Complexin cross-links prefusion SNAREs into a zigzag array," *Nat. Struct. Mol. Biol.*, vol. 18, no. 8, pp. 927–933, 2011.

[92] M. Park, S. Touihri, I. Müller, U. Mayer, and G. Jürgens, "Sec1/Munc18 protein stabilizes fusion-competent syntaxin for membrane fusion in Arabidopsis cytokinesis.," *Dev. Cell*, vol. 22, no. 5, pp. 989–1000, 2012.

[93] Z. Chen, B. Cooper, S. Kalla, F. Varoqueaux, and S. M. Young, "The Munc13 proteins differentially regulate readily releasable pool dynamics and calcium-dependent recovery at a central synapse.," *J. Neurosci.*, vol. 33, no. 19, pp. 8336–51, 2013.

[94] S. E. Kwon and E. R. Chapman, "Synaptophysin Regulates the Kinetics of Synaptic Vesicle Endocytosis in Central Neurons," *Neuron*, vol. 70, no. 5, pp. 847–854, 2011.

[95] J. Lund, J. Kaiser, U. Jacob, J. V Ravetch, J. V Ravetch, P. Williams, R. a Dwek, K. Shikata, F. Takeuchi, N. Kojima, T. Mizouchi, S. J. Thompson, a S. Lemonidis, C. J. Elson, S. L. Morrison, P. Bruhns, K. Horiuchi, J. V Ravetch, T. L. Towers, J. V Ravetch, a Samuelsson, J. W. Pollard, J. V Ravetch, M. P. Madaio, J. V Ravetch, B. E. Collins, P. Bengston, J. C. Paulson, P. Smith, J. Clowney, a Kim, and S. Science, "N- to C-Terminal SNARE Complex Assembly Promotes Rapid Membrane Fusion," no. August, pp. 673–676, 2006.

[96] F. Li, D. Kümmel, J. Coleman, K. M. Reinisch, J. E. Rothman, and F. Pincet, "A half-zippered SNARE complex represents a functional intermediate in membrane fusion," *J. Am. Chem. Soc.*, vol. 136, no. 9, pp. 2456–2464, 2014.

[97] T. J. Melia, T. Weber, J. a McNew, L. E. Fisher, R. J. Johnston, F. Parlati, L. K. Mahal, T. H. Sollner, and J. E. Rothman, "Regulation of membrane fusion by the membrane-proximal coil of the t-SNARE during zippering of SNAREpins.," *J. Cell Biol.*, vol. 158, no. 5, pp. 929–40, 2002.

[98] L. Shi, Q.-T. Shen, a. Kiel, J. Wang, H.-W. Wang, T. J. Melia, J. E. Rothman, and F. Pincet, "SNARE Proteins: One to Fuse and Three to Keep the Nascent Fusion Pore Open," *Science (80-.).*, vol. 335, no. 6074, pp. 1355–1359, 2012.

[99] E. N. B. Sakmann, *Single Channel Recording*. 1995.

[100] B. Sakmann and E. Neher, "Patch clamp techniques for studying ionic channels in excitable membranes.," *Annu. Rev. Physiol.*, vol. 46, pp. 455–472, 1984.

[101] S. McDavid and K. P. M. Currie, "G-Proteins Modulate Cumulative Inactivation of N-Type (CaV2.2) Calcium Channels," *J. Neurosci.*, vol. 26, no. 51, pp. 13373–13383, 2006.

[102] J. W. Gibbs, Y. F. Zhang, M. D. Shumate, and D. a Coulter, "Regionally selective blockade of GABAergic inhibition by zinc in the thalamocortical system: functional significance.," *J. Neurophysiol.*, vol. 83, no. 3, pp. 1510–1521, 2000.

[103] P. Tu, C. Kunert-Keil, S. Lucke, H. Brinkmeier, and A. Bouron, "Diacylglycerol analogues activate second messenger-operated calcium channels exhibiting TRPC-like properties in cortical neurons," *J. Neurochem.*, vol. 108, no. 1, pp. 126–138, 2009.

[104] B. Y. G. Matthews, E. Neher, and R. Penner, "FaJiberq, Gottingen.," pp. 131–144, 1989.

[105] P. Perez-Cornejo and J. Arreola, "Regulation of Ca2+-activated chloride channels by cAMP and CFTR in parotid acinar cells," *Biochem. Biophys. Res. Commun.*, vol. 316, no. 3, pp. 612–617, 2004.

[106] N. C. Guérineau, J. L. Bossu, B. H. Gähwiler, and U. Gerber, "G-protein-mediated desensitization of metabotropic glutamatergic and muscarinic responses in CA3 cells in rat hippocampus.," *J. Physiol.*, vol. 500 (Pt 2, pp. 487–96, 1997.

[107] R. E. Thompson, M. Lindau, and W. W. Webb, "Robust, high-resolution, whole cell patch-clamp capacitance measurements using square wave stimulation.," *Biophys. J.*, vol. 81, no. 2, pp. 937–948, 2001.

[108] S. H. White and T. E. Thompson, "Capacitance, area, and thickness variations in thin lipid films.," *Biochim. Biophys. Acta*, vol. 323, no. 1, pp. 7–22, 1973.

[109] B. Rituper, A. Guček, J. Jorgačevski, A. Flašker, M. Kreft, and R. Zorec, "High-resolution membrane capacitance measurements for the study of exocytosis and endocytosis," *Nat. Protoc.*, vol. 8, no. 6, pp. 1169–1183, 2013.

[110] G. Kilic, "Exocytosis in bovine chromaffin cells: studies with patch-clamp capacitance and FM1-43 fluorescence.," *Biophys. J.*, vol. 83, no. 2, pp. 849–857, 2002.

[111] A. Llobet, V. Beaumont, and L. Lagnado, "Real-Time Measurement of Exocytosis and Endocytosis Using Interference of Light," *Neuron*, vol. 40, no. 6, pp. 1075–1086, 2003.

[112] B. G. Kornreich, "The patch clamp technique: principles and technical considerations.," *J. Vet. Cardiol.*, vol. 9, no. 1, pp. 25–37, 2007.

[113] M. Lindau and E. Neher, "Patch-clamp techniques for time-resolved capacitance measurements in single cells.," *Pflugers Arch.*, vol. 411, no. 2, pp. 137–146, 1988.

[114] J.-P. Salvetat, G. Briggs, J.-M. Bonard, R. Bacsa, A. Kulik, T. Stöckli, N. Burnham, and L. Forró, "Patch clamp technique: review of the current state of the art and potential contributions from nanoengineering," *Science (80-.).*, vol. 339, no. 6119, p. 141022172723000, 2013.

[115] C. Kushmerick and H. Von Gersdorff, "Exo-endocytosis at mossy fiber terminals: toward capacitance measurements in cells with arbitrary geometry," *Proc.Natl.Acad.Sci.U.S.A*, vol. 100, no. 0027–8424 (Print), pp. 8618–8620, 2003.

[116] J. Bhagyajyoti, L. Sudheer, P. Bhaskar, and C. Parvathi, "Review on Lock-in Amplifier," *Int. J. Sci. Eng. Technol. Res.*, vol. 1, no. 5, pp. 40–45, 2012.

[117] a J. Sherman, a Shrier, and E. Cooper, "Series resistance compensation for whole-cell patch-clamp studies using a membrane state estimator.," *Biophys. J.*, vol. 77, no. 5, pp. 2590–2601, 1999.

[118] C. V. Kulkarni, W. Wachter, G. Iglesias-Salto, S. Engelskirchen, and S. Ahualli, "Monoolein: a magic lipid?," *Phys. Chem. Chem. Phys.*, vol. 13, no. 8, pp. 3004–3021, 2011.

[119] J. P. Dilger and R. Benz, "Optical and electrical properties of thin monoolein lipid bilayers.," *J. Membr. Biol.*, vol. 85, no. 2, pp. 181–189, 1985.

[120] W. R. Redwood, F. R. Pfeiffer, J. a. Weisbach, and T. E. Thompson, "Physical properties of bilayer membranes formed from a synthetic saturated phospholipid in n-decane.," *Biochim. Biophys. Acta*, vol. 233, no. 1, pp. 1–6, 1971.

[121] S. Tristram-Nagle, D. J. Kim, N. Akhunzada, N. Kučerka, J. C. Mathai, J. Katsaras, M. Zeidel, and J. F. Nagle, "Structure and water permeability of fully hydrated diphytanoylPC," *Chem. Phys. Lipids*, vol. 163, pp. 630–637, 2010.

[122] S. J. Attwood, Y. Choi, and Z. Leonenko, "Preparation of DOPC and DPPC supported planar lipid bilayers for atomic force microscopy and atomic force spectroscopy," *Int. J. Mol. Sci.*, vol. 14, no. 2, pp. 3514–3539, 2013.

[123] P. a. Leventis and S. Grinstein, "The Distribution and Function of Phosphatidylserine in Cellular Membranes," *Annu. Rev. Biophys.*, vol. 39, no. 1, pp. 407–427, 2010.

[124] S. Quetglas, C. Iborra, N. Sasakawa, L. De Haro, K. Kumakura, K. Sato, C. Leveque, and M. Seagar, "Calmodulin and lipid binding to synaptobrevin regulates calcium-dependent exocytosis," *EMBO J.*, vol. 21, no. 15, pp. 3970–3979, 2002.

[125] S. T. W. Nam-Trung Nguyen, *Fundamental And Applications of Microfluidics*. House, Artech, 2002.

[126] P. Tabeling, *Introduction to microfluidics*. 2015.

[127] S. N. J.L. Sang-Joon, *Microfabrication for Microfluidics*, vol. 1. Artech house INC, 2010.

[128] Y. Zhao, S. Inayat, D. a Dikin, R. S. Ruoff, and J. B. Troy, "Impedance characterization and modelling of an improved patch clamp device," *Proc. Inst. Mech. Eng. Part N J. Nanoeng. Nanosyst.*, vol. 1, no. -1, pp. 1–11, 2010.

[129] R. Seemann, M. Brinkmann, T. Pfohl, and S. Herminghaus, "Droplet based microfluidics," *Reports Prog. Phys.*, vol. 75, no. 1, p. 016601, 2012.

[130] S.-Y. Teh, R. Lin, L.-H. Hung, and A. P. Lee, "Droplet microfluidics.," *Lab Chip*, vol. 8, no. 2, pp. 198–220, 2008.

[131] J. Berthier, *Microdrops and Digital Microfluidics*. William Andrew, 2013.

[132] S. Thutupalli, J.-B. Fleury, A. Steinberger, S. Herminghaus, and R. Seemann, "Why can artificial membranes be fabricated so rapidly in microfluidics?," *Chem. Commun.*, vol. 49, no. 14, p. 1443, 2013.

[133] K. Funakoshi, H. Suzuki, and S. Takeuchi, "Lipid bilayer formation by contacting monolayers in a microfluidic device for membrane protein analysis.," *Anal. Chem.*, vol. 78, no. 24, pp. 8169–74, 2006.

[134] S. Thutupalli, S. Herminghaus, and R. Seemann, "Bilayer membranes in micro-fluidics: from gel emulsions to soft functional devices," *Soft Matter*, vol. 7, no. 4, pp. 1312–1320, 2011.

[135] G. Hed and S. a Safran, "Initiation and dynamics of hemifusion in lipid bilayers.," *Biophys. J.*, vol. 85, no. 1, pp. 381–389, 2003.

[136] C. Redon, F. Brochard-Wyart, and F. Rondelez, "Dynamics of dewetting," *Phys. Rev. Lett.*, vol. 66, no. 6, pp. 715–718, 1991.

[137] R. Fetzer and K. Jacobs, "Slippage of Newtonian liquids: Influence on the dynamics of dewetting thin films," *Langmuir*, vol. 23, no. 37, pp. 11617–11622, 2007.

[138] T. Kuhl, Y. Guo, J. L. Alderfer, A. D. Berman, D. Leckband, J. Israelachvili, and S. W. Hui, "Direct Measurement of Polyethylene Glycol Induced Depletion Attraction between Lipid Bilayers," *Langmuir*, vol. 12, no. 12, pp. 3003–3014, 1996.

[139] J. Nikolaus, M. Stöckl, D. Langosch, R. Volkmer, and A. Herrmann, "Direct Visualization of Large and Protein-Free Hemifusion Diaphragms," *Biophys. J.*, vol. 98, no. 7, pp. 1192–1199, 2010.

[140] B. Zhang, Y. H. Koh, R. B. Beckstead, V. Budnik, B. Ganetzky, and H. J. Bellen, "Synaptic vesicle size and number are regulated by a clathrin adaptor protein required for endocytosis," *Neuron*, vol. 21, no. 6, pp. 1465–1475, 1998.

[141] M. B. Linder, "Hydrophobins: Proteins that self assemble at interfaces," *Curr. Opin. Colloid Interface Sci.*, vol. 14, no. 5, pp. 356–363, 2009.

[142] M. Sunde, a. H. Y. Kwan, M. D. Templeton, R. E. Beever, and J. P. Mackay, "Structural analysis of hydrophobins," *Micron*, vol. 39, no. 7, pp. 773–784, 2008.

[143] M. K. Gilson and B. H. Honig, "The dielectric constant of a folded protein.," *Biopolymers*, vol. 25, pp. 2097–2119, 1986.

[144] J. N. Vargas, R. Seemann, and J.-B. Fleury, "Fast membrane hemifusion via dewetting between lipid bilayers.," *Soft Matter*, vol. 00, pp. 1–7, 2014.

[145] P. Kukić, D. Farrell, L. P. McIntosh, B. Garcia-Moreno E, K. S. Jensen, Z. Toleikis, K. Teilum, and J. E. Nielsen, "Protein dielectric constants

determined from NMR chemical shift perturbations.," *J. Am. Chem. Soc.*, vol. 135, no. 45, pp. 16968–16976, 2013.

[146] D. L. Cheung, "Molecular simulation of hydrophobin adsorption at an oil-water interface.," *Langmuir*, vol. 28, no. 23, pp. 8730–6, 2012.

[147] D. H. Kim and J. a Frangos, "Effects of amyloid beta-peptides on the lysis tension of lipid bilayer vesicles containing oxysterols.," *Biophys. J.*, vol. 95, no. 2, pp. 620–628, 2008.

Acknowledgements

The accomplishment of this thesis would not have been possible without the guidance, contribution and support from many different people. I would like to thank specially my PhD supervisor **Prof. Dr. Ralf Seemann**. For more than 4 years he guided me with patience and dedication. He was always ready to discuss or explain any aspect of my research topic. Beside his professionalism and scientific rigor, I thank Prof. Seemann for his unconditional support and understanding to my anxiety disorder condition. For a long time during my PhD I faced a condition that made me think even to drop the research, but he was always there to push me forwards. In a great extent, the accomplishment of this thesis is due to Prof. Seemann support. I will never have enough words to thank him but I will always remember and appreciate my PhD supervisor.

Declaration

I hereby swear in lieu of an oath that I have independently prepared this thesis and without using other aids than those stated. The data and concepts taken over from other sources or taken over indirectly are indicated citing the source. The thesis was not submitted so far either in Germany or in other country in the same or similar form in a procedure for obtaining an academic title.

Saarbrückent, 27rd November 2015

Jose Nabor Vargas

Eidesstattliche Versicherung

Hiermit versichere ich an Eides statt, dass ich die vorliegende Arbeit selbstständig und ohne Benutzung anderer als der angegebenen Hilfsmittel angefertigt habe. Die aus anderen Quellen oder indirekt übernommenen Daten und Konzepte sind unter Angabe der Quelle gekennzeichnet. Die Arbeit wurde bisher weder im In- noch im Ausland in gleicher oder ähnlicher Form in einem Verfahren zur Erlangung eines akademischen Grades vorgelegt.

Saarbrückent, 27rd November 2015

Jose Nabor Vargas